

In-Medium Nucleonic Interactions and Chiral Effective Field Theory: Insight into the Nuclear
and Neutron Matter Equation of State from Neutron Skins to Neutron Stars

A Dissertation

Presented in Partial Fulfillment of the Requirements for the

Degree of Doctor of Philosophy

with a

Major in Physics

in the

College of Graduate Studies

University of Idaho

by

Randy Millerson

Major Professor: Francesca Sammarruca, Ph.D.

Committee Members: Ruprecht Machleidt, Ph.D.; Andreas Vasdekis, Ph.D.;

Lyudmyla Barannyk, Ph.D.

Department Administrator: John Hiller, Ph.D.

December 2020

Authorization to Submit Dissertation

This dissertation of Randy Millerson, submitted for the degree of Doctor of Philosophy with a major in Physics and titled “In-Medium Nucleonic Interactions and Chiral Effective Field Theory: Insight into the Nuclear and Neutron Matter Equation of State from Neutron Skins to Neutron Stars,” has been reviewed in final form. Permission, as indicated by the signatures and dates given below, is now granted to submit final copies to the College of Graduate Studies for approval.

Major Professor: _____ Date _____
 Francesca Sammarruca, Ph.D.

Committee
 Members: _____ Date _____
 Ruprecht Machleidt, Ph.D.

_____ Date _____
 Andreas Vasdekis, Ph.D.

_____ Date _____
 Lyudmyla Barannyk, Ph.D.

Department
 Administrator: _____ Date _____
 John Hiller, Ph.D.

Abstract

The goal of microscopic nuclear physics is to describe nuclear structure and nuclear reactions in terms of fundamental forces between the elementary constituents of hadrons.

Quantum Chromodynamics (QCD) is understood to be the fundamental theory of strong interactions. In QCD, hadrons are bound states arising from interacting quarks and gluons. Unfortunately, in the low-energy regime QCD is non-perturbative, which renders the theory unmanageable for the description of low-energy reactions and nuclear structure.

Chiral Effective Field Theory provides the link between QCD and nuclear forces that are suitable to describe bound nuclear systems and low-energy reactions. While respecting the symmetries of the QCD Lagrangian, the theory adopts nucleons and pions as its degrees of freedom. In this work we use two- and three-nucleon forces constructed from Chiral Effective Field Theory and apply them in nuclear matter. The energy per particle as a function of density in infinite nuclear matter is referred to as the nuclear matter equation of state.

Nuclear matter is an infinite system with equal densities of protons and neutrons. More precisely, this is referred to as “symmetric nuclear matter.” Neutron-rich matter is then an infinite system with larger concentration of neutrons, and, of course, pure neutron matter contains only neutrons. The many-body framework we use to evaluate the nuclear matter equation of state is known as the Bruckner-Hartree-Fock approach.

Having presented our theoretical tools for the development of the equation of state based on few-nucleon chiral forces (Chapter 2), we proceed to show and apply our predictions.

Modern theoretical predictions of neutron-rich matter are particularly timely. On-going and planned experiments aim at measuring observables which are sensitive to the equation of state of neutron-rich matter or pure neutron matter, particularly the neutron skin. Our predictions (Chapter 3) are within presently available empirical constraints.

The equation of state of neutron-rich matter has recently been brought to the forefront of nuclear astrophysics due its relevance for the properties of neutron stars. Neutron stars are important natural laboratories for constraining theories of the equation of state, because the mass-radius relationship of these stellar objects has been shown to be sensitive to it. Our calculations and predictions of neutron star radii are presented in Chapter 4. We find them to be in good agreement

with recent observational constraints.

We conclude this work with our most recent effort, where we calculate the nuclear matter equation of state with the inclusion of subleading contributions to the chiral three-nucleon force. Additional studies related to this development are in progress.

Acknowledgements

I cannot adequately emphasize my appreciation and gratitude towards my advisor Dr. Francesca Sammarruca. Dr. Sammarruca's excellent guidance and tutelage has imparted to me the knowledge and skills necessary to successfully navigate the rigors of doctoral research. Her patience, kindness and belief in me has enabled my achievements and success, and without which I certainly would not have been able to complete my studies. Her first-rate instruction in the graduate courses of Classical Mechanics and Nuclear and Particle physics were instrumental to developing my understanding as a physicist and to building the foundation required to continuing my studies. Her continuous support, encouragement, open communication and patient explanations provided the scholastic environment for developing an understanding of the intricacies contained within this work. I am deeply indebted to Dr. Sammarruca and am sincerely grateful for her excellent work as my mentor.

I would like to give a special thanks to my committee member and instructor Dr. Ruprecht Machleidt. Dr. Machleidt's unparalleled quality in teaching Quantum Mechanics provided an important framework for my success throughout my graduate studies. His combined rigor, wit and lucid explanations made a tedious subject like quantum mechanics not only understandable but enjoyable. But more importantly I would like to thank Dr. Machleidt for his invaluable encouragement and support, for which I am deeply indebted and without which I never have been able to complete my studies.

I would like to thank my committee members Dr. Lyudmyla Barannyk and Dr. Andreas Vasdekis for their time and effort in working with me and on my committee during this especially difficult year. I would also like to thank Dr. Leah Bergman for her time on my committee. Additionally I would like to thank Dr. Bergman for her assistance and mentorship while I served as her assistant, her input and guidance gave me the framework necessary to successfully serve as an instructor.

I would like to acknowledge and thank my fellow physics cohorts and 301 comrades: Dr. Robert Chancia, Dr. Rajani Dhingra, Dr. Lokendra Khanal, Dr. Shahla Nemati and Dr. Negar Rajabi. You all were good friends and the best of study companions. The hours spent doing homework, preparing for the quals, laughing, joking and crying together will not be forgotten, I couldn't have done it without you guys. A very special thanks to Shahla for all of her support,

encouragement and advice.

I would like to acknowledge and thank all of my friends who provided support and encouragement throughout my time at the University of Idaho. Special thanks to Lt. Thomas Banks, Lt. John Corey, Lt. Sean Lawler and Lt. David Rutherford. Rest in peace David, you'll be missed. Special thanks to Eric Lynne, Taylor Jones and Ezra Dolezal. A special thanks to all of my family.

Financial support from the U.S. Department of Energy is gratefully acknowledged.

Table of Contents

Authorization to Submit Thesis	ii
Abstract	iii
Acknowledgements	v
Table of Contents	vii
List of Tables	ix
List of Figures	xi
Chapter 1: Introduction	1
Chapter 2: The Energy per Particle in Infinite Nuclear Matter	4
2.1 Introduction.....	4
2.2 The Brueckner-Bethe-Goldstone Method.....	5
2.2.1 The G-Matrix.....	6
2.2.2 Evaluating the Energy per Particle.....	7
2.3 QCD and Nuclear Forces: Some General Aspects.....	9
2.3.1 Chiral Effective Field Theory.....	10
2.3.2 Two-Nucleon Forces.....	13
2.3.3 Three-Nucleon Forces - N^2LO	14
2.3.4 Three-nucleon forces in the medium.....	15
Chapter 3: The Nuclear Equation of State From Chiral Nuclear Forces	21
3.1 Equations of state predictions for nuclear matter.....	21
3.1.1 Some basic definitions.....	21
3.1.2 Symmetric Nuclear Matter.....	22
3.1.3 Neutron Matter.....	25
3.2 Symmetry Energy.....	27

3.2.1	Basic Definitions and Phenomenological Properties of the Symmetry Energy ..	27
3.2.2	Symmetry Energy Predictions	29
3.2.3	Semi-Microscopic Symmetry Energy Predictions	32
3.3	Finite Nuclei	35
3.3.1	Energy-Density Functional Inspired by the Semi-Empirical Mass Formula	36
3.3.2	Symmetry Energy and the neutron skin.....	39
3.3.3	Predictions for Neutron Skins	41
Chapter 4:	The Nuclear Equation of State and Neutron Stars	43
4.1	General Aspects of Neutron Stars.....	43
4.1.1	Mass-Radius Relation.....	45
4.2	EoS for β -Stable Nuclear Matter	46
4.2.1	Particle Fractions	47
4.2.2	Predictions in β -Stable Matter	49
4.3	Radius of the Canonical-Mass Neutron Star.....	51
4.3.1	Polytropic extrapolation.....	51
4.3.2	The TOV Equation	53
4.3.3	Predictions for the Neutron Star Radius.....	56
Chapter 5:	Subleading contributions to the chiral three-nucleon force.....	58
5.1	Expressions for the long-range subleading chiral three-nucleon forces.....	58
5.2	The nuclear matter equation of state with three-nucleon forces at N ³ LO	68
Chapter 6:	Conclusion.....	70
References	72
Appendix A:	Deriving the EoS for β-Stable Matter	83
A.1	Electron Contributions.....	83
A.1.1	Muon Contribution.....	84
A.1.2	Evaluating Particle Fractions	85
Appendix B:	Numerical Tables of Results from Chapter 4.....	86

List of Tables

2.1	Values of the LECs $c_{1,3,4}$, c_D , and c_E for different orders of the 2NF in the χ EFT expansion, and the 3NF at N ² LO, and different values of the momentum-space cutoff Λ . The LECs $c_{1,3,4}$ are given in units of GeV ⁻¹ , while c_D and c_E are dimensionless. The numbers in parentheses indicate the error arising from the fitting procedure. In addition, we also show the value for the exponent n that appears in the regulator function of Eq. (2.25).	20
2.2	Same as Table 2.1, but including the 2PE 3NF at N ³ LO and N ⁴ LO. That is, at each order, the 2PE term of the 3NF is included summing up all contributions up to that order. (The N ² LO values are the same as in Table 2.1).	20
3.1	Saturation properties at three orders of the chiral expansion. The 3NF LECs used are found in Table 2.2. The truncation error is included in parenthesis. [83]	25
3.2	Saturation properties at three orders of the chiral expansion. The 3NF LECs used are found in Table 2.1. The truncation error is included in parenthesis. Note that the N ² LO values are the same as in Table 3.2 and are included for reference. [83]	25
3.3	Symmetry energy properties at three orders of the chiral expansion. The 3NF LECs are from Table 2.2. The truncation error is included in parenthesis [83]	32
3.4	Symmetry energy properties at three orders of the chiral expansion. The 3NF LECs employed here are found in Table 2.2. The truncation error is included in parenthesis [84]	35
3.5	The neutron skin (in fm) of ²⁰⁸ Pb as predicted with the chiral EoS.	41
3.6	As in Table 3.5, but for ⁴⁸ Ca.	41
3.7	The neutron skin (in fm) of ²⁰⁸ Pb obtained from the semi-microscopic model described in section 3.2.3.	42
3.8	As in Table 3.7, but for ⁴⁸ Ca.	42
4.1	Adiabatic indices, Γ_1 and Γ_2 , corresponding to the two matching densities, see Fig. 4.4. R is the radius, ρ_c is the central density, and v_s is the speed of sound in units of the speed of light.	57

B.1	β -stable EoS : N ² LO, $\Lambda = 450$ MeV.	86
B.2	β -stable EoS : N ² LO, $\Lambda = 500$ MeV.	87
B.3	β -stable EoS : N ³ LO, $\Lambda = 450$ MeV.	87
B.4	β -stable EoS : N ³ LO, $\Lambda = 500$ MeV.	88
B.5	β -stable EoS : N ⁴ LO, $\Lambda = 450$ MeV.	88
B.6	β -stable EoS : N ⁴ LO, $\Lambda = 500$ MeV.	89
B.7	$1.4 M_{\odot}$: N ² LO, $\Lambda = 450$ MeV.	90
B.8	$1.4 M_{\odot}$: N ² LO, $\Lambda = 500$ MeV.	91
B.9	$1.4 M_{\odot}$: N ³ LO, $\Lambda = 450$ MeV.	92
B.10	$1.4 M_{\odot}$: N ³ LO, $\Lambda = 500$ MeV.	93
B.11	$1.4 M_{\odot}$: N ⁴ LO, $\Lambda = 450$ MeV.	94
B.12	$1.4 M_{\odot}$: N ⁴ LO, $\Lambda = 500$ MeV.	95

List of Figures

2.1	Forces regrouped according to the chiral expansion. Note the appearance of three-body forces at N ² LO. The figure is from Ref. [59]	12
2.2	Topologies of the 3NF at N ² LO. Figure obtained from Ref. [51]	14
3.1	The EoS of symmetric nuclear matter obtained with cutoff $\Lambda = 450$ MeV. The dashed curves include only 2NF. (Note: N2LO is the first order at which 3NF appear.) The “I” and “II” labels denote choices of the LECs as in Tables 2.1 and 2.2, respectively.	23
3.2	The EoS of symmetric nuclear matter. The numbers 450 and 500 denote the cutoff, Λ , in MeV, with the corresponding predictions shown by the solid and dashed lines, respectively. LECs as in Table 2.2.	24
3.3	As in Fig. 3.2 but with LECs from Table 2.1	24
3.4	As in Fig. 3.1, but for the EoS of NM.	26
3.5	As in Fig. 3.2, but for the EoS of NM	26
3.6	As in Fig. 3.3, but for the EoS of NM.	27
3.7	The energy per particle for increasing degree of isospin asymmetry at N ³ LO and cutoff of 450 MeV [83]. 3NF LECs as in Table 2.2.	30
3.8	Symmetry energy at increasing orders and both values of the regulator. The 3NF LECs from are from Table 2.2.	30
3.9	As in Fig. 3.8 but with 3NF LECs as in Table 2.1.	31
3.10	Symmetry energy at the fourth and fifth orders predicted with the two different parameterizations of the 3NF. In each case, the results with both cutoffs are shown.	31
3.11	The EoS from the phenomenological study of Ref. [108] in comparison with the microscopic predictions, order by order [84].	33

3.12	The symmetry energy <i>vs.</i> density. The curves are obtained from the various microscopic EoS for NM at the indicated chiral orders and cutoff values, combined with the phenomenological EoS for SNM [108] as explained in the text. The additional predictions and various constraints are from: Ref. [109], dark green; Ref. [110], magenta contour; Refs. [111, 112], yellow and brown shaded areas. (The data points were extracted from the graphs assuming $\rho_0 = 0.16 \text{ fm}^{-3}$) [84].	34
4.1	A illustration of neutron star structure as understood from current models [173, 174].	45
4.2	Fractions of neutrons (n), protons (p), electrons (e), and muons (μ) as a function of density at three orders of the chiral expansion. The cutoff Λ is 450 MeV.	49
4.3	Pressure in β -stable nuclear matter at three orders of the chiral expansion and two values of the regulator.	50
4.4	Pressure spread resulting from the polytropic extrapolation of the β -stable EoS as described in the text. The interaction at N ³ LO with $\Lambda = 450$ MeV is used.	53
4.5	Mass vs. radius relation derived from the NM EoS at three orders of the chiral expansion with $\Lambda = 450$ MeV. The orange line marks a mass of $1.4 M_{\odot}$. The shaded overlay represents the constraints obtained from Ref. [178].	55
4.6	Same legend as in Fig. 4.5, except for the cutoff, which is equal to 500 MeV.	56
5.1	Black curve: the chiral EoS obtained with the 2NF and the 3NF at N ² LO. Red curve: 2NF and 3NF both at N ³ LO.	68
5.2	The chiral EoS at N ³ LO. The solid red line contains the 3NFs at N ² LO as well as the long-range 3NF effects at N ³ LO, the dashed red line contains only 3NFs at N ² LO, and the black line only contains 2NFs effects.	69

Chapter 1

Introduction

Understanding the interactions between nucleons (that is, protons and neutrons) and describing nuclear reactions and structure quantitatively has been a central focus of nuclear physics since its inception. The *ab initio* approach to a many-nucleon system requires the application of few-nucleon forces in the many-body theory. The ultimate test of the validity of the theory is then based on comparison between predictions and experimental data.

A very useful and convenient “test bench” for theoretical nuclear physics is infinite nuclear matter, which is an idealized system composed of protons and neutrons in equal concentrations interacting via nuclear forces in the absence of electromagnetic interactions. This system is characterized by the nuclear Equation of State (EoS), defined as the energy per nucleon in infinite matter as a function of density. The infinite nature of nuclear matter implies translation invariance, thus simplifying calculations. Furthermore, the EoS can be applied directly in studies of actual nuclear systems which adopt the local density approximation. Also, as we will discuss in depth, the nuclear EoS plays an outstanding role in studies of neutron stars.

In this work we derive the EoS based on the approach to nuclear matter known as the Bruckner-Hartree-Fock (BHF) method [1–9]. The BHF theory provides convergent solutions for in-medium interactions from realistic two-body nuclear potentials. A self-contained description of the method, as well as additional citations, are provided in Chapter 2.

Naturally, nuclear forces are a crucial input for nuclear matter calculations. The development of nuclear forces has a long history, including phenomenological models and those based on meson theory, which was historically a very important development. Extensive reviews of the meson theory of nuclear forces are cited in Chapter 2.

Our understanding of nuclear forces has evolved over the years, particularly with the realization that the underlying theory of strong interactions is Quantum Chromodynamics (QCD), where the interactions among quarks involves the “color” charge [60–62]. A truly fundamental theory of nuclear forces would have to be derived directly from the quark interactions via gluon exchange – unfortunately, still an unmanageable task.

Our main motivation is to develop and apply predictions of the EoS based on high-quality modern nuclear forces. Those are derived from Chiral Effective Field Theory (χ EFT). χ EFT is consistent with the symmetries of low-energy QCD, most notably the chiral symmetry [38–40]. Part of Chapter 2 will be devoted to reviewing how χ EFT provides the link between QCD and nuclear forces which are applicable in the low-energy regime and discuss the two- and three-nucleon chiral forces we employ in the many-body framework.

Previously, we defined nuclear matter as an infinite system with equal densities of protons and neutrons. More precisely, this is referred to as “symmetric nuclear matter.” Neutron-rich matter is then an infinite system with larger concentration of neutrons, and, of course, pure neutron matter refers to a system containing only neutrons. Up to date theoretical predictions of neutron-rich matter are particularly timely as this construct is the focus of on-going and planned experimental efforts. For instance, the PREX-II [121], CREX [122] and MESA [123] accelerator experiments seek to place high-precision constraints on the neutron radii and neutron skins of ^{48}Ca and ^{208}Pb . In Chapter 3, we will elaborate on the relation between neutron skins and the EoS of neutron-rich matter and show a variety of predictions.

The EoS of neutron-rich matter has recently been brought to the forefront of nuclear astrophysics due its relevance for calculating properties of neutron stars. Neutron stars are important natural laboratories for constraining theories of the EoS, because the mass-radius relationship of these stellar objects has been shown to be sensitive to the EoS. Recently, interest in these compact stars has increased considerably as we are now in the “multi-messenger era” of astrophysical observation. The recent GW170817 neutron star merger event has yielded new and independent constraints on the radius of the canonical mass neutron star [171, 172]. Chapter 4 is dedicated to the description of our calculations, and corresponding predictions, of neutron star properties based on our chirally constrained EoS for stellar matter.

We conclude this thesis with our most recent effort – the contributions arising from the sub-

leading long-range components of the three-nucleon chiral force. As for the leading chiral 3NF, the contributions are cast in terms of effective density dependent two-body potentials. We show the EoS predictions and observe satisfactory convergence at N³LO when accounting for leading and subleading three-nucleon forces.

Finally, in Chapter 6 we provide a brief summary of our methods and conclusions, which we link to work in progress and future plans.

Chapter 2

The Energy per Particle in Infinite Nuclear Matter

In this chapter we will discuss the theoretical underpinnings of the nuclear EoS employed throughout this work. We will begin with a discussion of the methodology and formalism behind the Bruckner-Hartree-Fock approach to nuclear matter which is the nuclear many-body framework we use to derive our EoS. We will then proceed to discuss the basic principles underlying the nuclear forces which are input into the many-body framework.

2.1 Introduction

Achieving an understanding of nuclear forces and how their interactions shape nuclear systems has been a quest at the heart of nuclear physics.

Although infinite nuclear matter is an idealized system, its EoS has proven to be a powerful tool for exploring nuclear interactions in the medium. Symmetric nuclear matter is composed of neutrons and protons in equal concentrations. Asymmetric nuclear matter, (in particular, neutron-rich matter), is characterized by the degree of neutron excess, with neutron matter, consisting of neutrons only, being the extreme case of neutron excess. From the theoretical standpoint, an infinite system presents the advantage of translational invariance. In this chapter, we will present the formalism we use to obtain the EoS microscopically from state-of-the-art nuclear forces.

As mentioned, we employ the approach to nuclear matter known as the Bruckner-Hartree-Fock (BHF) method. For a complete historical overview of the theory, the reader should consult Refs. [1, 3–7, 9]. The BHF theory has proven to be an effective method for addressing nuclear matter, providing a clear path towards the derivation of convergent solutions for in-medium interactions

from realistic two-body nuclear potentials.

Other approaches to nuclear matter include the relativistic extension of BHF, known as the Dirac-Brueckner-Hartree-Fock (DBHF) method. Comprehensive studies based on the DBHF scheme may be found in Refs. [10–17]. Variational methods have also been widely used to produce nuclear matter predictions which are similar to those produced from the BHF method when realistic nucleon-nucleon (NN) potentials are employed [18–21]. Phenomenological density-dependent forces, such as Skyrme or Gogny forces [22–24], have been used as well for exploring nuclear many-body systems. We will now proceed to briefly examine the key points of the BHF framework.

2.2 The Brueckner-Bethe-Goldstone Method

The goal of the Brueckner-Bethe-Goldstone method, typically referred to as Brueckner theory, is to calculate the ground state energy in a system of A nucleons from a perturbation series. To begin, we note that the total Hamiltonian of the system can be written as:

$$\mathcal{H} = H_0 + H_1 , \quad (2.1)$$

where the unperturbed Hamiltonian, H_0 , can be expressed in terms of a single particle potential, U [6]:

$$H_0 = \sum_i^A (T_i + U_i) , \quad (2.2)$$

whereas the perturbation H_1 can be written as

$$H_1 = \frac{1}{2} \sum_{i<j}^A V_{ij} - \sum_i^A U_i . \quad (2.3)$$

Here V_{ij} is the two-body nuclear potential, while the single-particle potential U is to be chosen in some convenient way so as to facilitate the convergence of the expansion. Note the total Hamiltonian does not depend on U :

$$\mathcal{H} = H_0 + H_1 = \sum_i^A T_i + \frac{1}{2} \sum_{i<j}^A V_{ij} , \quad (2.4)$$

although the choice of U will impact the convergence rate of the expansion [6].

Because the two-body nuclear potential is strongly repulsive at short distances, the expansion is written in terms of the reaction matrix, the so-called G matrix, which performs the “ladder” sum over all Pauli-allowed intermediate states of the two nucleons. The G matrix is solution of the Brueckner-Bethe-Goldstone integral equation:

$$G(\omega) = V + V \frac{Q}{\omega - H_0} G(\omega). \quad (2.5)$$

where ω is the two-nucleon starting energy and Q is the Pauli operator, which prevents scattering into occupied intermediate states.

We then obtain the energy per particle in nuclear matter from the reaction matrix as:

$$\frac{e}{A} = \langle T \rangle + \frac{1}{2A} \sum_{p,q \leq k_F} \langle pq | G(\omega) | pq - qp \rangle, \quad (2.6)$$

where $\langle T \rangle$ is the average single-particle kinetic energy and the second term is the average single-particle potential obtained as the sum of the interactions over antisymmetrized states. The factor 1/2 removes double counting of nucleon pairs.

A few key technical points concerning the solution of the integral equation and the evaluation of the energy per particle are provided in the next section.

2.2.1 The G-Matrix

It is convenient to express the momenta of the two nucleons in terms their center-of-mass and relative momenta:

$$\vec{P} = \frac{\vec{k}_1 + \vec{k}_2}{2}, \quad (2.7)$$

(note that this is actually 1/2 of the center-of-mass momentum, for reasons of convenience which become clear later on), and

$$\vec{q} = \frac{\vec{k}_1 - \vec{k}_2}{2}. \quad (2.8)$$

We then write the Bethe-Goldstone equation in terms of these variables [8]:

$$G(\vec{q}_0, \vec{q}, \vec{P}) = V(\vec{q}_0, \vec{q}) + \int d^3 \vec{q}' V(\vec{q}_0, \vec{q}') \frac{Q(\vec{P}, \vec{q}')}{E(\vec{P}, \vec{q}_0) - E(\vec{P}, \vec{q}')} G(\vec{P}, \vec{q}', \vec{q}). \quad (2.9)$$

Here, \vec{q}_0 , \vec{q}' and \vec{q} represent the initial, intermediate and final momentum, respectively, and E stands for the energy of the two nucleons. Using partial wave decomposition, we can write the G-matrix in terms of its partial wave components, $G_{LL'}^{JST}$:

$$G(\vec{q}_0, \vec{q}, \vec{P}) \propto \sum_{LL'STM} i^{(L'-L)} G_{LL'}^{JST}(q_0, q, P) Y_{LS}^{JM}(\hat{q}_0) Y_{L'S}^{JM}(\hat{q}). \quad (2.10)$$

The integral equation can therefore be explicitly reduced to a system of one-dimensional partial wave components [8]:

$$G_{LL'}^{JST}(q_0, q, P) = V_{LL'}^{JST}(q_0, q) + \frac{2}{\pi} \sum_l \int_0^\infty dq' (q')^2 \frac{V_{LL'}^{JST}(q_0, q') \bar{Q}(q', P) G_{LL'}^{JST}(q', q, P)}{E(q_0, P) - E(q', P)}, \quad (2.11)$$

where a similar decomposition has been applied to the two-body potential. Note that we have applied an angle average approximation to the Pauli operator, Q . Also, the angular dependence disappears from the energy denominator [8]. The above equation is solved for each partial wave using standard matrix inversion techniques.

2.2.2 Evaluating the Energy per Particle

As done previously, we define 1/2 of the total momentum and the relative momentum:

$$\vec{P} = \frac{\vec{k}_1 + \vec{k}_2}{2} \quad (2.12)$$

and

$$\vec{q}_o = \frac{\vec{k}_1 - \vec{k}_2}{2}, \quad (2.13)$$

implying that $\vec{P} \pm \vec{q}_o = \vec{k}_{1,2}$. (Note that these symmetric expressions for $\vec{k}_{1,2}$ are the reason for the definition in Eq. (2.7).)

The diagonal elements of the G-matrix, which contribute to the ground state energy of nuclear matter, are obviously obtained from:

$$\langle \vec{q}_o | G^P | \vec{q}_o \rangle = \langle \vec{q}_o | V | \vec{q}_o \rangle + \int d^3 q' \langle \vec{q}_o | V | \vec{q}' \rangle \frac{\bar{Q}(\vec{P}, \vec{q}', k_F)}{E(\vec{P}, \vec{q}_o) - E(\vec{P}, \vec{q}')} \langle \vec{q}' | G^P | \vec{q}_o \rangle, \quad (2.14)$$

where the two-particle energy is the sum of the single-particle energies:

$$E(\vec{P}, \vec{q}_o) = \epsilon(\vec{P} + \vec{q}_o) + \epsilon(\vec{P} - \vec{q}_o), \quad (2.15)$$

and

$$E(\vec{P}, \vec{q}') = \epsilon(\vec{P} + \vec{q}') + \epsilon(\vec{P} - \vec{q}'). \quad (2.16)$$

Note that the single-particle energy contains the single-particle potential, U , yet to be determined. Because the G-matrix depends on U , and U depends on G (see second term in Eq. (2.6)), a scheme must be applied to obtain a self-consistent solution. We start with parametrizing the single-particle energy in parabolic form:

$$\epsilon(\vec{k}) = \frac{k^2}{2m_N} + U(q) \approx \frac{k^2}{2m^*} + U_o, \quad (2.17)$$

where m_N is the nucleon mass and m^* and U_o are parameters to be determined. Clearly, the above equation implies that the single-particle potential also has an approximate parabolic form:

$$U(k) = \frac{q^2}{2} \left(\frac{m_N - m^*}{m_N m^*} \right) + U_o. \quad (2.18)$$

Starting with some initial values for m^* and U_o , we solve for the G-matrix and calculate the single-particle potential, which is again fitted to its parabolic approximation to obtain a new set of parameters. The procedure continues until convergence is achieved to the desired accuracy. The final single particle potential is then:

$$U(k_1) = \int d^3 k_2 \langle \vec{q}_o | G^P | \vec{q}_o \rangle. \quad (2.19)$$

The energy per particle can now be evaluated:

$$\frac{e}{A} = \langle T(k_1) \rangle_{(k_F)} + \langle U(k_1) \rangle_{(k_F)} , \quad (2.20)$$

where the averages are taken over the Fermi sea.

In the next sections, we will concentrate on the description of the nuclear forces, which constitute the input to the framework we have just outlined.

2.3 QCD and Nuclear Forces: Some General Aspects

There are essentially two approaches to the development of nuclear forces: microscopic and phenomenological. While phenomenological models have played an important role within the study of nuclear interactions and have been quite successful, they inherently do not attempt to explain nuclear phenomena from fundamental principles. For details on the history and current developments of nuclear forces from a phenomenological perspective see Refs. [25–28].

An important development in the theory of nuclear forces was meson theory. However, nuclear forces based on meson-theoretic approaches were essentially models, that is, not directly related to a fundamental theory of the underlying interactions among the constituents of hadrons. Extensive reviews of the meson theory of nuclear force can be found in Refs. [29–37].

It is now understood that the underlying theory of strong interactions is Quantum Chromodynamics (QCD). This section is primarily concerned with gaining insight into state-of-the-art nuclear forces constructed from the principles of χ EFT. For a comprehensive review of χ EFT, the nuclear potentials derived therefrom, current developments, and future challenges, see Refs. [38–58].

The fundamental theory of strong interactions is QCD, where the interaction among quarks involves the “color” charge [60–62]. Naturally, a true fundamental theory of nuclear forces would have to be derived directly from the quark interactions via gluon exchange. Unfortunately, this is an unmanageable task. While significant advances have been made in recent years, there is still a large gap in both theory and computational power before a working description of nuclear forces can be derived from QCD [63–66]. For instance, the simplest two-body system would now become a six-body problem due to the three-quark internal structure of nucleons.

The crucial feature of the interaction between colored particles is that it is weak at short distances, a phenomenon known as asymptotic freedom, but extremely strong at long distances,

namely at the low energies typical of nuclear physics. The quarks are therefore “locked in” in colorless objects – the hadrons – and the force between nucleons is a residual force from the complex interactions at the quark and gluon level. These considerations are crucial when identifying the appropriate degrees of freedom.

In this section we will start by briefly reviewing how χ EFT provides the link between QCD and nuclear forces which are applicable in the low-energy regime. We will then discuss the two- and three-nucleon chiral nuclear forces we employ in the many-body framework described in the preceding section.

2.3.1 Chiral Effective Field Theory

The first step in a development of an EFT is the identification of a “soft scale” and a “hard scale.” For this purpose, guidance can be found in the hadron spectrum, where a large separation exists between the mass of the pion and the mass of the vector meson ρ . Thus, we identify the pion mass as the soft scale while the mass of the ρ sets the hard scale, ≈ 1 GeV. Moreover, since quarks and gluons are ineffective degrees of freedom in the low-energy regime (see comments above), pions and nucleons are the appropriate degrees of freedom of the EFT.

We still have to make the connection between QCD and the EFT. This link is established through the symmetries of low-energy QCD. At this point, we can write the most general Lagrangian consistent with those symmetries (and their breaking). Following the prescription of the theory as expounded in Ref. [49], the QCD Lagrangian is given by:

$$\mathcal{L} = \bar{q}(i\gamma^\mu \mathcal{D}_\mu - \mathcal{M})q - \frac{1}{4} \mathcal{G}_{\mu\nu,a} \mathcal{G}_a^{\mu\nu} , \quad (2.21)$$

where ‘q’ is the quark field, \mathcal{D}_μ represents the gauge covariant derivative, \mathcal{M} is the quark mass matrix, and $\mathcal{G}_a^{\mu\nu}$ is the gluon strength field tensor.

Chiral symmetry is conservation of “handedness,” and is an exact symmetry for massless particles. Chiral symmetry occurs in the limit of vanishing quark masses, which amounts to dropping the quark mass matrix term in the above Lagrangian. In fact, such term is responsible for *explicit*

breaking of chiral symmetry, as can be seen from the following. The quark mass matrix,

$$\mathcal{M} = \begin{pmatrix} m_u & 0 \\ 0 & m_d \end{pmatrix} \quad (2.22)$$

can be recast in terms of the identity matrix and the third Pauli spin matrix:

$$\mathcal{M} = \frac{(m_u + m_d)}{2} \begin{pmatrix} 1 & 0 \\ 0 & 1 \end{pmatrix} + \frac{m_u - m_d}{2} \begin{pmatrix} 1 & 0 \\ 0 & -1 \end{pmatrix}. \quad (2.23)$$

Clearly, the first term respects isospin symmetry while the second term vanishes if the masses of the “up” and “down” quarks are equal – $m_d = m_u$. Thus, the small difference in the quark masses breaks isospin symmetry. On the other hand, the expression above breaks chiral symmetry explicitly as a result of the non-zero quark masses. However, since the masses of the “u” and “d” quarks are very small compared to typical hadronic masses, explicit breaking of chiral symmetry is a small effect.

Next, we need to address the *spontaneous* breaking of chiral symmetry, for which there is clear evidence in the hadron spectrum. The spontaneous breaking of a global (as opposed to local) symmetry is accompanied by the appearance of a so-called massless “Goldstone Boson.” The particle which fulfills these requirements is the pion, an isospin triplet pseudoscalar boson. The pion is light relative to the other mesons in the hadron spectrum but not massless, which is due to the explicit chiral symmetry breaking from the non-vanishing quark masses.

At this point, having identified pions and nucleons as the appropriate degrees of freedom, we can then proceed to construct the Lagrangian of the effective theory:

$$\mathcal{L}_{eff} = \mathcal{L}_{\pi\pi} + \mathcal{L}_{\pi N} + \mathcal{L}_{NN} + \dots \quad (2.24)$$

This effective Lagrangian is expanded in the form of the “soft scale” over the “hard scale”, $\frac{Q}{\Lambda_\chi}$. As mentioned earlier, Q is of the order of the pion mass, whereas Λ_χ is the energy scale of chiral symmetry breaking, approximately 1 GeV.

Through a scheme known as power counting, the most important contributions to the effective Lagrangian are accounted for first, with increasing order resulting in consistently smaller terms. While the expansion itself is, of course, infinite, at each order of the expansion we are assured that

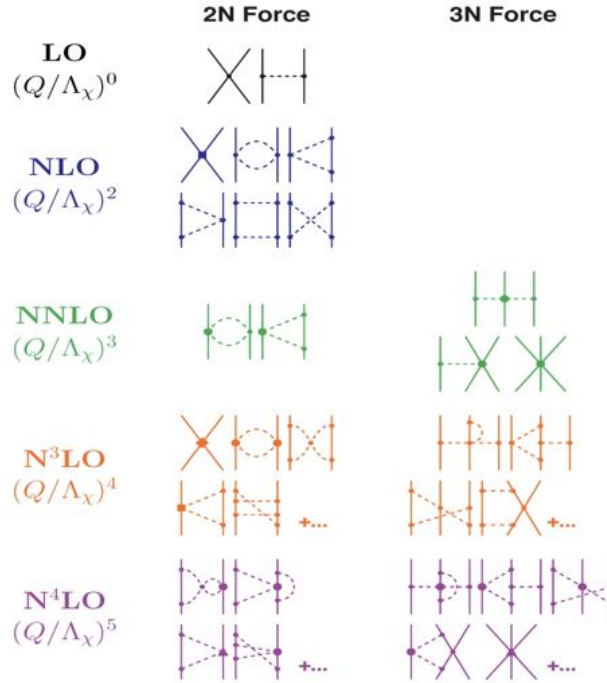


Figure 2.1: Forces regrouped according to the chiral expansion. Note the appearance of three-body forces at N²LO. The figure is from Ref. [59]

the number of terms is finite and well defined. This converts the issue of infinite expansion into a manageable problem [51].

Each order of the chiral expansion is associated to the maximum power of the expansion parameter $(\frac{Q}{\Lambda_\chi})^0$, denoted by ν . Thus, the first order is dubbed the Leading Order, or “LO”, being equivalent to the power $\nu = 0 : (\frac{Q}{\Lambda_\chi})^0$. Terms with $\nu = 1$ vanish due to symmetry reasons (they would violate conservation of parity). The group of terms corresponding to the next power in the expansion ($\nu = 2$) constitute the Next-to-Leading-Order (NLO); $\nu = 3$ is the Next-to-Next-to-Leading-Order (N²LO), and so on.

At the first two orders of the chiral expansion only two-body forces (2NF) are generated. At the third order (N²LO), three-body forces (3NF) appear for the first time.

In summary, we utilize potentials derived from χ EFT because:

1) Symmetries relevant to low-energy QCD are incorporated in the theory, in particular chiral symmetry. Thus, although the degrees of freedom are pions and nucleons instead of quarks and gluons, there exists a solid connection with the fundamental theory of strong interactions through its symmetries.

2) χ EFT employs a power counting scheme in which the progression of two and many-body nucleon forces is constructed in a clear and systematic manner. In this way the theory is internally consistent and the progression is well defined.

3) χ EFT treats two and many-body forces on equal grounds. This is very important, as it allows for a systematic inclusion of all 3NFs which appear at a given order, thus eliminating the inconsistencies which are unavoidable when adopting meson-theoretic or phenomenological forces.

4) Lastly, χ EFT provides a clear method for controlling the truncation error on an order-by-order basis. The latter can simply be expressed as the difference between the quantity computed at a given order of the chiral expansion and the one obtained at the next order.

We will now proceed to review the two and three-body chiral nuclear forces employed in this work.

2.3.2 Two-Nucleon Forces

In this work, we use chiral two-nucleon forces up to the fifth order of the chiral expansion (N^4 LO). The chiral potentials at N^4 LO are very accurate, yielding excellent reproduction of NN scattering data below approximately 290 MeV with a χ^2/datum equal to 1.15 [54] and the deuteron properties.

The long-range component of the interaction contains a set of low-energy constants (LECs) the values of which are determined in a very accurate Roy-Steiner analysis of π N scattering data [67]. The π N LECs precision is such that their resulting error is small enough to be ignored in the estimate of the overall uncertainty in the two-nucleon force [54, 67].

The short-range components of the chiral two-nucleon force are expressed through contact terms, while the long range part contains contributions from pion exchange (PE), ranging from one-pion exchange (1PE), found at all non-vanishing orders, to three-pion exchange (3PE), which appears for the first time at N^3 LO.

The NN system exhibits one (shallow) bound state, the deuteron. Furthermore, NN scattering lengths are large. These features make a perturbative calculation unfeasible and, therefore, the

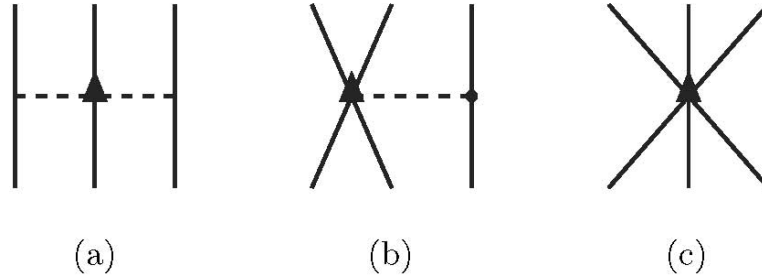


Figure 2.2: Topologies of the 3NF at $N^2\text{LO}$. Figure obtained from Ref. [51]

NN amplitude must be calculated from the T-matrix, solution of the Lippmann-Schwinger (LS) equation [49, 51]. Since high momentum components of the potential would produce divergences, a regulator function must be applied to the potential to cut out unwanted high-momenta prior to evaluating the T-Matrix. The regulator function has the typical form [51]

$$f(p', p) = \exp^{-[(p'/\Lambda)^{2n} - (p/\Lambda)^{2n}]}, \quad (2.25)$$

where p is the magnitude of the initial nucleon momentum and p' is the magnitude of the final nucleon momentum. Λ is the cutoff parameter, for which we chose a value of about 500 MeV, equal to about half of the hard scale. The choice of cutoff is based upon considerations of good perturbative behavior [51, 73]. Ideally, predictions should be independent of the cutoff, although in practice this is not the case. Achieving cutoff independence is known as “renormalization”. Different procedures have been suggested towards a renormalizable EFT, but this remains an open issue, see Refs. [51, 57] and references therein.

2.3.3 Three-Nucleon Forces - $N^2\text{LO}$

Prior $N^2\text{LO}$, 3NFs do not contribute. At $N^2\text{LO}$, there are three components (see diagrams in Fig. 2.2): a two-pion exchange term, a one-pion exchange term, and a contact term, contributing to the long-range, the medium-range, and the short-range, respectively.

The two-pion exchange (2PE) potential is given by [51, 70]:

$$V_{2\pi} = \frac{1}{8} \left(\frac{g_A}{f_\pi} \right)^2 \sum_{i \neq j \neq k} \frac{(\boldsymbol{\sigma}_i \cdot \mathbf{q}_i)(\boldsymbol{\sigma}_j \cdot \mathbf{q}_j)}{(q_i^2 + m_\pi^2)(q_j^2 + m_\pi^2)} F_{ijk}^{ab} \tau_i^a \tau_j^b, \quad (2.26)$$

where F_{ijk}^{ab} is defined as follows:

$$F_{ijk}^{ab} = \delta^{ab} [-4c_1 m_\pi^2 + 2c_3 \mathbf{q}_i \cdot \mathbf{q}_j] + c_4 \sum_c \epsilon^{abc} \tau_k^c \boldsymbol{\sigma}_k \cdot [\mathbf{q}_i \times \mathbf{q}_j]. \quad (2.27)$$

f_π is the pion decay constant equal to 94.4 MeV, g_A is dimensionless and is the scaled coupling constant with a value of 1.29, c_1 , c_3 and c_4 , are the LECs which appear within the NN chiral forces and thus are already fixed.

The 1PE contribution is given by [51, 70]:

$$V_{1\pi} = -\frac{g_A c_D}{8 f_\pi^4 \Lambda_\chi} \sum_{i \neq j \neq k} \frac{\boldsymbol{\sigma}_i \cdot \boldsymbol{\sigma}_j}{q_j^2 + m_\pi^2} (\boldsymbol{\tau}_i \cdot \boldsymbol{\tau}_j) (\boldsymbol{\sigma}_i \cdot \mathbf{q}_j), \quad (2.28)$$

while the contact contribution is [51, 70]:

$$V_{ct} = \frac{c_E}{2 f_\pi^4 \Lambda_\chi} \sum_{i \neq j \neq k} (\boldsymbol{\tau}_i \cdot \boldsymbol{\tau}_j). \quad (2.29)$$

In the above equations, Λ_χ is equal to 700 MeV and m_π is the average pion mass, equal to 138.04 MeV. The constants c_D and c_E are additional LECs which are constrained by fitting two observables within the few-nucleon system, typically ${}^3\text{H}$ or ${}^3\text{He}$ [48, 68, 69].

It has been shown [70] that, in nuclear matter, the original 3NFs displayed in this section can be expressed as density dependent contributions to the in-medium NN interaction. More details are given in the next section.

2.3.4 Three-nucleon forces in the medium

In Ref. [70], the genuine 3NFs at N²LO in nuclear matter are cast in the form of density-dependent two-body interactions. We will use those expressions, which can be easily incorporated in our nuclear matter framework.

First, we recall that the NN on-shell momentum space interaction has the general form:

$$\begin{aligned}
V(\vec{p}, \vec{q}) = & \left[V_C + (\vec{\tau}_1 \cdot \vec{\tau}_2) W_C \right] \\
& + \left[V_S + (\vec{\tau}_1 \cdot \vec{\tau}_2) W_S \right] \vec{\sigma}_1 \cdot \vec{\sigma}_2 \\
& + \left[V_T + (\vec{\tau}_1 \cdot \vec{\tau}_2) W_T \right] \vec{\sigma}_1 \cdot \vec{q} \vec{\sigma}_2 \cdot \vec{q} \\
& + \left[V_{SO} + (\vec{\tau}_1 \cdot \vec{\tau}_2) W_{SO} \right] i(\vec{\sigma}_1 + \vec{\sigma}_2) \cdot (\vec{q} \times \vec{p}) \\
& + \left[V_Q + (\vec{\tau}_1 \cdot \vec{\tau}_2) W_Q \right] (\vec{\sigma}_1 \cdot (\vec{q} \times \vec{p}) \vec{\sigma}_2 \cdot (\vec{q} \times \vec{p})) .
\end{aligned} \tag{2.30}$$

Here, V corresponds to the isoscalar component of the interaction and $(\vec{\tau}_1 \cdot \vec{\tau}_2)W$ corresponds to the isovector component of the interaction. C stands for central, S for spin-spin, T for tensor, SO for spin-orbit, and Q for quadratic spin-orbit.

The three nucleon effective potentials at N²LO for symmetric nuclear matter are expressed in terms of six NN density dependent contributions, which we give below. For a detailed derivation, see Ref. [70].

For clarity, we first regroup the values of some important constants [71]:

- $g_A = 1.29$,
- $f_\pi = 94.4$ MeV ,
- $M_N = 938.918$ MeV ,
- $m_\pi = 138.04$ MeV .

In the following, ρ is the density, while p is the nucleon momenta and q is the momentum transfer.

The 2PE term of the chiral 3NF generates three contributions from Pauli-blocking of the in-medium self-energy and vertex corrections:

$$V_{NN}^{med,1} = \left(\frac{g_A^2 M_N \rho}{8\pi f_\pi^4} \right) (2 c_1 m_\pi^2 + c_3 q^2) \vec{\tau}_1 \cdot \vec{\tau}_2 \frac{\vec{\sigma}_1 \cdot \vec{q} \vec{\sigma}_2 \cdot \vec{q}}{(m_\pi^2 + q^2)^2} , \tag{2.31}$$

$$V_{NN}^{med,2} = \left(\frac{g_A^2 M_N}{32\pi^3 f_\pi^4} \right) \vec{\tau}_1 \cdot \vec{\tau}_2 \frac{\vec{\sigma}_1 \cdot \vec{q} \vec{\sigma}_2 \cdot \vec{q}}{m_\pi^2 + q^2} , \tag{2.32}$$

and

$$\begin{aligned}
V_{NN}^{med,3} = & \left(\frac{g_A^2 M_N}{64\pi^3 f_\pi^4} \right) \left[-12c_1 m_\pi^2 [2\Gamma_0(p) - (2m_\pi^2 + q^2) G_0(p, q)] \right. \\
& - c_3 \left[8k_f^3 - 12(2m_\pi^2 + q^2) \Gamma_0(p) \right. \\
& \quad \left. - 6q^2 \Gamma_1(p) + 3(2m_\pi^2 + q^2)^2 G_0(p, q) \right] \\
& + 4c_4 \vec{\tau}_1 \cdot \vec{\tau}_2 (q^2 \vec{\sigma}_1 \cdot \vec{\sigma}_2 - \vec{\sigma}_1 \cdot \vec{q} \vec{\sigma}_2 \cdot \vec{q}) G_2(p, q) \\
& - (3c_3 + c_4 \vec{\tau}_1 \cdot \vec{\tau}_2) i(\vec{\sigma}_1 + \vec{\sigma}_2) \cdot (\vec{q} \times \vec{p}) \\
& \quad \times [2\Gamma_0(p) + 2\Gamma_1(p) - (2m_\pi^2 + q^2)(G_0(p, q) + 2G_1(p, q))] \\
& - 12c_1 m_\pi^2 i(\vec{\sigma}_1 + \vec{\sigma}_2) \cdot (\vec{q} \times \vec{p}) [G_0(p, q) + 2G_1(p, q)] \\
& + 4c_4 (\vec{\tau}_1 \cdot \vec{\tau}_2) (\vec{\sigma}_1 \cdot (\vec{q} \times \vec{p}) \vec{\sigma}_2 \cdot (\vec{q} \times \vec{p})) \\
& \quad \times (G_0(p, q) + 4G_1(p, q) + 4G_3(p, q)) \left. \right]. \tag{2.33}
\end{aligned}$$

The Γ functions are defined below:

$$\begin{aligned}
\Gamma_0(p) = & k_f - m_\pi \left[\arctan\left(\frac{k_f + p}{m_\pi}\right) + \arctan\left(\frac{k_f - p}{m_\pi}\right) \right] \\
& + \frac{m_\pi^2 + k_f^2 - p^2}{4p} \ln\left(\frac{m_\pi^2 + (k_f + p)^2}{m_\pi^2 + (k_f - p)^2}\right), \tag{2.34}
\end{aligned}$$

$$\begin{aligned}
\Gamma_1(p) = & \frac{k_f}{4p^2} (m_\pi^2 + k_f^2 + p^2) - \Gamma_0(p) \\
& - \frac{1}{16p^3} [m_\pi^2 + (k_f + p)^2] [m_\pi^2 + (k_f - p)^2] \ln\left(\frac{m_\pi^2 + (k_f + p)^2}{m_\pi^2 + (k_f - p)^2}\right), \tag{2.35}
\end{aligned}$$

$$\Gamma_2(p) = \frac{k_f^3}{9} + \frac{1}{6} (k_f^2 - m_\pi^2 - p^2) \Gamma_0(p) + \frac{1}{6} (m_\pi^2 + k_f^2 - p^2) \Gamma_1(p), \tag{2.36}$$

$$\Gamma_3(p) = \frac{k_f^3}{3p^2} - \frac{m_\pi^2 + k_f^2 + p^2}{2p^2} \Gamma_0(p) - \frac{m_\pi^2 + k_f^2 + 3p^2}{2p^2} \Gamma_1(p) , \quad (2.37)$$

while the $G_j(p, q)$ functions are defined as follows:

$$G_{\{0,*,**\}}(p, q) = \frac{2}{q} \int_0^{k_f} dk \frac{\{k, k^3, k^5\}}{\sqrt{A(p) + q^2 k^2}} \ln\left(\frac{qk + \sqrt{A(p) + q^2 k^2}}{\sqrt{A(p)}}\right) , \quad (2.38)$$

and the function $A(p)$ stands for:

$$A(p) \equiv \left[m_\pi^2 + (k + p)^2 \right] \left[m_\pi^2 + (k - p)^2 \right] . \quad (2.39)$$

The following G functions are defined in terms of Eq. 2.3.4 and the Γ functions defined above:

$$G_1(p, q) = \frac{\Gamma_0(p) - (m_\pi^2 + p^2) G_0(p, q) - G_*(p, q)}{4p^2 - q^2} , \quad (2.40)$$

$$G_{1*}(p, q) = \frac{3\Gamma_2(p) + p^2\Gamma_3(p) - (m_\pi^2 + p^2) G_*(p, q) - G_{**}(p, q)}{4p^2 - q^2} , \quad (2.41)$$

$$G_2(p, q) = (m_\pi^2 + p^2) G_1(p, q) + G_*(p, q) + G_{1*}(p, q) , \quad (2.42)$$

$$G_3(p, q) = \frac{0.5\Gamma_1(p) - 2(m_\pi^2 + p^2) G_1(p, q) - 2G_{1*}(p, q) - G_*(p, q)}{4p^2 - q^2} . \quad (2.43)$$

The 1PE generates contributions dependent on the parameter $\frac{cD}{\Lambda_\chi}$:

$$V_{NN}^{med,4} = - \left(\frac{g_A M_N c_D \rho}{32\pi f_\pi^4 \Lambda_\chi} \right) \vec{\tau}_1 \cdot \vec{\tau}_2 \frac{\vec{\sigma}_1 \cdot \vec{q} \vec{\sigma}_2 \cdot \vec{q}}{m_\pi^2 + q^2}, \quad (2.44)$$

and

$$\begin{aligned} V_{NN}^{med,5} = & \left(\frac{g_A M_N c_D}{64\pi^3 f_\pi^4 \Lambda_\chi} \right) \left[\vec{\tau}_1 \cdot \vec{\tau}_2 \left(2 \vec{\sigma}_1 \cdot \vec{\sigma}_2 \Gamma_2(p) \right. \right. \\ & + \left(\Gamma_0(p) + 2\Gamma_1(p) + \Gamma_3 \right) [\vec{\sigma}_1 \cdot \vec{\sigma}_2 (2p^2 - \frac{q^2}{2}) \\ & + \vec{\sigma}_1 \cdot \vec{q} \vec{\sigma}_2 \cdot \vec{q} (1 - \frac{2p^2}{q^2}) - \frac{2}{q^2} (\vec{\sigma}_1 \cdot (\vec{q} \times \vec{p}) \vec{\sigma}_2 \cdot (\vec{q} \times \vec{p}))] \Big) \\ & \left. + 4k_f^3 - 6 m_\pi^2 \Gamma_0(p) \right]. \end{aligned} \quad (2.45)$$

Finally, the short-range component of the chiral 3NF generates a contribution dependent on the constant, $\frac{c_E}{\Lambda_\chi}$:

$$V_{NN}^{med,6} = - \frac{3 M_N c_E \rho}{8\pi f_\pi^4 \Lambda_\chi}. \quad (2.46)$$

For a complete description of the contributions listed above the reader is referred to Ref. [70]. The LECs c_D and c_E which we use are determined *via* the three-nucleon system. They are constrained to reproduce the $A = 3$ binding energies and the Gamow-Teller matrix element of tritium β -decay through the procedure described in Refs. [48, 68, 69]. The regulator function applied to the 3NF is

$$f(q) = \exp^{[(-q/\Lambda)^4]}, \quad (2.47)$$

as in Ref. [74], with $q \equiv |\vec{p}' - \vec{p}|$ the momentum transfer.

The complete 3NF at orders higher than the third (N²LO) is very challenging, both in its development and applications, and, therefore, it is frequently excluded from nuclear structure studies. Note, though, that good progress is being made toward the inclusion of the subleading 3NF at N³LO [72, 75–79]. However, in Ref. [80] it was shown that the 2PE 3NF has nearly the same analytical structure at the third (N²LO), fourth (N³LO), and fifth (N⁴LO) orders. Thus, one can

Table 2.1: Values of the LECs $c_{1,3,4}$, c_D , and c_E for different orders of the 2NF in the χ EFT expansion, and the 3NF at N²LO, and different values of the momentum-space cutoff Λ . The LECs $c_{1,3,4}$ are given in units of GeV^{-1} , while c_D and c_E are dimensionless. The numbers in parentheses indicate the error arising from the fitting procedure. In addition, we also show the value for the exponent n that appears in the regulator function of Eq. (2.25).

	Λ (MeV)	n	c_1	c_3	c_4	c_D	c_E
N ² LO	450	2	-0.74	-3.61	2.44	0.935(0.215)	0.12(0.04)
	500	2	-0.74	-3.61	2.44	0.495(0.195)	-0.07(0.04)
N ³ LO	450	2	-1.07	-5.32	3.56	0.675(0.205)	0.31(0.05)
	500	2	-1.07	-5.32	3.56	-0.945(0.215)	-0.68(0.04)
N ⁴ LO	450	2	-1.10	-5.54	4.17	1.245(0.225)	0.28(0.05)
	500	2	-1.10	-5.54	4.17	-0.670(0.230)	-0.83(0.03)

Table 2.2: Same as Table 2.1, but including the 2PE 3NF at N³LO and N⁴LO. That is, at each order, the 2PE term of the 3NF is included summing up all contributions up to that order. (The N²LO values are the same as in Table 2.1).

	Λ (MeV)	n	c_1	c_3	c_4	c_D	c_E
N ² LO	450	2	-0.74	-3.61	2.44	0.935(0.215)	0.12(0.04)
	500	2	-0.74	-3.61	2.44	0.495(0.195)	-0.07(0.04)
N ³ LO	450	2	-1.20	-4.43	2.67	0.670(0.210)	0.41(0.05)
	500	2	-1.20	-4.43	2.67	-0.750(0.210)	-0.41(0.04)
N ⁴ LO	450	2	-0.73	-3.38	1.69	0.560(0.220)	0.46(0.05)
	500	2	-0.73	-3.38	1.69	-0.745(0.225)	-0.15(0.04)

parametrize the sum of all the three orders of 3NF contributions in terms of a set of effective LECs. In this way, at least for the very important 2PE component of the 3NF, complete calculations up to N⁴LO are possible. Tables 2.1 and 2.2 display a complete list of LECs with (Table 2.2) and without (Table 2.1) the 2PE contribution, respectively.

Chapter 3

The Nuclear Equation of State From Chiral Nuclear Forces

3.1 Equations of state predictions for nuclear matter

3.1.1 Some basic definitions

The nuclear matter equation of state is characterized by the energy per particle as a function of density, which we will denote by $e(\rho)$:

$$e(\rho) = \frac{E}{A}(\rho), \quad (3.1)$$

where E is the total energy of A nucleons. Here ρ is the total density of neutrons, n , and protons, p :

$$\rho = \rho_n + \rho_p. \quad (3.2)$$

Isospin is a quantum number that is conserved in strong interactions. Protons and neutrons are assigned an isospin quantum number of $\frac{1}{2}$, whereas the isospin projection along the quantization axis is $\frac{1}{2}$ for the proton and $-\frac{1}{2}$ for the neutron. Isospin, unlike spin, is dimensionless, but its formal properties are the same as those of the spin angular momentum “vector.”

The isospin asymmetry parameter, α , defined as:

$$\alpha \equiv \frac{\rho_n - \rho_p}{\rho_n + \rho_p} = \frac{\rho_n - \rho_p}{\rho}, \quad (3.3)$$

characterizes the degree of neutron excess (if positive) or deficiency (if negative) as a function of the nucleonic density. Clearly, $\alpha = 0$ corresponds to equal densities of protons and neutrons, while $\alpha = 1$ corresponds to pure neutron matter.

In the previous chapter we described the formalism for deriving the energy per particle at a given Fermi momentum, k_F . The Fermi momentum is simply related to the density by summing over normalized states in momentum space:

$$\rho = \gamma \int \frac{d^3k}{(2\pi)^3} = \frac{\gamma}{2\pi^2} \int_0^{k_F} k^2 dk = \gamma \frac{k_F^3}{6\pi^2}, \quad (3.4)$$

where γ is the total degeneracy, namely the number of nucleons which can share the same momentum state accounting for both isospin and spin. Thus, the degeneracy in isospin symmetric matter and pure neutron matter is equal to 4 and 2, respectively.

Throughout this chapter we will denote the energy per particle of isospin symmetric nuclear matter (SNM) by e_0 , while the energy per particle in neutron matter (NM) will be denoted by e_1 . Then, e_0 corresponds to $\alpha = 0$, while e_1 corresponds to $\alpha = 1$.

The nuclear force is a “saturated force,” which is why the density in the interior of nuclei is approximately constant. As a consequence, the energy per particle in SNM displays a minimum. The density at which the minimum occurs is referred to as “saturation density” and denoted by ρ_0 . The energy per particle in NM, on the other hand, increases monotonically with density. This is because the nuclear force, which is isospin dependent, produces no bound states in the nn system. Thus, no minimum of the energy per particle occurs in a system of neutrons.

As can be anticipated from the above discussion, the typical central density of nuclei is approximately equal to the saturation density, about 0.16 fm^{-3} (or $2.67 \cdot 10^{17} \frac{\text{kg}}{\text{m}^3}$ in S.I. units), with a corresponding energy per particle approximately equal to -16 MeV. These values are derived from fitting phenomenological models to large sets of nuclear data [81, 82].

3.1.2 Symmetric Nuclear Matter

Before proceeding to a discussion of our predictions in SNM, we take a small detour to address quantification of the chiral error. At each order of the chiral expansion, the truncation error should be a measure of what is neglected by terminating the chiral expansion at that order. When the

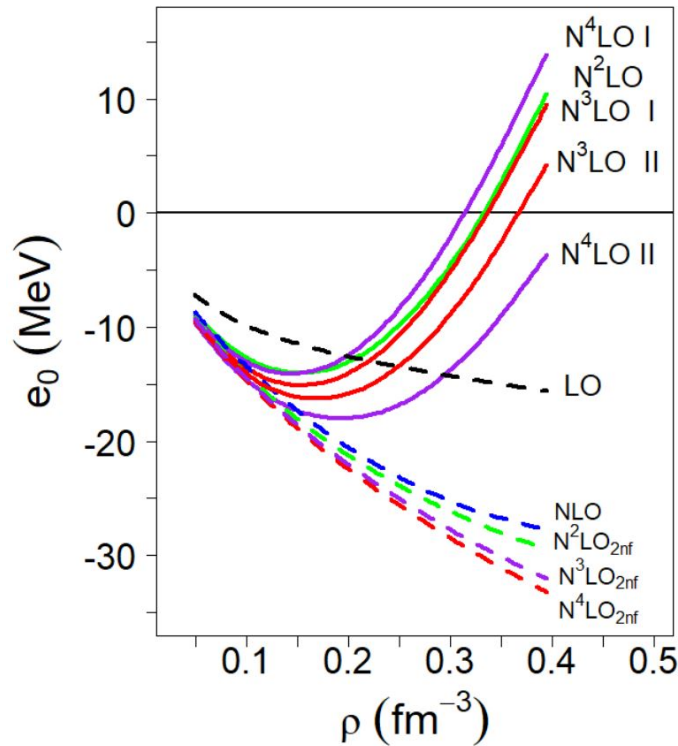


Figure 3.1: The EoS of symmetric nuclear matter obtained with cutoff $\Lambda = 450$ MeV. The dashed curves include only 2NF. (Note: N2LO is the first order at which 3NF appear.) The “I” and “II” labels denote choices of the LECs as in Tables 2.1 and 2.2, respectively.

prediction at, say, order $n + 1$ is known, the truncation error at order n can be simply expressed as

$$\bar{\epsilon}_n = |X_{n+1} - X_n|. \quad (3.5)$$

If the prediction at order $n+1$ is unknown, the following is a reasonable (pessimistic) prescription to estimate the error at order n :

$$\bar{\epsilon}_n \approx |X_n - X_{n-1}| \frac{Q}{\Lambda}, \quad (3.6)$$

where Q is a typical momentum of the system, and Λ is the cutoff parameter. Usually we restrict ourselves to values of 450 - 500 MeV, since this cutoff range is associated with better perturbative properties in applications.

In Fig. 3.1, we show the nuclear equation of state at five orders of the chiral expansion. The dashed curves are predictions which include only 2NF contributions. The labels “I” and “II” for the N³LO and N⁴LO cases denote the choice of 3NF LECs as given in Table 2.1 and 2.2, respectively.

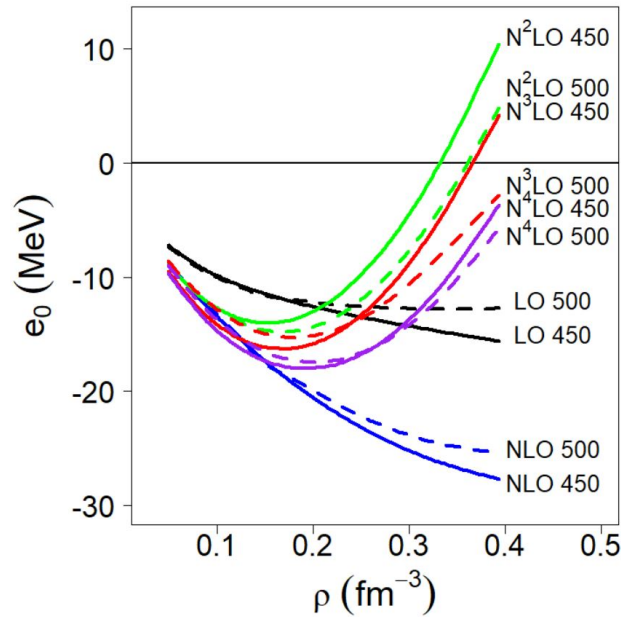


Figure 3.2: The EoS of symmetric nuclear matter. The numbers 450 and 500 denote the cutoff, Λ , in MeV, with the corresponding predictions shown by the solid and dashed lines, respectively. LECs as in Table 2.2.

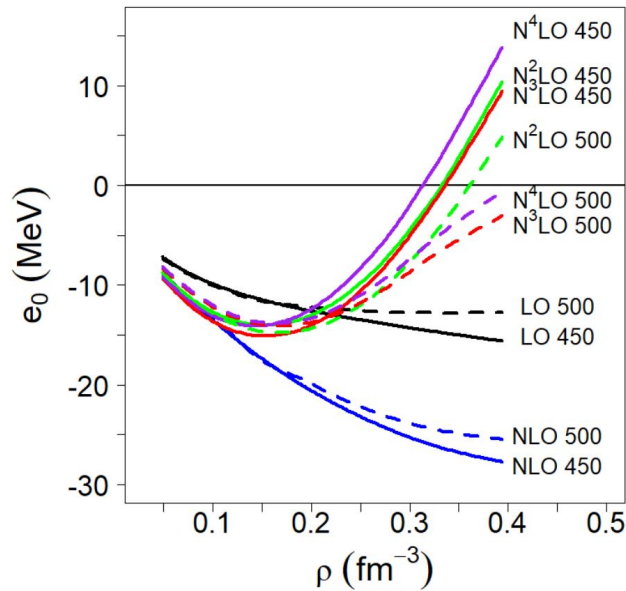


Figure 3.3: As in Fig. 3.2 but with LECs from Table 2.1

Their origin and significance was described in section 2.3.4. Clearly, inclusion of 3NF contributions is crucial for saturation. At $N^3\text{LO}$ and $N^4\text{LO}$, the EoS is very sensitive to the choice of the LECs.

In Figs. 3.2 and 3.3 we explore cutoff dependence for a particular choice of the LECs, case II and case I, respectively. In Fig. 3.2 we note larger truncation error, but comparatively smaller

Table 3.1: Saturation properties at three orders of the chiral expansion. The 3NF LECs used are found in Table 2.2. The truncation error is included in parenthesis. [83]

Order	Λ (MeV)	ρ_0 (fm $^{-3}$)	$e_0(\rho_0)$ (MeV)	K_0 (MeV)
N ² LO	450	0.155 (\pm 0.015)	-14.2 (\pm 2.3)	217.4 (\pm 3.6)
N ² LO	500	0.170 (\pm 0.010)	-14.9 (\pm 0.5)	214.4 (\pm 8.0)
N ³ LO	450	0.170 (\pm 0.025)	-16.4 (\pm 1.7)	221.2 (\pm 51.5)
N ³ LO	500	0.180 (\pm 0.023)	-15.4 (\pm 2.2)	206.4 (\pm 49.2)
N ⁴ LO	450	0.195 (\pm 0.012)	-18.1 (\pm 0.8)	272.7 (\pm 24.3)
N ⁴ LO	500	0.203 (\pm 0.010)	-17.6 (\pm 0.9)	255.6 (\pm 21.2)

Table 3.2: Saturation properties at three orders of the chiral expansion. The 3NF LECs used are found in Table 2.1. The truncation error is included in parenthesis. Note that the N²LO values are the same as in Table 3.2 and are included for reference. [83]

Order	Λ (MeV)	ρ_0 (fm $^{-3}$)	$e_0(\rho_0)$ (MeV)	K_0 (MeV)
N ² LO	450	0.155 (\pm 0.015)	-14.2 (\pm 2.3)	217.4 (\pm 3.6)
N ² LO	500	0.170 (\pm 0.010)	-14.9 (\pm 0.5)	214.4 (\pm 8.0)
N ³ LO	450	0.155 (\pm 0.011)	-15.2 (\pm 1.0)	220.6 (\pm 52.1)
N ³ LO	500	0.169 (\pm 0.001)	-14.2 (\pm 0.2)	207.0 (\pm 15.0)
N ⁴ LO	450	0.144 (\pm 0.005)	-14.2 (\pm 0.4)	180.3 (\pm 17.2)
N ⁴ LO	500	0.166 (\pm 0.001)	-14.0 (\pm 0.1)	222.0 (\pm 6.0)

cutoff error than observed in Fig. 3.3. In both cases, we see significant cutoff uncertainty in the high density region, as to be expected.

Table 3.1 contains the saturation properties as predicted at N²LO to N⁴LO, with the 3NF at N³LO and at N⁴LO treated as in case II. We observe that the energy per particle at saturation density varies within a range of about 4 MeV across all orders and cutoffs: $-14.2 \leq e_0 \leq -18.1$ MeV, while the saturation density spans a range of 0.048 fm^{-3} across all orders and both cutoffs: $0.155 \text{ fm}^{-3} \leq \rho_0 \leq 0.203 \text{ fm}^{-3}$. Table 3.2 contains similar information as Table 3.1 but for parametrization I of the 3NF at the fourth and fifth orders. In this case, the energy per particle at saturation spans about 1.2 MeV across all orders and cutoffs: $-14.0 \leq e_0 \leq -15.2$ MeV, while the saturation density varies within a range of 0.035 fm^{-3} : $0.144 \text{ fm}^{-3} \leq \rho_0 \leq 0.169 \text{ fm}^{-3}$. We conclude this section reiterating the importance of a consistent inclusion of the appropriate 3NF contributions at each order.

3.1.3 Neutron Matter

Here, we present a similar study as the one in the previous section, but for NM. Figure 3.4 is the analogous of Fig. 3.1. The dashed curves denote the EoS which only account for 2NF contributions.

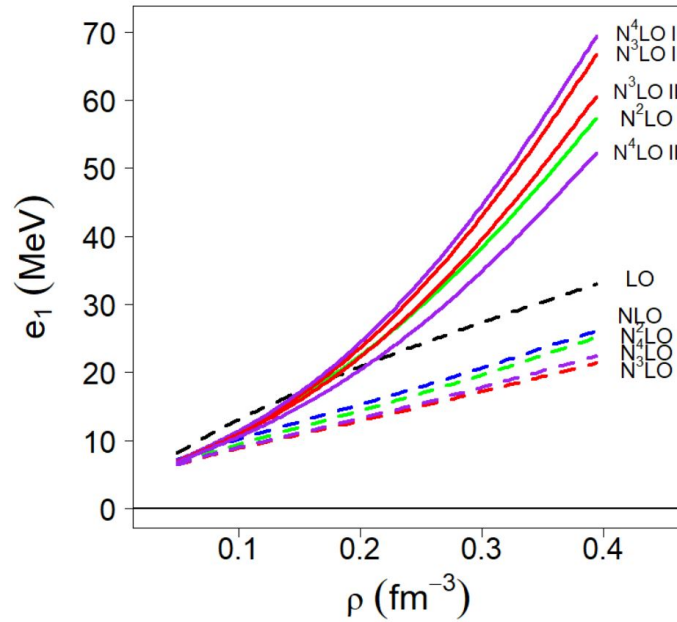


Figure 3.4: As in Fig. 3.1, but for the EoS of NM.

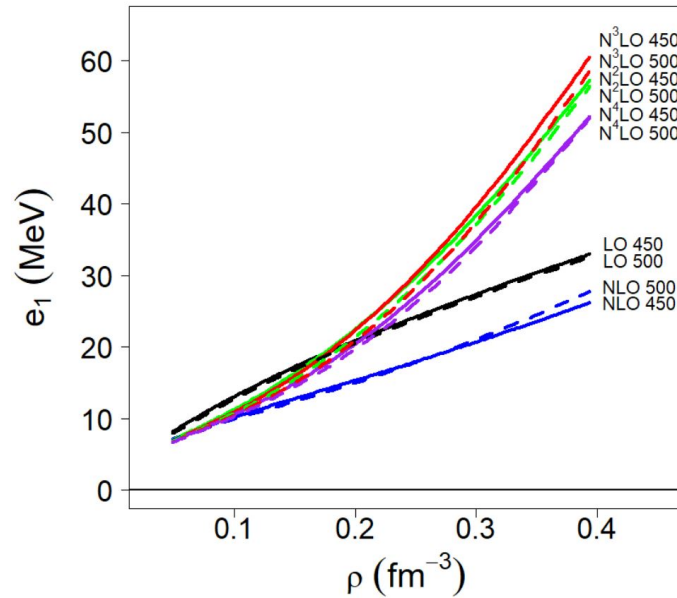


Figure 3.5: As in Fig. 3.2, but for the EoS of NM

We note excellent convergence of the 2NF curves, as observed for the SNM EoS. For the predictions which include 3NFs, the labels “I” and “II” have the same meaning as in the previous section. We note that significant, repulsive effects are produced by the inclusion of 3NFs in neutron matter.

From Figs. 3.5 and 3.6, a similar pattern as in the corresponding figures for SNM, Figs. 3.2 and 3.3, is seen with respect to cutoff dependence, although such dependence is weaker in NM.

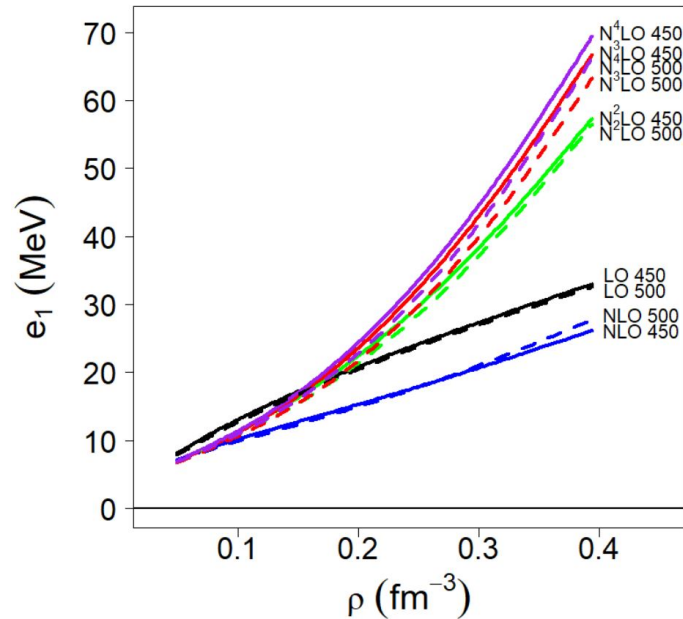


Figure 3.6: As in Fig. 3.3, but for the EoS of NM.

Figure 3.5 shows that cutoff dependence remains weak also at high densities. The reduced cutoff sensitivity in NM could be due to the absence of isospin-0 partial waves, which are large and present only in SNM [84]. Cutoff dependence is even weaker in Fig. 3.6. There, we also see a good order-by-order convergence pattern.

3.2 Symmetry Energy

3.2.1 Basic Definitions and Phenomenological Properties of the Symmetry Energy

We can express the EoS of isospin asymmetric matter, $e(\rho, \alpha)$, as a Maclaurin series expansion with respect to the isospin asymmetry parameter:

$$e(\rho, \alpha) = e(\rho, \alpha = 0) + \frac{1}{2} \left(\frac{\partial^2 e(\rho, \alpha)}{\partial \alpha^2} \right)_{(\alpha=0)} \alpha^2 + \mathcal{O}(\alpha^4). \quad (3.7)$$

Neglecting terms of order $\mathcal{O}(\alpha^4)$, Eq. (3.7) takes the parabolic form:

$$e(\rho, \alpha) \approx e_0 + e_{sym} \alpha^2, \quad (3.8)$$

where $e_{\text{sym}} = \frac{1}{2} \left(\frac{\partial^2 e(\rho, \alpha)}{\partial \alpha^2} \right)_{\alpha=0}$. If $\alpha = 1$, the symmetry energy (in the parabolic approximation) becomes the difference between the energy per particle in NM and the one in SNM:

$$e_{\text{sym}}(\rho) = e_1(\rho) - e_0(\rho) . \quad (3.9)$$

For comprehensive reviews on the symmetry energy and its role in neutron-rich systems, consult Refs. [85–88].

The Taylor expansion of the symmetry energy with respect to density about the saturation point helps identifying several useful parameters, whose physical meaning shall be discussed as they become relevant:

$$e_{\text{sym}}(\rho) \approx e_{\text{sym}}(\rho_o) + L \frac{\rho - \rho_o}{3\rho} + \frac{K}{2} \frac{(\rho - \rho_o)^2}{(3\rho)^2} . \quad (3.10)$$

L is referred to as the slope parameter, as it is a measure of the slope of the symmetry energy at saturation:

$$L = 3\rho_o \left(\frac{\partial e_{\text{sym}}(\rho)}{\partial \rho} \right)_{\rho_o} . \quad (3.11)$$

Furthermore, it is obvious from Eqs. (3.9) and (3.11) that L is a measure of the slope of the NM EoS at saturation density since the SNM EoS has a vanishing slope at that point, by definition of saturation. From a variety of phenomenological models, typical values for L are within 70 ± 15 MeV [86, 89–91]. A value closer to 50 MeV was obtained in Ref. [86].

The parameter K characterizes the curvature of the symmetry energy at saturation density:

$$K = 9 \rho_o^2 \left(\frac{\partial^2 e_{\text{sym}}(\rho)}{\partial \rho^2} \right)_{\rho_o} . \quad (3.12)$$

Note that a similar expansion of the energy per particle in SNM identifies the quantity

$$K_0 = 9 \rho_0^2 \left(\frac{\partial^2 e_0(\rho)}{\partial \rho^2} \right)_{\rho_0} \quad (3.13)$$

as a measure of the curvature of the EoS in SNM.

Correlations between physical observables and the symmetry energy and/or its derivatives have been explored mostly using families of phenomenological models. Popular examples are the Skyrme

forces or relativistic mean-field models (RMF) [105]. These models are parameterized so as to ensure that the empirical saturation properties are well described. Earlier investigations with a family of Skyrme interactions concluded that there is a linear correlation between the slope parameter and the neutron skin thickness of ^{208}Pb [94]. The neutron skin is defined as the difference between the root-mean square radii of the neutron and proton density distributions, a concept which will be elaborated on further when discussing nuclei. This intimate connection between the symmetry energy density derivative and the neutron skin of neutron-rich nuclei is of great interest. Accurate measurements of the skin would set stringent constraints on theoretical predictions of the L parameter.

Relativistic mean-field models predict a very wide range of L values, for example IU-FSU [92] gives a L value of 47.2 MeV, while NL3 [93] yields a value of 118.2 MeV for the same quantity. Naturally, these models also produce a large range of neutron skin values. For neutron skin predictions and RMF models, see also Ref. [106], where the authors utilize a large set of RMF models constrained through accurate fits of the nuclear binding energies and charge radii.

Extensive studies involving the correlations of the symmetry energy parameters and the symmetry energy at saturation density have been conducted using a variety of phenomenological and theoretical models [95–99]. Constraints on L vary considerably depending on the methods employed, with the most typical range found to be between 50 and 70 MeV [89, 100, 101, 124]. Constraints for the symmetry energy curvature are much weaker [102–104].

3.2.2 Symmetry Energy Predictions

We begin with showing the EoS for different levels of isospin asymmetry (or neutron excess), see Fig. 3.7, at N^3LO and cutoff equal to 450 MeV. Figure 3.8 displays the symmetry energy from third to fifth order and cutoff of 450 MeV and 500 MeV. The 3NF LECs from Table 2.2 are used. We note that there is very little truncation or cutoff error up to about $\rho = 0.2 \text{ fm}^{-3}$. In particular, the truncation error between the fourth and fifth chiral orders is remarkably small up to high density, especially for the cutoff of 450 MeV. Figure 3.9 displays the analogous comparison when the parameterization of the 3NF as in Table 2.1 is used instead. Similar comments apply as in Fig. 3.8. The difference between the fourth and fifth chiral orders is nearly zero.

From the observations above, regrouped for emphasis in Fig. 3.10, one may conclude that the

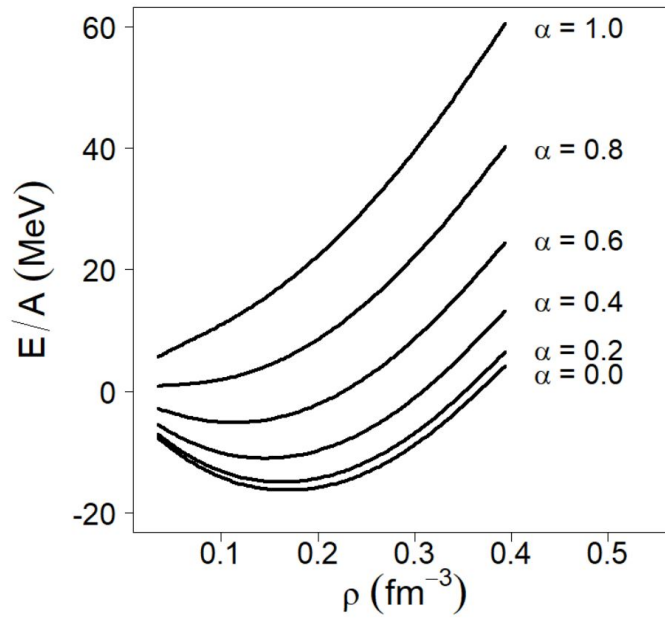


Figure 3.7: The energy per particle for increasing degree of isospin asymmetry at $N^3\text{LO}$ and cutoff of 450 MeV [83]. 3NF LECs as in Table 2.2.

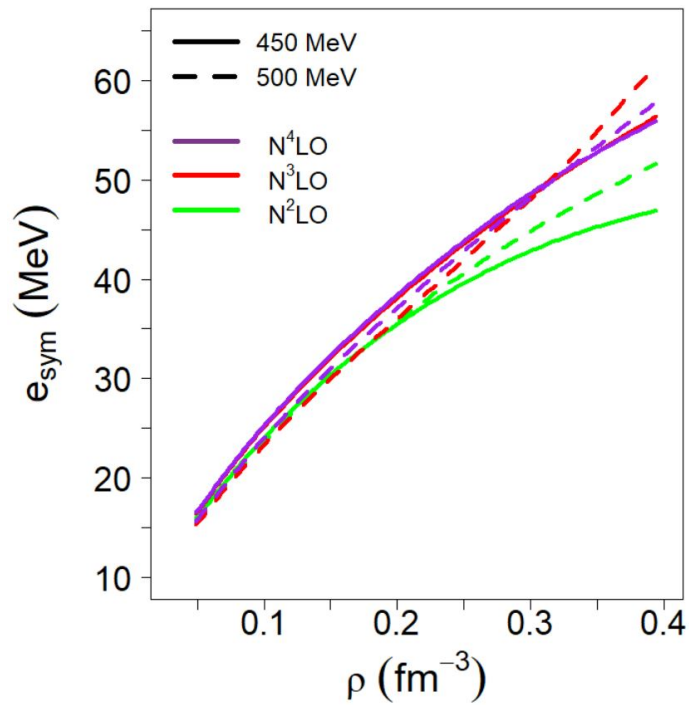


Figure 3.8: Symmetry energy at increasing orders and both values of the regulator. The 3NF LECs from are from Table 2.2.

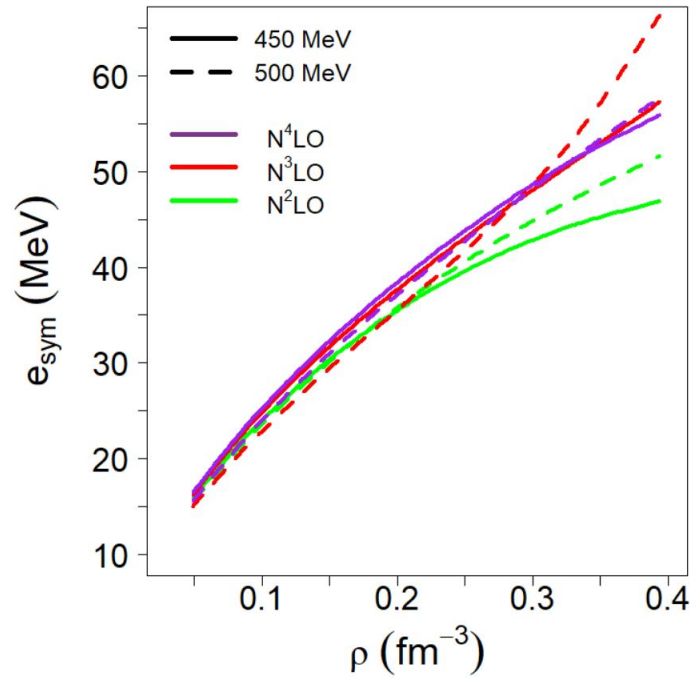


Figure 3.9: As in Fig. 3.8 but with 3NF LECs as in Table 2.1.

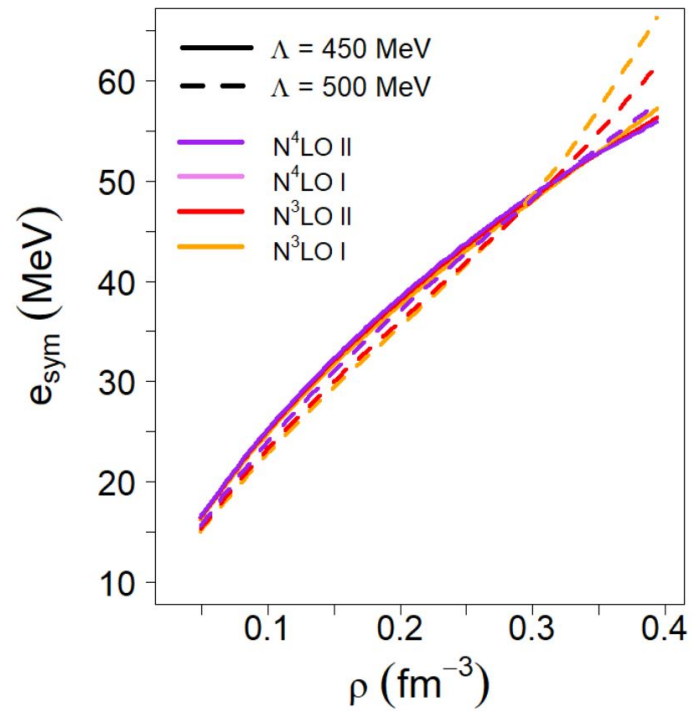


Figure 3.10: Symmetry energy at the fourth and fifth orders predicted with the two different parameterizations of the 3NF. In each case, the results with both cutoffs are shown.

Table 3.3: Symmetry energy properties at three orders of the chiral expansion. The 3NF LECs are from Table 2.2. The truncation error is included in parenthesis [83]

Order	Λ (MeV)	$e_{sym}(\rho_0)$ (MeV)	L (MeV)	K_{sym} (MeV)
$\overline{N}^2\text{LO}$	450	30.9 (± 3.6)	51.9 (± 10.7)	-93.2 (± 27.9)
	500	32.8 (± 1.1)	58.8 (± 6.4)	-85.0 (± 43.0)
$\overline{N}^3\text{LO}$	450	34.6 (± 3.2)	62.6 (± 5.9)	-65.3 (± 17.9)
	500	33.9 (± 3.9)	65.2 (± 6.9)	-42.0 (± 5.9)
$\overline{N}^4\text{LO}$	450	37.8 (± 1.5)	68.5 (± 3.0)	-83.2 (± 8.4)
	500	37.8 (± 1.7)	72.1 (± 2.8)	-47.9 (± 2.5)

predictions for the symmetry energy are quite similar for either choice of the LECs, which is in contrast to the behavior observed for isospin symmetric matter and neutron matter predictions individually. This may be due to cancellations, see Eq. (3.9).

In Table 3.3 we report predictions for the symmetry energy and related quantities. The predictions for the slope parameter can be stated as 62 ± 10.1 MeV, while the range for the incompressibility can be stated as -67.6 ± 25.6 MeV, including uncertainty from truncation and cutoff. For comparison, the corresponding values obtained with Skyrme density functionals are 65.4 ± 13.5 MeV for the slope parameter and -22.9 ± 73.2 MeV for the incompressibility [108].

Averaging over the cutoff, the results at $\overline{N}^3\text{LO}$ can be stated as follows (in MeV) [83]:

$$e_{sym}(\rho_0) = 34.3 \pm \Delta_{e_{sym}} \quad \Delta_{e_{sym}} = 3.6 \text{ (3.9)} , \quad (3.14)$$

$$L = 63.9 \pm \Delta_L \quad \Delta_L = 6.4 \text{ (6.9)} , \quad (3.15)$$

$$K_{sym} = -53.7 \pm \Delta_{K_{sym}} \quad \Delta_{K_{sym}} = 11.9 \text{ (17.9)} . \quad (3.16)$$

3.2.3 Semi-Microscopic Symmetry Energy Predictions

Up to this point, we discussed fully microscopic symmetry energy predictions. We already noted that the saturation properties predicted by the chiral interactions we are considering can differ substantially from one another, see Tables 3.1 and 3.2. The expansion parameters contained in Eq. (3.10) have been evaluated at the saturation density appropriate for that interaction, not at some common, nominal saturation density ρ_0 . On the other hand, as we mentioned earlier,

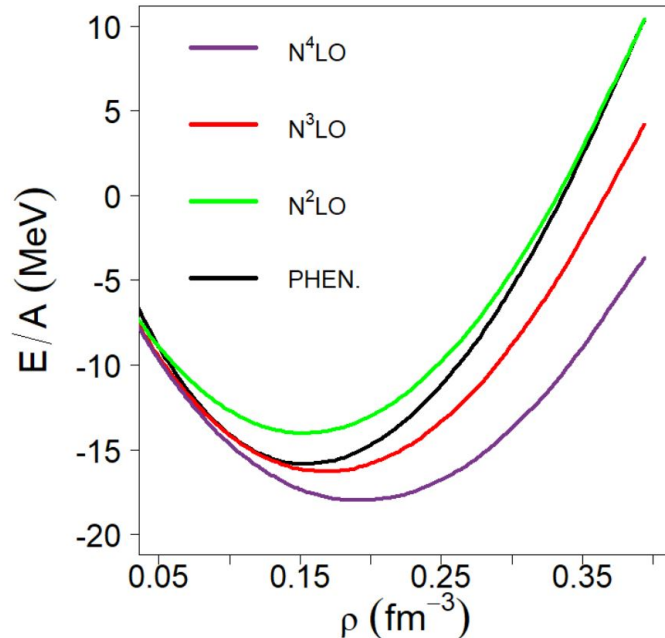


Figure 3.11: The EoS from the phenomenological study of Ref. [108] in comparison with the microscopic predictions, order by order [84].

analyses of correlations between the symmetry energy, its density slope, and the neutron skin thickness are typically done utilizing families of phenomenological models, such as large sets of Skyrme interactions or relativistic mean-field (RMF) models [105]. These models are constructed so as to have in common good saturation properties (usually by adjusting parameters to empirical properties of nuclei) while differing in the slope of the symmetry energy which, at saturation, is essentially a measure for the pressure in pure neutron matter. Our EoS are microscopic and parameter-free and our purpose is not to construct families of parameterized EoS models to establish phenomenological correlations. However, for the purpose of demonstration, next we wish to perform an analysis to “single out” the role of neutron matter pressure for the neutron skin thickness. For that purpose, we remove the uncertainty associated with the saturation point in SNM by constructing a “semi-microscopic” model of asymmetric matter as follows: for the symmetric part, we will use an established phenomenological EoS, such as the one from Ref. [108], whereas for the neutron matter portion – currently our focal point – we will continue to use the microscopic chiral EoS presented in Sec. 3.1.3.

In Fig. 3.11 we see the phenomenological SNM EoS compared to the microscopic predictions.

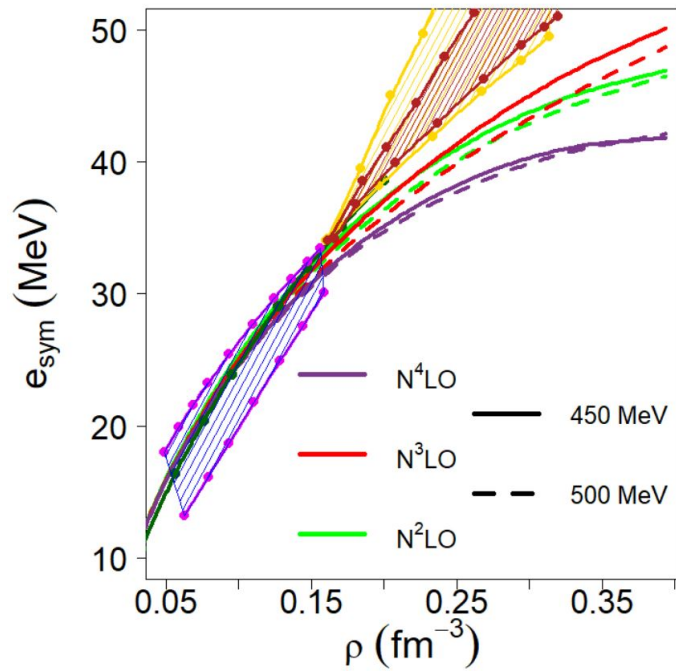


Figure 3.12: The symmetry energy *vs.* density. The curves are obtained from the various microscopic EoS for NM at the indicated chiral orders and cutoff values, combined with the phenomenological EoS for SNM [108] as explained in the text. The additional predictions and various constraints are from: Ref. [109], dark green; Ref. [110], magenta contour; Refs. [111, 112], yellow and brown shaded areas. (The data points were extracted from the graphs assuming $\rho_0 = 0.16 \text{ fm}^{-3}$) [84].

Table 3.4: Symmetry energy properties at three orders of the chiral expansion. The 3NF LECs employed here are found in Table 2.2. The truncation error is included in parenthesis [84]

Order	Λ (MeV)	$e_{sym}(\rho_0)$ (MeV)	L (MeV)	K_{sym} (MeV)
N ² LO	450	32.8 (± 0.4)	52.2 (± 0.8)	-117.6 (± 36.1)
	500	32.2 (± 0.1)	50.2 (± 1.5)	-106.3 (± 31.1)
N ³ LO	450	32.4 (± 1.0)	53.0 (± 7.2)	-81.5 (± 32.8)
	500	31.7 (± 0.6)	48.8 (± 4.6)	-75.2 (± 32.8)
N ⁴ LO	450	31.4 (± 0.5)	45.8 (± 3.1)	-114.3 (± 14.3)
	500	31.1 (± 0.2)	44.2 (± 1.8)	-108.0 (± 12.9)

We note considerable variations of the saturation point around the empirical values of $e_0 = -16 \pm 0.1$ MeV and $\rho_0 = 0.155 \pm 0.008 \text{ fm.}^{-3}$ In Fig. 3.12 we show our predictions for the symmetry energy in comparison with those from a variety of phenomenological models and empirical constraints. There is a general agreement of the symmetry energy predictions up to saturation density, after which our chiral predictions are significantly softer than those from the phenomenological models.

Table 3.4 contains predictions for the symmetry energy parameters obtained with the microscopic NM EoS and the phenomenological SNM EoS. As to be expected, we note that the range of values for both the symmetry energy at saturation and the slope parameter are more constrained than those in Table 3.3.

The average values at N³LO (with the ‘‘hybrid’’ model used in this section), accounting for truncation error and cutoff uncertainty, are given below in MeV [84]:

$$e_{sym}(\rho_0) = 32.1 \pm \Delta_{e_{sym}} \quad \Delta_{e_{sym}} = 1.0 , \quad (3.17)$$

$$L = 53.0 \pm \Delta_L \quad \Delta_L = 7.2 , \quad (3.18)$$

$$K_{sym} = -78.4 \pm \Delta_{K_{sym}} \quad \Delta_{K_{sym}} = 32.8 . \quad (3.19)$$

3.3 Finite Nuclei

So far we have discussed the chiral EoS predictions for infinite nuclear matter. However, to gain further insights into the chiral EoS, it is useful to include finite nuclei in the discussion. In

particular, as mentioned above, there is an important connection between the neutron skin of nuclei and the symmetry energy.

For this purpose we will employ an energy-density functional inspired by the well-known semi-empirical mass formula (SEMF) which assumes a spherically symmetric nucleus. In this way, we can evaluate the energy per particle in nuclei in a manner that is inherently connected to the chiral EoS.

3.3.1 Energy-Density Functional Inspired by the Semi-Empirical Mass Formula

With the SEMF as a guideline, we write the total energy of a given nucleus (Z, A) as:

$$E(Z, A) = \int d^3r \rho(r) e(\rho, \alpha) + \int d^3r f_o |\nabla \rho|^2 + \frac{e^2}{4\pi\epsilon_o} (4\pi)^2 \int_0^\infty dr' [r' \rho_p(r')] \int_0^{r'} dr r^2 \rho_p(r) . \quad (3.20)$$

The energy per nucleon is simply the total energy of the nucleus, $E(Z, A)$, divided by the atomic mass number, A :

$$e = \frac{E(Z, A)}{A} . \quad (3.21)$$

The density $\rho(r)$ is expressed as a function of the distance from the center of the nucleus, r . The isospin asymmetry parameter, α , was defined in Eq. (3.3).

Analyzing the formula term by term, we note that the first term – the “volume” term – represents the energy of an infinite system:

$$E_v = \int d^3r \rho(r) e(\rho(r), \alpha) . \quad (3.22)$$

The second term,

$$E_s = \int d^3r f_o |\nabla \rho(r)|^2 , \quad (3.23)$$

simulates surface effects, which depend on the density gradient. The constant, f_o , has been found to be between 60 and 72 MeV fm⁻⁵ from fits to nuclear data [117]. Varying the constant f_o across this range introduces an additional uncertainty of about 0.01 fm in calculations of the radius. We will use an average value of 65 MeV fm⁻⁵ for f_o throughout this section. (See Ref. [84] for additional

discussion.) We note that a contribution depending on the isovector density ($\rho_n - \rho_p$) has been left out in Eq. (3.23) because its effect was found to be negligible [113].

Naturally, a realistic description of nuclei requires inclusion of the Coulomb energy, which is not part of the energy per particle in the strongly interacting system defined as infinite nuclear matter. (In fact, nuclear matter is the result of an extrapolation from finite nuclei when Coulomb and finite-size effects are removed.) We account for the Coulomb energy, E_C , through the expression:

$$E_C = \frac{e^2}{4\pi\epsilon_0} (4\pi)^2 \int_0^\infty dr' [r' \rho_p(r')] \int_0^{r'} dr r^2 \rho_p(r). \quad (3.24)$$

The integral in Eq. 3.24 is straightforward and yields the electrostatic potential energy of a charged sphere.

Next, we model the nuclear density distribution as a function of radial distance using the well-established two-parameter Thomas-Fermi distribution:

$$\rho_i = \frac{\rho_a}{1 + e^{(r-b_i)/c_i}}, \quad (3.25)$$

where ρ_a is a normalization constant and $i = (n, p)$. The constants b and c are the radius and the diffuseness parameter, respectively. Thus for each species of particle (neutron/proton), there are two parameters to be determined, totaling four parameters to describe the density distribution a given nucleus (A, Z) .

To summarize, the numerical procedure to obtain both the energy and the neutron and proton density distributions of a given nucleus, (A, Z) , is: 1) An EoS, together with the atomic and mass numbers a given nucleus, (A, Z) , and four starting parameters $(b_{p_o}, c_{p_o}, b_{n_o}, c_{n_o})$ are input into the program. 2) Using a Nelder-Mead optimization algorithm, the minimum of the energy-density functional is obtained. This corresponds to minimizing the energy, E , with respect to the Thomas-Fermi density parameters. The four density parameters, (b_p, c_p, b_n, c_n) are the degrees of freedom of the minimization algorithm. 3) The optimal parameters are those which give the minimum of the energy.

The average radii of the neutron and proton density distributions are the quantum mechanical

root-mean-square radii:

$$R_i = \sqrt{\langle (r_i)^2 \rangle} = \sqrt{\frac{4\pi}{T_i} \int_0^\infty \rho_i(r) \cdot r^4 dr}, \quad (3.26)$$

where $T_{n,z} = N, Z$ respectively. R_n is the neutron radius, while R_p is the proton radius.

Another quantity of interest is the charge radius, which is the average radius determined from the charge distribution. The physical interpretation of the charge radius is a folding of the point proton density with the finite charge distribution of the proton itself, which is not point-like:

$$r_{ch}^2 = \frac{4\pi}{Z} \int_0^\infty \frac{2}{a\sqrt{\pi}} r^4 dr \int_0^\infty \frac{r'}{r} \rho_p(r') \sinh\left(\frac{2r r'}{a^2}\right) e^{-[(\frac{r'}{a})^2 + (\frac{r}{a})^2]} dr'. \quad (3.27)$$

In Eq. (3.3), we defined the symmetry energy in terms of the energy per particle in neutron matter and in symmetric matter. The *average* isospin asymmetry of a given nucleus with N neutrons and Z protons is:

$$\alpha_{ave.} \equiv \frac{N - Z}{N + Z} = \frac{N - Z}{A}. \quad (3.28)$$

Substituting Eq. (3.8) in Eq. (3.20) and recalling that, in the liquid droplet model, the term associated with the isospin asymmetry of the nucleus is written as $a_{sym} \frac{(N-Z)^2}{A}$, where a_{sym} is known as the symmetry energy coefficient, naturally leads to the definition:

$$a_{sym}(A, Z) = \frac{A}{(N - Z)^2} \int \rho(r) e_{sym}(\rho(r)) \alpha^2 d^3r. \quad (3.29)$$

The reference density, ρ_1 , is the density for which the symmetry energy is equal to the symmetry energy coefficient for a given nucleus:

$$e_{sym}(\rho_1) = a_{sym}(A, Z). \quad (3.30)$$

The relation above is of relevance, because it can potentially be used to constrain the symmetry energy around ρ_1 from the knowledge of the symmetry energy coefficient in nuclei. The latter can be obtained from fitting a liquid droplet model to nuclear data.

3.3.2 Symmetry Energy and the neutron skin

As mentioned above, a quantity of particular interest is the neutron skin, which is defined as the difference in neutron and proton *r.m.s.* radii:

$$S_n = \sqrt{\langle (r_n)^2 \rangle} - \sqrt{\langle (r_p)^2 \rangle} = R_n - R_p . \quad (3.31)$$

For nuclei with $N = Z$, the simplest approximation is to take $R_n \approx R_p$, although the proton radius is slightly larger due to the electrostatic repulsion. On the other hand, for neutron-rich nuclei, some of the excess neutrons are pushed away from the neutron-enriched core, as such configuration is energetically favorable. In fact, the formation of the neutron skin can be described as due to a pressure gradient, known as the *symmetry pressure*:

$$P_{sym} = \rho^2 \frac{de_{sym}}{d\rho} = P_{NM} - P_{SNM} , \quad (3.32)$$

where the derivative is evaluated at ρ_0 . As the pressure in SNM vanishes at saturation, the symmetry pressure is essentially the pressure in NM:

$$P_{NM} = \left(\rho^2 \frac{de_1}{d\rho} \right)_{\rho_0} . \quad (3.33)$$

Together with Eq. (3.11), it is then clear that the pressure at saturation density correlates with the slope parameter L which, in turn, correlates with the neutron skin.

As previously mentioned, families of phenomenological models have consistently demonstrated a strong correlation between the neutron skin of ^{208}Pb and the slope parameter. For instance, in Refs. [105, 106], the correlation between the neutron skin in ^{208}Pb and the slope parameter was examined for a large collection of RMF models and a 98% degree of correlation was found. For further details on the relationship of the slope parameter and the neutron skin of ^{208}Pb consult Refs. [106, 124–130] Since the neutron skin is of such interest, there are numerous historical and on-going experimental efforts to measure its value. However, this quantity is difficult to determine since it must be inferred from precision experiments where controlling errors remains a major challenge [114, 116].

However, the prospects for the near future are encouraging. For example, using the parity-violating weak interaction in electron-nucleus scattering, the ratio of right-hand scattered electrons to left-handed electrons can reveal information on the charge distribution within the nucleus [120]. The on-going PREX-II [121] and CREX [122] experiments, which exploit this phenomenon, seek to constrain the value of the neutron skin of ^{208}Pb and ^{48}Ca to within ± 0.06 fm and ± 0.02 fm, respectively. It is worth noting for comparison, that the first PREX experiment provided the neutron skin constraints of $0.33 (+0.16, -0.18)$ fm [115], the error was larger than initially intended due to technical complications, which are addressed in current experiments [121]. Additionally, the MESA accelerator in Mainz is planning to conduct experiments [123] to constrain the neutron skin of ^{208}Pb and ^{48}Ca within ± 0.03 fm and ± 0.02 fm, respectively. The ^{208}Pb and ^{48}Ca nuclei have been studied extensively due to the fact that they are the only neutron-rich nuclei having full nuclear shells (containing double “magic numbers” of neutrons and protons) and thus can be treated as spherically symmetric.

The existence of neutron “drip lines” is also linked to the neutron/proton asymmetry in nuclei. Nuclei with extreme neutron excess eventually become so weakly bound that the outermost neutrons begin to “drip”. The degree of neutron excess where neutrons in nuclei of a particular isotopic chain become unbound defines the location of the neutron drip lines on the nuclear chart [107, 117]. The neutron drip lines are currently unknown for elements above neon and this is because it is not experimentally feasible to produce elements with extremely high neutron excess before decay occurs [119]. Our group has performed a preliminary analysis of neutron drip lines based on chiral forces [118] and we plan to extend those studies. However, at this time, parity-violating electron-nucleus scattering offers the best prospect for constraining the slope of the symmetry energy, because the relevant weak interaction observables are under solid theoretical control.

Neutron stars are a unique “laboratory” for nuclear astrophysics. Some of the mechanisms governing the structure of neutron-rich nuclei are at play within neutron stars and this is readily observed in the correlation between the neutron skin of ^{208}Pb and the typical radius of the neutron star [106, 120, 131–133]. Since the nuclear EoS is the crucial input for the evaluation of both quantities, constraints on the neutron skin can provide theoretical constraints on neutron stars radii. This remarkable connection between objects differing in scale by eighteen orders of magnitude establishes a unique partnership between nuclear physics and nuclear astrophysics. The radius of

Table 3.5: The neutron skin (in fm) of ^{208}Pb as predicted with the chiral EoS.

Order	$\Lambda = 450 \text{ MeV}$	$\Lambda = 500 \text{ MeV}$
$\bar{\text{N}}^2\text{LO}$	0.133 ± 0.010	0.140 ± 0.005
N^3LO	0.143 ± 0.007	0.145 ± 0.011
N^4LO	0.150 ± 0.004	0.156 ± 0.006

Table 3.6: As in Table 3.5, but for ^{48}Ca .

Order	$\Lambda = 450 \text{ MeV}$	$\Lambda = 500 \text{ MeV}$
$\bar{\text{N}}^2\text{LO}$	0.132 ± 0.011	0.134 ± 0.002
N^3LO	0.143 ± 0.005	0.136 ± 0.006
N^4LO	0.138 ± 0.002	0.142 ± 0.002

the canonical-mass neutron star is sensitive to the pressures at saturation density and thus correlates with the slope parameter in a similar fashion as the neutron skin of neutron-rich nuclei. The mass-radius relationship for neutron stars as predicted from the chiral EoS will be discussed in the next chapter.

3.3.3 Predictions for Neutron Skins

We now turn to nuclei predictions as generated from the chiral EoS through the energy-density functional discussed in section 3.3.1. In Table 3.5 we show the prediction for the neutron skin of ^{208}Pb as derived from the EoS at three orders of the chiral expansion, while Table 3.6 shows the predictions for ^{48}Ca . Overall, the results cover a range of $0.133 \text{ fm}^{-3} \leq S_n(^{208}\text{Pb}) \leq 0.156 \text{ fm}^{-3}$ and $0.132 \text{ fm}^{-3} \leq S_n(^{48}\text{Ca}) \leq 0.142 \text{ fm}^{-3}$. Averaging with respect to the cutoff, the final neutron skin predictions at N^3LO for ^{208}Pb and ^{48}Ca [83] can be expressed as:

$$S_n(^{208}\text{Pb}) = 0.144 \pm \Delta_{S_n} \quad \Delta_{S_n} = 0.009(0.011) , \quad (3.34)$$

$$S_n(^{48}\text{Ca}) = 0.140 \pm \Delta_{S_n} \quad \Delta_{S_n} = 0.006 . \quad (3.35)$$

For ^{208}Pb , the reference density was determined to be in the range $0.086 \text{ fm}^{-3} \leq \rho_1 \leq 0.108 \text{ fm}^{-3}$ over all orders and both cutoffs, while the symmetry energy coefficient was found to be in the range $19.1 \text{ MeV} \leq a_{\text{sym}} \leq 25.9 \text{ MeV}$.

In Tables 3.7 and 3.8 we observe the neutron skin predictions arising from the semi-microscopic

Table 3.7: The neutron skin (in fm) of ^{208}Pb obtained from the semi-microscopic model described in section 3.2.3.

Order	$\Lambda = 450 \text{ MeV}$	$\Lambda = 500 \text{ MeV}$
N ² LO	0.155 ± 0.005	0.147 ± 0.004
N ³ LO	0.150 ± 0.009	0.143 ± 0.004
N ⁴ LO	0.141 ± 0.004	0.139 ± 0.002

Table 3.8: As in Table 3.7, but for ^{48}Ca .

Order	$\Lambda = 450 \text{ MeV}$	$\Lambda = 500 \text{ MeV}$
N ² LO	0.150 ± 0.003	0.144 ± 0.002
N ³ LO	0.147 ± 0.005	0.142 ± 0.002
N ⁴ LO	0.141 ± 0.003	0.140 ± 0.001

nuclear EoS described in section 3.2.3. Overall, the neutron skins of ^{208}Pb and ^{48}Ca were found to be within 0.139-0.155 fm and 0.140-0.150 fm, respectively. The final estimates at N³LO, including truncation and cutoff uncertainty, are given below in units of fermi [84]:

$$S_n(^{208}\text{Pb}) = 0.147 \pm \Delta_{S_n} \quad \Delta_{S_n} = 0.009 , \quad (3.36)$$

$$S_n(^{48}\text{Ca}) = 0.145 \pm \Delta_{S_n} \quad \Delta_{S_n} = 0.005 . \quad (3.37)$$

Chapter 4

The Nuclear Equation of State and Neutron Stars

A neutron star is the remnant collapsed core of a giant star which has undergone a supernova explosion. Only stars with sufficient mass, about 8 solar masses ($8 M_{\odot}$) or greater, undergo a supernova event as the end of their life cycle [135]. Neutron stars are estimated to originate from stars having between 8 - 25 M_{\odot} [136] which corresponds to the mass range of supergiant main-sequence stars. Due to its extremely compact nature, the neutron star is directly supported against further gravitational collapse into a black hole by mechanisms of nuclear origin, which make these objects excellent natural laboratories for exploring the nuclear EoS at high densities. We begin by briefly discussing the historical relevance as well as some properties of neutron stars. We will then proceed to explore the predicted mass-radius relationship derived from the EoS through the TOV stellar structure equation.

4.1 General Aspects of Neutron Stars

In 1934, just a couple of years after the discovery of the neutron [137], Baade and Zwicky hypothesized the existence of a very dense stellar object, which they named neutron star, arising from the remnants of a supernova [138, 139]. In 1939 Tolman [140], and independently yet simultaneously, Oppenheimer and Volkoff [141] estimated the mass-radius relationship of these neutron stars based on general relativity and crude nuclear force models, thus producing the famous Tolman-Oppenheimer-Volkoff (TOV) equation. The TOV equation allows for the calculation of a theoretical upper limit on the possible mass of neutron stars. However, due to the lack of understanding of the nucleon interaction at the time, their original predictions were not accurate, placing the upper

limit of a neutron star mass lower than the Chandrasekhar limit.

Over the years, with a better understanding of nuclear interactions, a more realistic picture of neutron stars and their structure emerged. For a comprehensive look at historical developments of the neutron star EoS, see Refs. [142–154].

While the existence of neutron stars was a theoretical possibility, finding proof of their existence remained a challenge. Initial efforts involving attempts to compute and observe the thermal signature of neutron stars [155–158] were unsuccessful. In 1967, Pacini [159] postulated that fast rotating neutron stars could produce large electromagnetic emission generated from a powerful magnetic dipole. The next year, Bell and Hewish [160] discovered the first radio pulsar, characterized by an astonishingly stable periodic electromagnetic signal. Later that year, Gold theorized that neutron stellar objects were excellent candidates to explain the unusual characteristics of the pulsar signal [161].

By 1969, the connection between supernovas and pulsars was firmly established with the discoveries of the Vela [162] and Crab [163] nebula pulsars. Hundreds of pulsars were discovered in the 1970s and 80s using radio astronomy, while more recent developments have identified pulsars whose signals span the electromagnetic spectrum [134]. To date, more than two and a half thousand pulsars have been discovered [164], these stellar objects being found in many configurations including in binary pulsar systems [165], main-sequence binary-pulsar systems [166], globular clusters [167], with orbiting exo-planets [168] and displaying a wide variety of unusual, yet periodic signals [169, 170]. The recent GW170817 neutron star merger event, as detected through gravitational wave signatures by LIGO/Virgo [171], along with the accompanying gamma-ray burst [172], has generated further and remarkable evidence that observational data is aligned with theoretical predictions for neutron stars.

The incredibly small periods of pulsars indicates the extreme gravitational forces (and corresponding internal densities) needed to hold these rapidly rotating objects together. Classical estimates place the average density of pulsars to be around $3.6 \cdot 10^{17} \frac{\text{kg}}{\text{m}^3}$ (0.216 fm^{-3}) [134]. For reference, the average density found in atomic nuclei is on the order of $2.0 \cdot 10^{17} \frac{\text{kg}}{\text{m}^3}$ (0.12 fm^{-3}) and saturation density is about $2.67 \cdot 10^{17} \frac{\text{kg}}{\text{m}^3}$ (0.16 fm^{-3}). Thus the *average* densities found in pulsars is significantly greater than the density found at the center of atomic nuclei. Clearly, this points to the existence of very compact objects, whose composition is neutron rich and involves

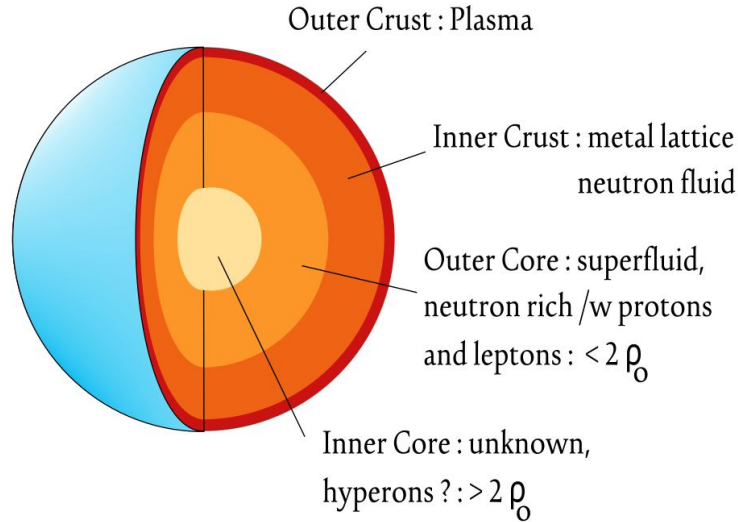


Figure 4.1: A illustration of neutron star structure as understood from current models [173, 174].

nuclear forces. For these reasons we refer to these objects as neutron stars. Figure 4.1 illustrates the internal structure of a neutron star as understood through current theoretical predictions.

4.1.1 Mass-Radius Relation

The mass-radius relationship of neutron stars is uniquely determined from the star's EoS and thus reliable observational constraints can shed light on the EoS. While the radius cannot be directly measured, the mass of neutron stars in binary systems can be inferred from observation together with application of gravitational theory. With constraints on the mass of a star, the Doppler shift then allows estimates of the radius [134].

The total mass range deduced from observed neutron stars is small compared to main-sequence stars and is around $1 M_{\odot}$. To date, the smallest mass neutron star has been determined to be $\approx 1.17 M_{\odot}$ [176], while the most massive observed neutron star is $\approx 2.14 M_{\odot}$ [177]. Of particular interest is the Chandrasekhar mass limit of white dwarf stars which is $1.4 M_{\odot}$. If this mass is exceeded, electron degeneracy would no longer be able to support a white dwarf star from gravitational collapse. Observational constrains on neutron star masses yield values clustered around $1.4 M_{\odot}$ [175] and for this reason this mass is referred to as the canonical-mass for neutron stars. This observation led to the idea that white dwarf collapse may be an additional mechanism for the formation of neutron stars [181–183].

As previously mentioned, the neutron star's radius is hard to measure directly, however, ob-

servational data allows for indirect inference. Observation-based constraints consistently place the estimated radius of a neutron star in the range of 10-15 km. For instance, using accreting and bursting sources, the radius of the canonical-mass neutron star was determined to be within a range of 10.4 to 12.9 km [178], while analysis from the LIGO/Virgo observations determined the radius to be in the range of 11.1 to 13.4 km [179]. Upper limits on the neutron star radii, as determined from iron emission lines, were placed between 14.5 and 16.5 km [180].

Neutron star models are generally in good agreement with observational constraints for the radius. For instance, the radius of the canonical-mass neutron star predicted from the set of EoS applied in Ref. [184] is predicted to be in the range 10.45 - 12.66 km. From a variety of techniques using experimentally determined quantities correlated to symmetry energy parameters the same quantity is determined to have a range of 10.7 to 13.1 km [184–187], while using a range of theoretical models a limit of 9.7 to 13.9 km is obtained [184, 188, 189]. On theoretical grounds, the largest mass was predicted to be $3.2 M_{\odot}$ [190], based on only three assumptions: 1) General Relativity is the appropriate theory for these massive stars, 2) the EoS is constrained by Le Chatelier’s principle ($\partial P/\partial \epsilon \geq 0$), and 3) the causality condition $\partial P/\partial \epsilon \leq c^2$. While such massive neutron star may be theoretically possible, no neutron star in this mass range has been observed.

It is interesting to note the small range of values for the radius across the mass range of neutron stars. Heavier neutron stars have larger central densities and thus the star becomes comparatively more compact, resulting in a very narrow mass-radius range in stark contrast to main-sequence stars whose masses and radii span several orders of magnitude.

4.2 EoS for β -Stable Nuclear Matter

In this section we will detail the construction of the EoS for stellar matter in β -equilibrium. We define the total energy per baryon as

$$e_T(\rho) = e_0(\rho) + e_{sym} (Y_n - Y_p)^2 + e_e + e_{\mu} + \sum_{i=n,p} Y_i \cdot m_i, \quad (4.1)$$

where the first two terms on the right-hand side are equivalent to Eq. (3.8). Here $Y_{n,p}$ is the neutron/proton fractions. The last term accounts for the baryon rest masses (in units of energy), while

$e_{e/\mu}$ are the energy-per-baryon of the electrons and muons, respectively. All terms are functions of density.

The energy density (ϵ_i), pressure (p_i) and density (ρ_i) for each particle species, i , at a given Fermi momentum, $(k_F)_i$, can be expressed as

$$\epsilon_i = \frac{\gamma}{2\pi^2} \cdot \int_0^{k_{F_i}} \sqrt{k^2 + m_i^2} k^2 dk , \quad (4.2)$$

$$p_i = \frac{1}{3} \frac{\gamma}{2\pi^2} \cdot \int_0^{k_{F_i}} \frac{k^2}{\sqrt{k^2 + m_i^2}} k^2 dk , \quad (4.3)$$

$$\rho_i = \frac{\gamma}{2\pi^2} \int_0^{k_{F_i}} k^2 dk . \quad (4.4)$$

The degeneracy, γ , is the number of spin states available to each particle species, equal to 2 for spin- $\frac{1}{2}$ fermions. Energy density is simply related to the energy per particle through the density:

$$\epsilon = \rho \cdot e(\rho) . \quad (4.5)$$

The Fermi energy for each species, i , given in Eq. (4.6) below, is referred to as the chemical potential:

$$\mu_i = \frac{\partial \epsilon_i}{\partial \rho_i} = \sqrt{k_{F_i}^2 + m_i^2} . \quad (4.6)$$

4.2.1 Particle Fractions

To evaluate Eq. (4.1) we must determine the fractions of each particle species:

$$Y_i = \frac{\rho_i}{\rho} . \quad (4.7)$$

Note, also, the following relation:

$$\mu_i = \frac{\partial \epsilon_i}{\partial \rho_i} = \frac{\partial \epsilon_i}{\partial Y_i} . \quad (4.8)$$

Next, we impose two additional constraints on the system, namely fixed baryon density, Eq. (4.9), and global charge neutrality, Eq. (4.10):

$$\rho_p + \rho_n = \rho \quad \Rightarrow \quad Y_p + Y_n = 1 , \quad (4.9)$$

$$\rho_p = \rho_e + \rho_\mu \quad \Rightarrow \quad Y_p = Y_e + Y_\mu . \quad (4.10)$$

To simultaneously solve these coupled equations, we define the functional F :

$$F = e_T + \lambda_1 \eta_1 + \lambda_2 \eta_2 , \quad (4.11)$$

where:

$$\eta_1 = 1 - Y_n + Y_p = 0 , \quad (4.12)$$

$$\eta_2 = Y_p - Y_e - Y_\mu = 0 , \quad (4.13)$$

and λ_i are Lagrange multipliers. We then minimize the functional with respect to the appropriate particle fractions,

$$\frac{\partial F}{\partial Y_i} = 0 . \quad (4.14)$$

We use Eqs. (4.1), (4.11) and (4.14) to relate the chemical potentials of each species. Taking the derivative of each species fraction with respect to F yields four equations:

$$\frac{\partial F}{\partial Y_p} = \frac{\partial e}{\partial Y_p} - \lambda_1 + \lambda_2 = 0 \quad \Rightarrow \quad \mu_p = \lambda_1 - \lambda_2 , \quad (4.15)$$

$$\frac{\partial F}{\partial Y_n} = \frac{\partial e}{\partial Y_n} - \lambda_1 = 0 \quad \Rightarrow \quad \mu_n = \lambda_1 , \quad (4.16)$$

$$\frac{\partial F}{\partial Y_e} = \frac{\partial e}{\partial Y_e} - \lambda_2 = 0 \quad \Rightarrow \quad \mu_e = \lambda_2 , \quad (4.17)$$

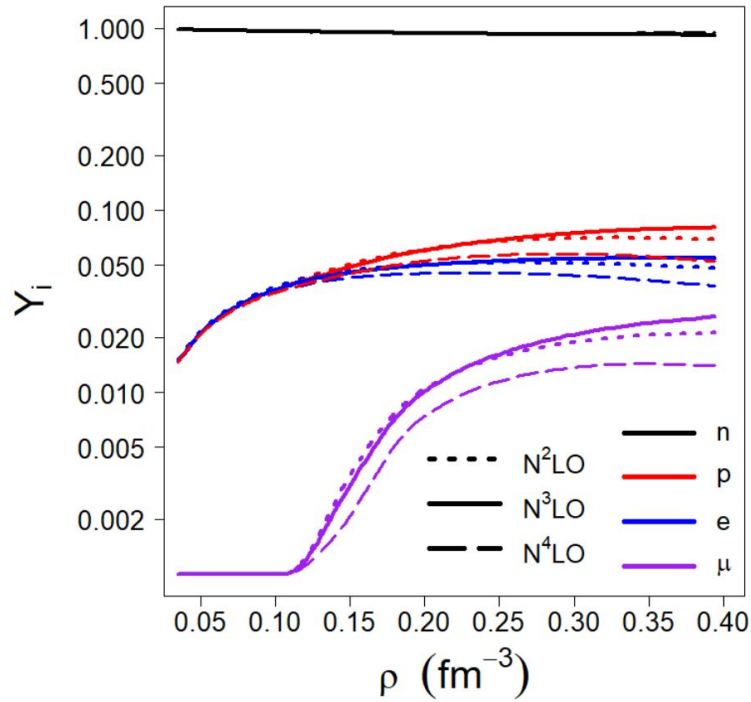


Figure 4.2: Fractions of neutrons (n), protons (p), electrons (e), and muons (μ) as a function of density at three orders of the chiral expansion. The cutoff Λ is 450 MeV.

$$\frac{\partial F}{\partial Y_\mu} = \frac{\partial e}{\partial Y_\mu} - \lambda_2 = 0 \quad \Rightarrow \quad \mu_\mu = \lambda_2 . \quad (4.18)$$

Combining the above equations, we obtain the following relationships:

$$\mu_\mu = \mu_e , \quad (4.19)$$

$$\mu_p = \mu_n - \mu_e . \quad (4.20)$$

4.2.2 Predictions in β -Stable Matter

Using Eqs. (4.2), (4.4), (4.5) and (4.6) along with the chemical potential relationships of Eqs. (4.19) and (4.20), we can derive the energy density and energy per particle in β -stable matter. For details of the derivation, see Appendix A.

The pressure of the system is related to density through:

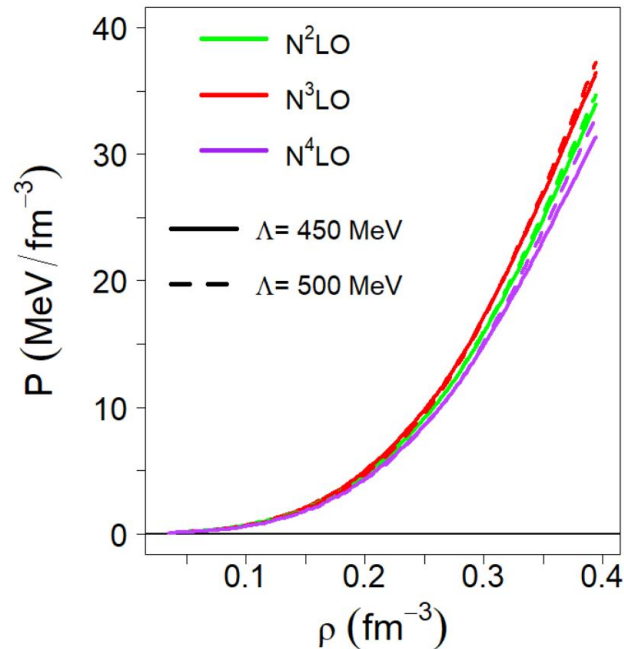


Figure 4.3: Pressure in β -stable nuclear matter at three orders of the chiral expansion and two values of the regulator.

$$P(\rho) = \rho^2 \frac{d(\frac{\epsilon_T}{\rho})}{d\rho} = \rho^2 \frac{de_T}{d\rho}, \quad (4.21)$$

which is the internal pressure critical for the star’s structure. We will briefly discuss the chiral EoS predictions for the pressure in β -stable nuclear matter at densities up to twice saturation density ($\approx 0.32 \text{ fm}^{-3}$). This choice is guided by considerations of the typical momentum of the system, Q , relative to the cutoff, $\Lambda \approx 450 \text{ MeV}$, to avoid issues with the chiral expansion in Q/Λ . Since the highest momentum of neutrons in neutron matter at twice saturation density is $\approx 420 \text{ MeV}$ and the r.m.s value is typically 60% of the maximum value, so-called “cutoff artifacts” should not pose serious problems [84].

For the nuclear EoS component of Eq. (4.1), we will use the semi-microscopic EoS detailed in section 3.2.3 for the reasons discussed therein.

In Fig. 4.2 we observe predictions for the particle fractions as a function of density using the techniques described in the previous section. We note the small fraction of particles other than neutrons, where even at high densities neutrons compose between 90% and 95% of all particles. The pressure predictions for the β -stable nuclear matter derived from the chiral NM EoS are shown

in Fig. 4.3. We note the lack of cutoff dependence and, at densities up to twice saturation density, the relatively small order dependence. At N³LO (and $\Lambda = 450$ MeV), the pressure at saturation density is determined to be, accounting for truncation error, $2.48 (\pm 0.289)$ MeV/fm³ while at twice saturation density a value of $20.54 (\pm 2.7)$ MeV/fm³ is obtained.

4.3 Radius of the Canonical-Mass Neutron Star

4.3.1 Polytropic extrapolation

In the previous section, we presented predictions for the EoS in β -stable matter. However, we must keep in mind that chiral predictions have a limited domain of validity, which, in the previous section, we estimated to be about twice saturation density. The densities within neutron stars can reach five to six times saturation density, and therefore an appropriate method for extrapolating the EoS to these densities must be employed. To accomplish this, we express the high density pressure through polytropes [192]:

$$P(\rho) = \alpha \rho^\Gamma, \quad (4.22)$$

fitted piece-wise at selected densities [192].

In this way, by varying the adiabatic index, Γ , a wide range of pressures can be explored. We chose a density of $2\rho_0$ as the first matching density as this is where our chiral predictions end. We vary the adiabatic index from 1.5 to 4.5, following guidelines from the literature [192]. We then match the pressure with an additional set of polytropes at $3\rho_0$, with adiabatic indices spanning the same range as the first set. In this manner we can explore a wide variety of “soft” and “stiff” EoS and obtain a realistic estimate of the uncertainty on the radius arising from the “spreading” of the pressure at the higher densities. It is worth stressing that high-density EoS extrapolations are not meant to be a replacement for microscopic theoretical predictions [84, 193] which, at this time, are not feasible at super-high densities.

We choose α so as to ensure continuity at the matching density:

$$\alpha \equiv \frac{P_{(\rho_m)}}{(\rho_m)^\Gamma}. \quad (4.23)$$

To evaluate the energy density, we use Eq. (4.22) in Eq. (4.21). Integrating to obtain the total energy density yields

$$\epsilon_T = \frac{\alpha}{\Gamma - 1} \rho^\Gamma + C\rho, \quad (4.24)$$

which ensures that the energy density is likewise continuous at the matching density. The constant C is then:

$$C = \frac{\epsilon(\rho_m)}{\rho_m} - \frac{\alpha}{\Gamma - 1} \rho_m^{\Gamma-1}. \quad (4.25)$$

To construct the EoS for high densities, we must apply additional physical constraints. One is the *causality limit*, which imposes the speed of light as the maximum speed of sound in matter. In terms of $P(\epsilon)$, the causality condition reads

$$\frac{dP(\rho)}{d\epsilon(\rho)} < 1. \quad (4.26)$$

Note that the constraint on the speed of sound is strictly valid only in absence of dispersion or absorption in stellar matter [191, 194]. Nevertheless, imposing the causality constraint is standard practice when constructing neutron star EoS and we will apply it in this work [134, 190, 192, 194].

Additionally we will only consider polytropes which can support a maximum mass of at least $1.97 M_\odot$, to be consistent with the lower limit of the $2.01 \pm 0.04 M_\odot$ observation reported in Ref. [195]. This limit is lower than the most massive observed neutron star to date. However, small variations in the maximum mass constraint will not be very impactful on our predictions, which focus on the radius of the canonical-mass neutron star.

In Fig. 4.4 we display the spreading of pressure values arising from the polytrope extrapolation to high densities. The adiabatic index is incremented in intervals of 0.5, creating a total of seven curves. The left most point of the figure is the first density ($2\rho_0$) at which polytropes are matched to the semi-microscopic β -stable EoS. The orange line marks the second point ($3\rho_0$) at which a new set of polytropes, having the same range of adiabatic indices, is matched to each of the previous pressure curves. (We use c.g.s. units to facilitate comparisons, as this unit system is popular in the astrophysical community.)

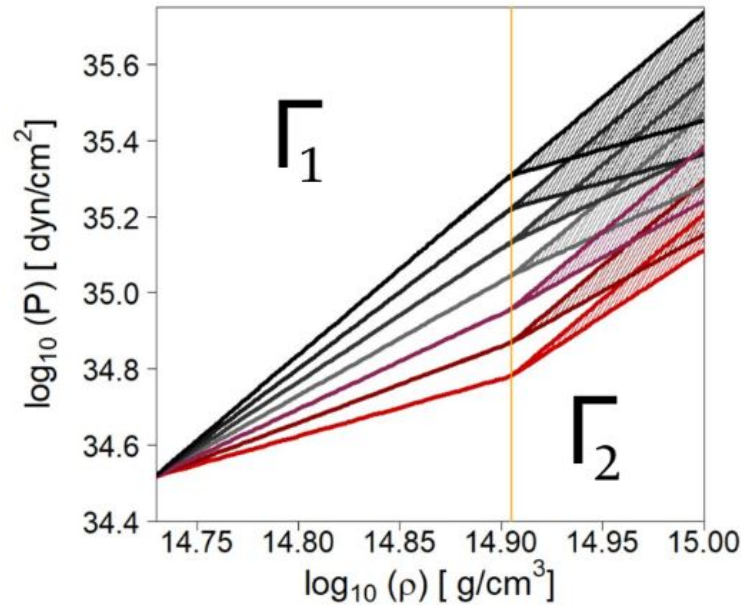


Figure 4.4: Pressure spread resulting from the polytropic extrapolation of the β -stable EoS as described in the text. The interaction at N³LO with $\Lambda = 450$ MeV is used.

4.3.2 The TOV Equation

With the EoS available over a full range of densities, we now discuss how the mass-radius relation of a neutron star is evaluated. In this section we will briefly review the TOV equation [140, 141] and how the mass-radius relationship emerges from the equation and a given input EoS.

The TOV equation describes a spherically symmetric inertial massive object composed of a perfect fluid in hydrostatic equilibrium. The equation relates the pressure within the star to the mass-energy density as functions of the radial distance from the star's center:

$$\frac{dP(r)}{dr} = -\frac{G}{c^2} \frac{(P(r) + \epsilon(r)) (M(r) + 4\pi r^3 \frac{P(r)}{c^2})}{r(r - \frac{2GM(r)}{c^2})}. \quad (4.27)$$

A spherical shell of material is related to the energy density at a distance r from the star's center by:

$$\frac{dM(r)}{dr} = \frac{4\pi}{c^2} r^2 \epsilon(r). \quad (4.28)$$

The star has a gravitational mass (M) is determined from the radius (R) and the mass-energy

density ($\epsilon(r)$):

$$M(R) = \int_0^R \frac{\epsilon(r)}{c^2} d^3r . \quad (4.29)$$

Since the pressure and energy-density are functions of density, for a fixed central density the mass-radius of the star can be determined by Eqs. (4.28) and (4.27). Equation (4.27) can be integrated numerically by summing over shells of fixed width at incremented distance from the star's center so as to evaluate the total pressure as a function of radial distance. Equation (4.28) can be integrated in the same fashion, simultaneously, to determine the mass contained within each spherical shell. To accomplish this we employed fourth-order Runge-Kutta method. The Runge-Kutta method can be summarized as follows:

- 1) For a 1st order ordinary differential equation in the form : $\frac{dy}{dx} = f(x, y)$,
- 2) and a given initial point (x_o, y_o) and fixed incremental step h ,
- 3) the set of y_i points at corresponding $(x_i \equiv x_{i-1} + h)$ points is given by the following algorithm:

$$y_{n+1} = y_n + h T(x_n, y_n, h) , \quad (4.30)$$

where $T(x_n, y_n, h)$ is defined as:

$$T(x_n, y_n, h) = \frac{1}{6}(k_1 + 2k_2 + 2k_3 + k_4) , \quad (4.31)$$

and the k_i 's are as follows:

$$k_1 = f(x_n, y_n) , \quad (4.32)$$

$$k_2 = f\left(x_n + \frac{h}{2}, y_n + \frac{h}{2}k_1\right) , \quad (4.33)$$

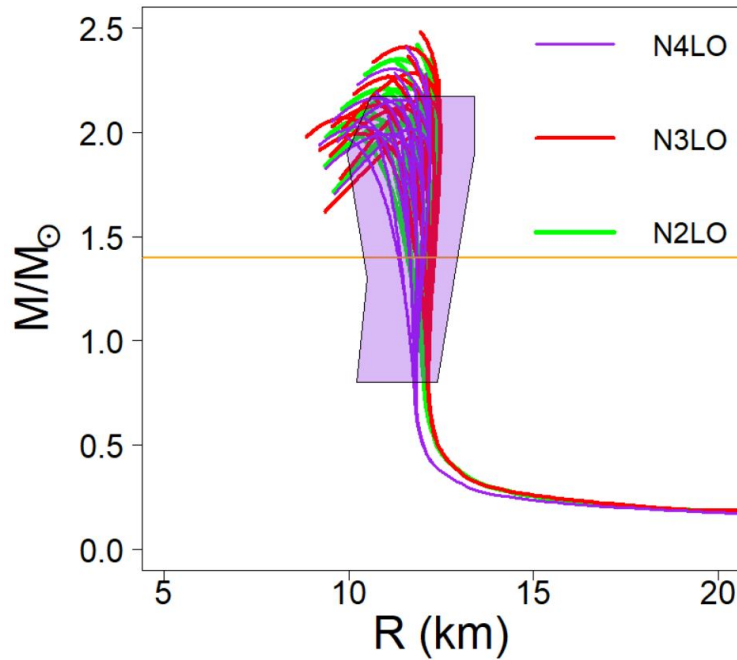


Figure 4.5: Mass vs. radius relation derived from the NM EoS at three orders of the chiral expansion with $\Lambda = 450$ MeV. The orange line marks a mass of $1.4 M_{\odot}$. The shaded overlay represents the constraints obtained from Ref. [178].

$$k_3 = f\left(x_n + \frac{h}{2}, y_n + \frac{h}{2}k_2\right), \quad (4.34)$$

$$k_4 = f(x_n + h, y_n + hk_3). \quad (4.35)$$

Clearly, the initial condition of a given central density will correspond to a given pressure and energy density at zero radial distance from the star's center, which is a singularity. To avoid it, we begin at a radial distance offset enough to prevent numerical divergences, but not enough to cause any notable numerical error. Since the integration involves computing the pressure at each spherical shell for a given incremented distance from the star's center, the radial distance at which the pressure effectively vanishes corresponds to the star's radius. Then, Eq. (4.29), provides the total mass enclosed within such radius.

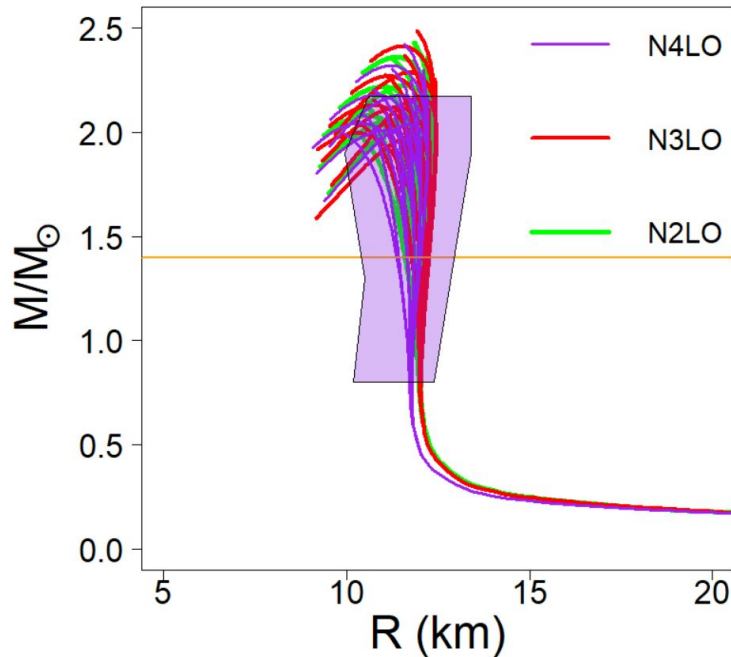


Figure 4.6: Same legend as in Fig. 4.5, except for the cutoff, which is equal to 500 MeV.

4.3.3 Predictions for the Neutron Star Radius

To briefly reiterate, we construct an EoS using the chiral NM EoS in β equilibrium at densities ranging from $0.03 \text{ fm}^{-3} \leq \rho \leq 2\rho_0$. At higher densities, we match a polytropic extrapolation to the chiral predictions. To account for a continuous EoS at crustal densities we utilize the crustal EoS from Refs. [196, 197]. The neutron star crust is composed of metals in crystalline structure and cannot be described as a homogeneous fluid of neutrons, as appropriate for the BHF theory. Instead, an appropriate crustal EoS [197] is matched to our previously described EoS using Akima interpolation.

In Fig. 4.5 we see the predictions of the mass-radius relationship derived from the chiral NM EoS at three chiral orders and cutoff $\Lambda = 450$ MeV. The orange line highlights the predictions for a $1.4 M_\odot$ neutron star. The polygonal lavender overlay represents the constraints from Ref. [178]. We note that for the canonical mass, there is almost no spreading as a result of the variations in the polytropic extrapolation at $3\rho_0$ and above, while for the extrapolation between $2\rho_0$ and $3\rho_0$ there is a small yet noticeable impact which creates an uncertainty on the order of ± 0.5 km. This is interesting since the predicted central densities corresponding to these canonical mass stars are

Table 4.1: Adiabatic indices, Γ_1 and Γ_2 , corresponding to the two matching densities, see Fig. 4.4. R is the radius, ρ_c is the central density, and v_s is the speed of sound in units of the speed of light.

Γ_1	Γ_2	R (km)	ρ_c (fm^{-3})	v_s (c)
1.5	3.5 - 4.5	11.19 - 11.34	0.653 - 0.589	0.718 - 0.813
2.0	3.0 - 4.5	11.49 - 11.62	0.620 - 0.548	0.642 - 0.786
2.5	3.0 - 4.5	11.83 - 11.86	0.543 - 0.514	0.621 - 0.789
3.0	2.5 - 4.5	12.05 - 12.06	0.488 - 0.478	0.555 - 0.766
3.5	1.5 - 4.5	12.19 - 12.18	0.445 - 0.444	0.650 - 0.676
4.0	1.5 - 4.5	12.27	0.420	0.759 - 0.699
4.5	1.5 - 4.5	12.32	0.403	0.792 - 0.750

1.25-2 times greater than $2\rho_0$, which is the region of large pressure variations seen in Fig. 4.4. Thus, we confirm that the radii are sensitive mostly to pressures much lower than those found at the star’s center (central density ranges shown in Table 4.1).

Table 4.1 displays intervals of central densities, radii, and speed of sound corresponding to the given ranges of the polytropic index. The missing entries in Γ_2 are due to restrictions imposed on the EoS as discussed previously. We note that for the “stiff” EoS extrapolations at $2\rho_0$, denoted by the upper range of Γ_1 , there is no variation at all in radius predictions due to pressure variations at and above $3\rho_0$.

The total range for the radius of the canonical mass neutron star for N^3LO , $\Lambda = 450$ MeV, can be expressed as 11.19 - 12.32 km. Accounting for both truncation and extrapolation uncertainty, we estimate:

$$R_{1.4M_\odot} = 11.8 (\pm 1) \text{ km} \quad (4.36)$$

We note that our predictions fall within the range of radius constraints mentioned at the beginning of this chapter, namely 10.4 to 12.9 km [178], the LIGO/Virgo observations of 11.1 to 13.4 km [179], as well as the overlay in Fig. 4.5 which is based on observational data [178]. Appendix B contains extensive tabulations of the results for the canonical-mass predictions at three chiral orders (N^2LO , N^3LO , N^4LO) and varying the cutoff. Also contained therein are the β -stable EoS predictions as determined from the chiral NM EoS.

Chapter 5

Subleading contributions to the chiral three-nucleon force

The complete 3NF beyond $N^2\text{LO}$ is very complex and was neglected in nuclear structure studies of the past. However, in recent years, the 3NF at $N^3\text{LO}$ has been derived [198, 200] and applied in some nuclear many-body systems [75, 76, 78, 79]. The contributions to the subleading chiral 3NF include: the 2PE topology, which is the longest-range component of the subleading 3NF, the two-pion-one-pion exchange (2P-1P) topology, and the ring topology, generated by a circulating pion which is absorbed and reemitted from each of the three nucleons.

Direct inclusion of the subleading chiral 3NF is a challenge for many-body calculations. However, similar to the leading 3NF, the contributions of the 3NF at $N^3\text{LO}$ can be conveniently expressed in the form of density-dependent effective two-nucleon interactions, as derived in Refs. [72, 77]. Here, we retain all the long-range components [77].

The in-medium NN potentials corresponding to the short-range subleading 3NFs have been calculated in Ref. [72], and include the two-pion-exchange-contact topology and the relativistic corrections, proportional to $1/M$, where M is the nucleon mass. Both have been shown to be negligible [78, 79] and are therefore left out of this study.

5.1 Expressions for the long-range subleading chiral three-nucleon forces

In this section, we show the long-range subleading contributions to the 3NFs at $N^3\text{LO}$. Contributions to the 3NF at $N^3\text{LO}$ take the form of three topologies: the 2PE, the 2P-1P, and the ring topology. Below, we provide the analytical expressions for the most important in-medium

density-dependent potentials derived from the 3N diagrams at N³LO. For a detailed derivation, see Ref. [77].

We begin with the 2PE topology. An important contribution to the double exchange is:

$$\begin{aligned}
V_{NN}^{med,3} = & \frac{g_A^4}{512 \pi^3 f_\pi^6} \left[\right. \\
& [m_\pi + (2m_\pi^2 + q^2)A(q)] [8k_f^3 + 6q^2(\Gamma_0 - \Gamma_1)] - 6m_\pi^2 \Gamma_0 [3m_\pi + (2m_\pi^2 + q^2)A(q)] \\
& + 3(2m_\pi^2 + q^2) [m_\pi^3 - 2m_\pi q^2 - (2m_\pi^4 + 5m_\pi^2 q^2 + 2q^4)A(q)] G_0 \\
& + 3i(\vec{\sigma}_1 + \vec{\sigma}_2) \cdot (\vec{q} \times \vec{p}) \left(2[m_\pi + (2m_\pi^2 + q^2)A(q)] (\Gamma_0 + \Gamma_1) \right. \\
& \quad \left. + [2m_\pi q^2 - m_\pi^3 + (2m_\pi^4 + 5m_\pi^2 q^2 + 2q^4)A(q)] [G_0 + 2G_1] \right) \\
& + \vec{\tau} \cdot \vec{\tau} [m_\pi + (4m_\pi^2 + q^2)A(q)] \\
& \quad \left(i(\vec{\sigma}_1 + \vec{\sigma}_2) \cdot (\vec{q} \times \vec{p}) [2\Gamma_0 + 2\Gamma_1 - (2m_\pi^2 + q^2)(G_0 + 2G_1)] \right. \\
& \quad + 4(\vec{\sigma}_1 \cdot \vec{q} \vec{\sigma}_2 \cdot \vec{q} - \vec{\sigma}_1 \cdot \vec{\sigma}_2 q^2) G_2 \\
& \quad \left. \left. - 4(\vec{\sigma}_1 \cdot (\vec{q} \times \vec{p}) \vec{\sigma}_2 \cdot (\vec{q} \times \vec{p})) [G_0 + 4G_1 + 4G_3] \right) \right] . \tag{5.1}
\end{aligned}$$

The expressions for the G_ν functions, $A(q)$, as well as for the Γ_i functions can be found in Chapter 2. The 2P-1P exchange topology yields four contributions. The vertex correction by 1P exchange yields the following contribution:

$$\begin{aligned}
V_{NN}^{med,3} = & \frac{g_A^4}{512 \pi^3 f_\pi^6} \left[\right. \\
& [2m_\pi^2 \Gamma_0 - \frac{4k_f^3}{3}] [\vec{\tau} \cdot \vec{\tau} f_3(q) + 3f_7(q)] - \vec{\tau} \cdot \vec{\tau} [2\Gamma_2 + \frac{q^2}{2} \tilde{\Gamma}_3] q^2 f_1(q) \\
& + \tilde{\Gamma}_1 q^2 [3f_6(q) + \vec{\tau} \cdot \vec{\tau} f_2(q)] - 2 \vec{\sigma}_1 \cdot \vec{\sigma}_2 [3\Gamma_2 f_5(q) + \vec{\tau} \cdot \vec{\tau} \tilde{\Gamma}_1 q^2 f_8(q)] \\
& - 3(\vec{\sigma}_1 \cdot \vec{p} \vec{\sigma}_2 \cdot \vec{p} + \vec{\sigma}_1 \cdot \vec{p}' \vec{\sigma}_2 \cdot \vec{p}') \tilde{\Gamma}_3 f_5(q) \\
& + 2\vec{\sigma}_1 \cdot \vec{q} \vec{\sigma}_2 \cdot \vec{q} \left(\vec{\tau} \cdot \vec{\tau} \tilde{\Gamma}_1 f_8(q) - 3[\Gamma_2 + \frac{q^2}{4} \tilde{\Gamma}_3] f_4(q) \right) \\
& \left. + i(\vec{\sigma}_1 + \vec{\sigma}_2) \cdot (\vec{q} \times \vec{p}) \left(\vec{\tau} \cdot \vec{\tau} [\tilde{\Gamma}_1 (2f_8(q) - f_2(q)) + \tilde{\Gamma}_3 \frac{q^2}{2} f_1(q)] - 3\tilde{\Gamma}_1 f_6(q) \right) \right] , \tag{5.2}
\end{aligned}$$

where the reduced functions, $f_i(s)$, have the following analytic expressions:

$$f_1(s) = \frac{m_\pi}{s^2} (1 - 2g_A^2) - \frac{g_A^2 m_\pi}{4m_\pi^2 + s^2} + \left(1 + g_A^2 + \frac{4m_\pi^2}{s^2} (2g_A^2 - 1)\right) A(s), \quad (5.3)$$

$$f_2(s) = 2m_\pi + (4m_\pi^2 + 2s^2)A(s), \quad (5.4)$$

$$f_3(s) = m_\pi(1 - 3g_A^2) + (4m_\pi^2(1 - 2g_A^2) + s^2(1 - 3g_A^3))A(s), \quad (5.5)$$

$$f_4(s) = -2 g_A^2 A(s), \quad (5.6)$$

$$f_5(s) = 2 g_A^2 s^2 A(s), \quad (5.7)$$

$$f_6(s) = 4m_\pi + (8m_\pi^2 + 4s^2)A(s), \quad (5.8)$$

$$f_7(s) = 2m_\pi + (4m_\pi^2 + 2s^2)A(s), \quad (5.9)$$

$$f_8(s) = -\frac{1}{2} (m_\pi + (4m_\pi^2 + 2s^2)A(s)). \quad (5.10)$$

The three nucleon-ring (3NR) interaction produces a particularly impactful set of contributions.

Two originate from the self-closings of nucleon lines:

$$V_{NN}^{med,0} = -\frac{g_A^4 k_f^3}{96\pi^3 f_\pi^6} \vec{\tau} \cdot \vec{\tau} \left(\frac{m_\pi(9m_\pi^2 + 2q^2)}{4m_\pi^2 + q^2} + \frac{3m_\pi^2 + q^2}{q} \arctan\left(\frac{q}{2m_\pi}\right) \right), \quad (5.11)$$

$$V_{NN}^{med,0} = \frac{g_A^6 k_f^3}{96\pi^3 f_\pi^6} \left[\vec{\tau} \cdot \vec{\tau} \left(\frac{23m_\pi^3(2m_\pi^2 + q^2) + 3m_\pi q^4}{(4m_\pi^2 + q^2)^2} + \frac{3m_\pi^2 + q^2}{q} \arctan\left(\frac{q}{2m_\pi}\right) \right) \right. \\ \left. + \frac{3}{2q^2} (\vec{\sigma}_1 \cdot \vec{q} \vec{\sigma}_2 \cdot \vec{q} - \vec{\sigma}_1 \cdot \vec{\sigma}_2 q^2) \left(\frac{m_\pi^3}{4m_\pi^2 + q^2} + \frac{q^2 - m_\pi^2}{2q} \arctan\left(\frac{q}{2m_\pi}\right) \right) \right]. \quad (5.12)$$

The concatenation of nucleon lines for the 3NR interaction can be regrouped according to the

power of the scaled coupling constant. There are five contributions arising from the $\propto g^4$ component of the 3NR interaction, all of which are expressible as an integration. The first contains only an isoscalar central term:

$$V_{NN}^{med,CC} = \frac{3 g_A^4}{256 \pi^4 f_\pi^6} \int_0^\infty dl \left[l \tilde{\Gamma}_1(l) \left([m_\pi^2 (8p^2 - q^2) + (4p^2 + q^2)(p^2 - l^2)] \frac{\Lambda(l)}{p^2} + \frac{l}{p^2} (q^2 - 4p^2) + 2(2m_\pi^2 + q^2)(l^2 - p^2 - m_\pi^2) \Omega(l) \right) + \frac{16k_f^3}{3} \right]. \quad (5.13)$$

The second term contain isoscalar and isovector spin-spin and tensor terms:

$$V_{NN}^{med,CC} = \frac{g_A^4 (3 + \vec{\tau} \cdot \vec{\tau})}{64 \pi^4 f_\pi^6} (\vec{\sigma}_1 \cdot \vec{\sigma}_2 q^2 - \vec{\sigma}_1 \cdot \vec{q} \vec{\sigma}_2 \cdot \vec{q}) \int_0^\infty dl \frac{l \tilde{\Gamma}_1(l)}{4p^2 - q^2} \left((B + q^2 l^2) \Omega(l) - (m_\pi^2 + l^2 + p^2) \Lambda(l) \right). \quad (5.14)$$

The third term contains an isoscalar and isovector quadratic spin-orbit term:

$$V_{NN}^{med,CC} = \frac{g_A^4 (3 + \vec{\tau} \cdot \vec{\tau})}{64 \pi^4 f_\pi^6} (\vec{\sigma}_1 \cdot (\vec{q} \times \vec{p}) \vec{\sigma}_2 \cdot (\vec{q} \times \vec{p})) \int_0^\infty dl \frac{l \tilde{\Gamma}_1(l)}{4p^2 - q^2} \left[-\frac{l}{p^2} + \left(\frac{m_\pi^2 + l^2 + p^2}{p^2} + \frac{2(4m_\pi^2 + 4l^2 + q^2)}{4p^2 - q^2} \right) \Lambda(l) + 2(m_\pi^2 + 3l^2 + p^2 - \frac{4(m_\pi^2 + l^2 + p^2)^2}{4p^2 - q^2}) \Omega(l) \right]. \quad (5.15)$$

The fourth term is a isovector central term:

$$V_{NN}^{med,CC} = \frac{g_A^4 \vec{\tau} \cdot \vec{\tau}}{64 \pi^4 f_\pi^6} \int_0^\infty dl \left[(3 l \Gamma_2(l) + l^3 \tilde{\Gamma}_3(l)) ((2m_\pi^2 + q^2) \Omega(l) - 2 \Lambda(l)) + l \tilde{\Gamma}_1(l) \left(\frac{l}{4p^2} (q^2 - 4p^2) + (2m_\pi^2 + p^2 - l^2 + \frac{q^2}{4} - \frac{q^2}{4p^2} (m_\pi^2 + l^2)) \Lambda(l) + (m_\pi^2 + \frac{q^2}{2}) (l^2 - p^2 - m_\pi^2) \Omega(l) \right) + \frac{8k_f^3}{3} \right]. \quad (5.16)$$

The fifth and final component of the $\propto g_A^4$ component to the 3N-ring interaction is an isovector spin-orbit term:

$$\begin{aligned}
V_{NN}^{med,CC} &= \frac{g_A^4 \vec{\tau} \cdot \vec{\tau}}{64 \pi^4 f_\pi^6} i(\vec{\sigma}_1 + \vec{\sigma}_2) \cdot (\vec{q} \times \vec{p}) \\
&\int_0^\infty dl \frac{l}{4p^2 - q^2} \left[\tilde{\Gamma}_1(l) [(p^2 + l^2)\Lambda(l) - (m_\pi^2(p^2 + l^2) + q^2 l^2 + (p^2 - l^2)^2)\Omega(l)] \right. \\
&\quad + 4\Gamma_2(l) \left((m_\pi^2 + l^2 - p^2 + \frac{q^2}{2})\Omega(l) - \Lambda(l) \right) \\
&\quad + \frac{\tilde{\Gamma}_3(l)}{2} \left([(m_\pi^2 + p^2)^2 + 3l^4 + 2l^2(2m_\pi^2 - 2p^2 + q^2)]\Omega(l) \right. \\
&\quad \left. \left. - (m_\pi^2 + 3l^2 + p^2)\Lambda(l) \right) \right]. \tag{5.17}
\end{aligned}$$

In addition to the $\propto g_A^4$ components of the 3NR interaction there are nine additional $\propto g_A^6$ components. These can be grouped into a set of five contributions, the first of which is an isoscalar central term:

$$\begin{aligned}
V_{NN}^{med,2} &= \frac{3g_A^6}{256 \pi^4 f_\pi^6} \int_0^\infty dl \left[\right. \\
&4l\gamma_2(l) \left(\frac{l}{p^2}(4p^2 - q^2) + [(m_\pi^2 + l^2)\frac{q^2}{p^2} - 8m_\pi^2 - 3q^2]\Lambda(l) + (2m_\pi^2 + q^2)^2\Omega(l) \right) \\
&+ \frac{l}{2}\tilde{\gamma}_3(l) \left(\frac{l}{p^2}[2p^2(7l^2 - 2m_\pi^2 - p^2) + q^2(m_\pi^2 - 3l^2)] \right. \\
&\quad + [2p^4 + p^2(8m_\pi^2 - 4l^2 + q^2) + 6m_\pi^2(m_\pi^2 - 4l^2) + 2l^2(l^2 - 4q^2) \\
&\quad \left. + \frac{q^2}{p^2}(3l^4 + 2m_\pi^2 l^2 - m_\pi^4)]\Lambda(l) \right. \\
&\quad \left. + (2m_\pi^2 + q^2)[2l^2(3m_\pi^2 + p^2 + q^2) - l^4 - (m_\pi^2 + p^2)^2]\Omega(l) \right) - \frac{16k_f^3}{3} \left. \right]. \tag{5.18}
\end{aligned}$$

The second component is an isoscalar spin-orbit term:

$$\begin{aligned}
V_{NN}^{med,2} = & \frac{3g_A^6}{256 \pi^4 f_\pi^6} i(\vec{\sigma}_1 + \vec{\sigma}_2) \cdot (\vec{q} \times \vec{p}) \int_0^\infty dl \frac{l}{4p^2 - q^2} \left[\right. \\
& \gamma_2(l) \left([4(p^2 - l^2 - 2m_\pi^2) - 3q^2 + \frac{q^2}{p^2}(m_\pi^2 + l^2)] \Lambda(l) \right. \\
& \quad \left. + \frac{l}{p^2}(4p^2 - q^2) + (2m_\pi^2 + q^2)(2m_\pi^2 + 2l^2 - 2p^2 + q^2) \Omega(l) \right) \\
& + \tilde{\gamma}_3(l) \left(\frac{l}{4p^2}(4p^2 - q^2)(m_\pi^2 + l^2 + p^2) \right. \\
& \quad + [p^2(2l^2 - 4m_\pi^2 - \frac{3q^2}{4} - p^2) + \frac{q^2}{4p^2}(m_\pi^2 + l^2)^2 - l^4 \\
& \quad - l^2(4m_\pi^2 + \frac{3q^2}{2}) - m_\pi^2(3m_\pi^2 + \frac{q^2}{2})] \Lambda(l) \\
& \quad \left. \left. + (2m_\pi^2 + q^2)[l^4 + l^2(2m_\pi^2 - 2p^2 + q^2) + (m_\pi^2 + p^2)^2] \Omega(l) \right) \right]. \tag{5.19}
\end{aligned}$$

The third component is an isovector spin-orbit term:

$$\begin{aligned}
V_{NN}^{med,2} = & \frac{g_A^6 \vec{\tau} \cdot \vec{\tau}}{128 \pi^4 f_\pi^6} i(\vec{\sigma}_1 + \vec{\sigma}_2) \cdot (\vec{q} \times \vec{p}) \int_0^\infty dl \frac{l}{4p^2 - q^2} \left[\right. \\
& \gamma_2(l) \left([4(2m_\pi^2 + l^2 - p^2) + 3q^2 - \frac{q^2}{p^2}(m_\pi^2 + l^2)] \Lambda(l) \right. \\
& \quad \left. + \frac{l}{p^2}(q^2 - 4p^2) + (2m_\pi^2 + q^2)(2p^2 - 2m_\pi^2 - 2l^2 - q^2) \Omega(l) \right) \\
& + \tilde{\gamma}_3(l) \left(\frac{l}{2p^2}(4p^2 - q^2)(m_\pi^2 - l^2) \right. \\
& \quad + (m_\pi^2 - l^2 + p^2) [p^2 - l^2 - 3m_\pi^2 - \frac{q^2}{2} + \frac{q^2}{2p^2}(m_\pi^2 + l^2)] \Lambda(l) \\
& \quad \left. \left. + (m_\pi^2 + p^2 - l^2)^2 (m_\pi^2 + l^2 - p^2 + \frac{q^2}{2}) \Omega(l) \right) \right]. \tag{5.20}
\end{aligned}$$

The fourth component contains an isovector spin-spin tensor and tensor term:

$$\begin{aligned}
V_{NN}^{med,2} = & \frac{g_A^6}{64 \pi^4 f_\pi^6} (\vec{\sigma}_1 \cdot \vec{\sigma}_2 q^2 - \vec{\sigma}_1 \cdot \vec{q} \vec{\sigma}_2 \cdot \vec{q}) \int_0^\infty dl \frac{l}{4p^2 - q^2} \left[\right. \\
& 4\gamma_2(l) \left((m_\pi^2 + l^2 + p^2) \Lambda(l) - (B + q^2 l^2) \Omega(l) \right) \\
& + \tilde{\gamma}_3(l) \left(\frac{l}{8p^2} (4p^2 - q^2) (m_\pi^2 + l^2 + p^2) \right. \\
& \quad \left. + [p^2(l^2 - 3m_\pi^2 + \frac{q^2}{8} - \frac{3p^2}{2})] + \frac{l^4}{2} - m_\pi^2 l^2 - \frac{3m_\pi^4}{2} \right. \\
& \quad \left. + \frac{q^2}{4} (m_\pi^2 - l^2) + \frac{q^2}{8p^2} (m_\pi^2 + l^2)^2 \right] \Lambda(l) \\
& \left. + (m_\pi^2 - l^2 + p^2) (B + q^2 l^2) \Omega(l) \right]. \tag{5.21}
\end{aligned}$$

The fifth contribution is an isovector quadratic spin-orbit term:

$$\begin{aligned}
V_{NN}^{med,2} = & \frac{g_A^6}{64 \pi^4 f_\pi^6} (\vec{\sigma}_1 \cdot (\vec{q} \times \vec{p}) \vec{\sigma}_2 \cdot (\vec{q} \times \vec{p})) \int_0^\infty dl \frac{l}{4p^2 - q^2} \left[\right. \\
& 4\gamma_2(l) \left(\frac{l}{p^2} + [1 - \frac{m_\pi^2 + l^2}{p^2} - \frac{2(4m_\pi^2 + 4l^2 + 1^2)}{4p^2 - q^2}] \Lambda(l) \right. \\
& \quad \left. + [\frac{8(m_\pi^2 + l^2 + p^2)^2}{4p^2 - q^2} - 8l^2 - 4m_\pi^2 - q^2] \Omega(l) \right) \\
& + \tilde{\gamma}_3(l) \left(\frac{l}{p^2} (l^2 - m_\pi^2 - p^2) + \right. \\
& \quad \left. + [\frac{m_\pi^4 - l^4}{p^2} + 2l^2 - p^2 + \frac{8}{4p^2 - q^2} ((m_\pi^2 + p^2)^2 - l^4)] \Lambda(l) \right. \\
& \quad \left. + 2(l^2 - m_\pi^2 - p^2) [\frac{4(m_\pi^2 + l^2 + p^2)^2}{4p^2 - q^2} - 3l^2 - m_\pi^2 - p^2] \Omega(l) \right) \left. \right]. \tag{5.22}
\end{aligned}$$

Four additional contributions arise from the concatenations. The first is an isoscalar spin-spin and tensor term:

$$\begin{aligned}
V_{NN}^{med,cc} = & \frac{3g_A^6}{256 \pi^4 f_\pi^6} (\vec{\sigma}_1 \cdot \vec{\sigma}_2 q^2 - \vec{\sigma}_1 \cdot \vec{q} \vec{\sigma}_2 \cdot \vec{q}) \int_0^\infty dl \frac{l}{4p^2 - q^2} \left[\right. \\
& 12\Gamma_2(l) \left((m_\pi^2 + l^2 + p^2)\Omega(l) - \Lambda(l) \right) \\
& + \tilde{\Gamma}_3(l) \left(\frac{l}{2p^2} (q^2 - 4p^2) \right. \\
& \quad + [3(3m_\pi^2 + l^2 + 3p^2) - \frac{q^2}{2} - \frac{q^2}{2p^2} (m_\pi^2 + l^2)] \Lambda(l) \\
& \quad \left. \left. - [4l^2(2m_\pi^2 + q^2 - 2p^2) + l^4 + 7(m_\pi^2 + p^2)^2] \Omega(l) \right) \right]. \tag{5.23}
\end{aligned}$$

The isoscalar quadratic spin-orbit term reads:

$$\begin{aligned}
V_{NN}^{med,2} = & \frac{3g_A^6}{64 \pi^4 f_\pi^6} (\vec{\sigma}_1 \cdot (\vec{q} \times \vec{p}) \vec{\sigma}_2 \cdot (\vec{q} \times \vec{p})) \int_0^\infty dl \frac{1}{4p^2 - q^2} \left[\right. \\
& 3\Gamma_2(l) \left(\left[\frac{l}{p^2} + \frac{8l}{4p^2 - q^2} \right] \Lambda(l) \right. \\
& \quad - \frac{1}{p^2} + \frac{m_\pi^2 + l^2 + p^2}{q^2} \left[\frac{m_\pi^2 + (q^2 - 4p^2)}{p^2 B} + \frac{4m_\pi^2 + q^2}{B + q^2 l^2} \right] \\
& \quad \left. - \left[\frac{4m_\pi^2 - q^2}{B + q^2 l^2} (m_\pi^2 + l^2 + p^2) + \frac{4}{4p^2 - q^2} (2m_\pi^2 + 2l^2 - 2p^2 + q^2) \right] l\Omega(l) \right) \\
& + l\tilde{\Gamma}_3(l) \left(-2 \left[\frac{m_\pi^2}{p^2} + \frac{7m_\pi^2 + 7p^2 + l^2}{4p^2 - q^2} \right] \Lambda(l) + \frac{l}{q^2} \right. \\
& \quad + \frac{l}{2q^2} (m_\pi^2 + l^2 + p^2) \left[\frac{4m_\pi^2 (q^2 - 4p^2)}{p^2 B} + \frac{3(4m_\pi^2 + q^2)}{B + q^2 l^2} \right] \\
& \quad + \left[\frac{m_\pi^4 - (l^2 - p^2)^2}{q^2} + \frac{2}{4p^2 - q^2} (l^4 + 8l^2(m_\pi^2 + p^2) + 7(m_\pi^2 + p^2)^2) \right. \\
& \quad \left. \left. - \frac{1}{2} (3m_\pi^2 + 7l^2 + 3p^2) - \frac{3l^2}{B + q^2 l^2} (2m_\pi^2 + \frac{q^2}{2})(m_\pi^2 + l^2 + p^2) \right] \Omega(l) \right) \left. \right]. \tag{5.24}
\end{aligned}$$

The isovector central term is given by:

$$\begin{aligned}
V_{NN}^{med,cc} = & \frac{g_A^6 \vec{\tau} \cdot \vec{\tau}}{128 \pi^4 f_\pi^6} \int_0^\infty dl \left[\right. \\
& [3\Gamma_2(l) + l^2 \tilde{\Gamma}_3(l)] \left(\frac{q^2}{p^2} - \frac{(2m_\pi^2 + q^2)^2}{q^2(B + q^2 l^2)} (m_\pi^2 + l^2 + p^2) \right) \\
& + \frac{m_\pi^2}{B} \left[4(m_\pi^2 + p^2 - l^2) + \frac{4m_\pi^2 p^2 - q^4}{p^2 q^2} (m_\pi^2 + l^2 + p^2) \right] \\
& + \frac{l}{p^2} (8p^2 - q^2) \Lambda(l) \\
& \left. + \left[\frac{2m_\pi^2 + q^2}{B + q^2 l^2} (m_\pi^2 + l^2 + p^2) - 4 \right] (2m_\pi^2 + q^2) l \Omega(l) \right) - \frac{16k_f^3}{3} \left. \right].
\end{aligned} \tag{5.25}$$

Finally, there is an isovector spin-orbit term:

$$\begin{aligned}
V_{NN}^{med,2} = & \frac{g_A^6 \vec{\tau} \cdot \vec{\tau}}{256 \pi^4 f_\pi^6} i(\vec{\sigma}_1 + \vec{\sigma}_2) \cdot (\vec{q} \times \vec{p}) \int_0^\infty dl \left[\right. \\
& 4\Gamma_2(l) \left(\left[\frac{l}{p^2} + \frac{4l}{4p^2 - q^2} \right] \Lambda(l) - \frac{1}{p^2} + \frac{m_\pi^2}{B} \left[1 + \frac{m_\pi^2 + l^2}{p^2} + \frac{2}{q^2} (l^2 - m_\pi^2 - p^2) \right] \right. \\
& + \frac{2m_\pi^2 + q^2}{q^2(B + q^2 l^2)} (m_\pi^2 + p^2 - l^2) \\
& + \left[2 - \frac{4(m_\pi^2 + l^2 + p^2)}{4p^2 - q^2} + \frac{2m_\pi^2 + q^2}{B + q^2 l^2} (l^2 - m_\pi^2 - p^2) \right] l \Omega(l) \left. \right) \\
& + l \tilde{\Gamma}_3(l) \left(l(m_\pi^2 + p^2 - l^2) \left[\frac{2m_\pi^2 + q^2}{q^2(B + q^2 l^2)} + \frac{1}{B} \left(\frac{m_\pi^2 + l^2}{p^2} - \frac{4m_\pi^2}{q^2} - 1 \right) \right] \right. \\
& + \left[\frac{l^2 - m_\pi^2 - p^2}{p^2} + \frac{2(3l^2 + m_\pi^2 + p^2)}{4p^2 - q^2} \right] \Lambda(l) \\
& + \left[(m_\pi^2 + p^2 - l^2) \left(\frac{2m_\pi^2}{q^2} - \frac{(2m_\pi^2 + q^2)l^2}{B + q^2 l^2} \right) \right. \\
& \left. \left. + \frac{3l^2 + m_\pi^2 + p^2}{4p^2 - q^2} (2p^2 - 2m_\pi^2 - 2l^2 - q^2) \right] \Omega(l) \right) \left. \right].
\end{aligned} \tag{5.26}$$

The integral auxiliary functions $\Lambda(l)$, $\Omega(l)$ and B are defined below:

$$\Lambda(l) = \frac{1}{4p} \ln \left(\frac{m_\pi^2 + (l+p)^2}{m_\pi^2 + (l-p)^2} \right), \tag{5.27}$$

$$\Omega(l) = \frac{1}{q\sqrt{B + q^2 l^2}} \ln \left(\frac{ql - \sqrt{B + q^2 l^2}}{\sqrt{B}} \right), \tag{5.28}$$

$$B \equiv \left[m_\pi^2 + (l+p)^2 \right] \left[m_\pi^2 + (l-p)^2 \right]. \quad (5.29)$$

Lastly, the Γ auxiliary functions, $\tilde{\Gamma}_1(l)$, $\Gamma_2(l)$, $\tilde{\Gamma}_3(l)$, $\gamma_2(l)$ and $\tilde{\gamma}_3(l)$ are defined analytically as follows:

$$\tilde{\Gamma}_1(l) = \frac{k_f}{4l^2} (m_\pi^2 + k_f^2 + l^2) - \frac{1}{16l^3} \left[m_\pi^2 + (k_f + l)^2 \right] \left[m_\pi^2 + (k_f - l)^2 \right] \ln \left(\frac{m_\pi^2 + (k_f + l)^2}{m_\pi^2 + (k_f - l)^2} \right), \quad (5.30)$$

$$\begin{aligned} \Gamma_2(l) = & \frac{m_\pi^3}{3} \left[\arctan \left(\frac{k_f + l}{m_\pi} \right) + \arctan \left(\frac{k_f - l}{m_\pi} \right) \right] + \frac{k_f}{9} (k_f^2 - 3m_\pi^2) + \frac{k_f}{24l^2} (k_f^2 + m_\pi^2)^2 \\ & - \frac{k_f l^2}{24} + \frac{l^2 - k_f^2 - m_\pi^2}{96l^3} \left[(m_\pi^2 + k_f^2)^2 + l^4 + 2l^2(5m_\pi^2 - k_f^2) \right] \ln \left(\frac{m_\pi^2 + (k_f + l)^2}{m_\pi^2 + (k_f - l)^2} \right), \end{aligned} \quad (5.31)$$

$$\begin{aligned} \tilde{\Gamma}_3(l) = & \frac{k_f}{8} + \frac{k_f^3}{3l^2} - \frac{k_f}{8l^4} (k_f^2 + m_\pi^2)^2 \\ & + \frac{m_\pi^2 + k_f^2 - l^2}{32l^5} \left[m_\pi^2 + (k_f + l)^2 \right] \left[m_\pi^2 + (k_f - l)^2 \right] \ln \left(\frac{m_\pi^2 + (k_f + l)^2}{m_\pi^2 + (k_f - l)^2} \right), \end{aligned} \quad (5.32)$$

$$\begin{aligned} \gamma_2(l) = & -\frac{m_\pi}{2} \left[\arctan \left(\frac{k_f + l}{m_\pi} \right) + \arctan \left(\frac{k_f - l}{m_\pi} \right) \right] + \frac{k_f}{8l^2} (3l^2 - k_f^2 - m_\pi^2) \\ & + \frac{1}{32l^3} \left[k_f^4 m_\pi^4 - 3l^4 + 2l^2(3m_\pi^2 + k_f^2) \right] \ln \left(\frac{m_\pi^2 + (k_f + l)^2}{m_\pi^2 + (k_f - l)^2} \right), \end{aligned} \quad (5.33)$$

$$\begin{aligned} \tilde{\gamma}_2(l) = & \frac{k_f}{8l^4} (3m_\pi^2 + 3k_f^2 - l^2) \\ & + \frac{1}{32l^5} \left[l^4 - 2l^2(k_f^2 - m_\pi^2) - 3(m_\pi^2 + k_f^2)^2 \right] \ln \left(\frac{m_\pi^2 + (k_f + l)^2}{m_\pi^2 + (k_f - l)^2} \right). \end{aligned} \quad (5.34)$$

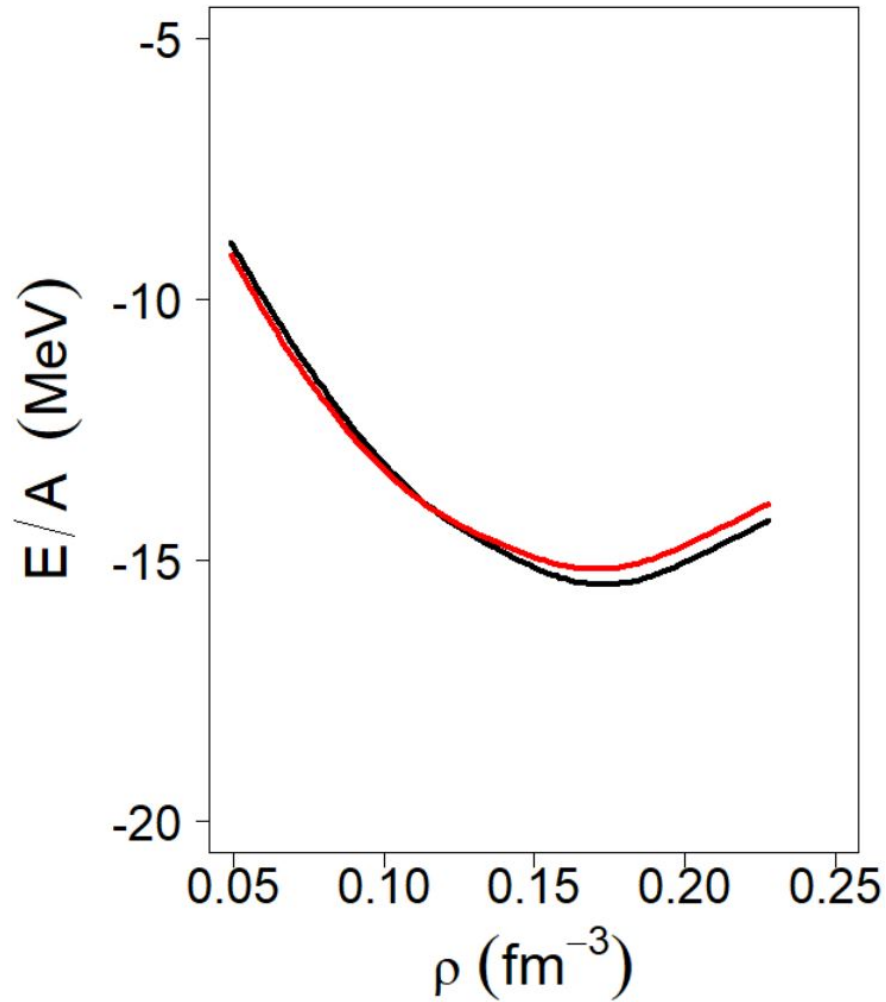


Figure 5.1: Black curve: the chiral EoS obtained with the 2NF and the 3NF at $N^2\text{LO}$. Red curve: 2NF and 3NF both at $N^3\text{LO}$.

5.2 The nuclear matter equation of state with three-nucleon forces at $N^3\text{LO}$

In this section, we show and discuss the EoS we obtain with the inclusion of the subleading 3NF contributions given in the previous section. We begin with discussing Fig. 5.1. There, the black curve represents the EoS consistently at $N^2\text{LO}$, whereas the red curve displays the EoS obtained with the 2NF and the 3NF up to $N^3\text{LO}$. The cutoff is fixed at 450 MeV, and the low-energy constants c_E , c_D of Ref. [76] are used. The predictions are very close, indicating good convergence.

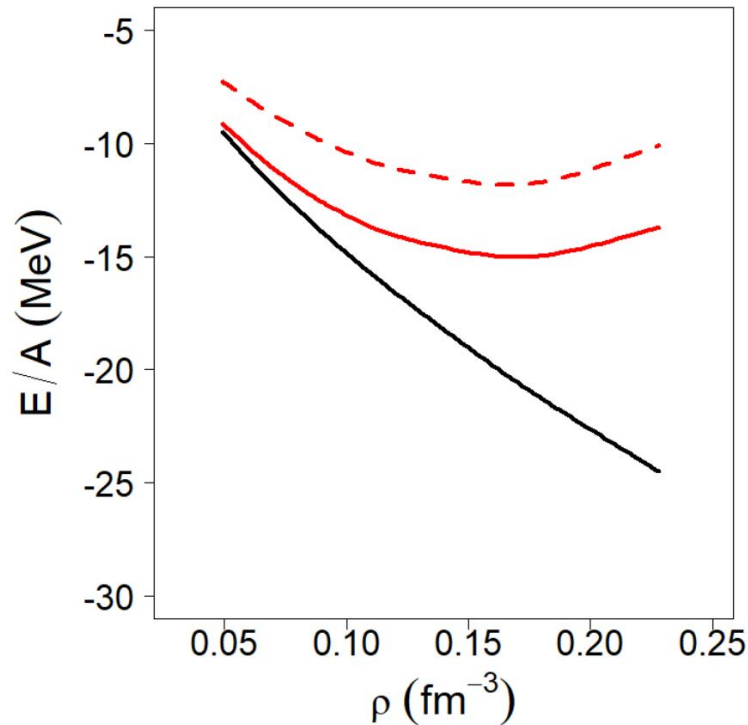


Figure 5.2: The chiral EoS at N^3 LO. The solid red line contains the 3NFs at N^2 LO as well as the long-range 3NF effects at N^3 LO, the dashed red line contains only 3NFs at N^2 LO, and the black line only contains 2NFs effects.

We see good agreement between our predictions with $\Lambda=450$ MeV, which is our standard choice, and the corresponding EoS predictions of Ref. [76], especially considering that we use a different many-body method (non-perturbative BHF instead of many-body perturbation theory) and we calculate the 3NF contribution by way of a density-dependent 2NF. At saturation, we estimate the differences to be in the order of 2 and 3% at N^3 LO and N^2 LO, respectively.

In closing this section, we wish to extract the contribution from the N^3 LO portion of the 3NF at N^3 LO, see Fig. 5.2. In this figure, the solid black curve is the result when only the 2NF at N^3 LO (with cutoff equal to 450 MeV) is applied. The solid red curve includes the entire 3NF up to N^3 LO, while the red dashed curve includes only the N^2 LO part of the total 3NF (solid red curve). Thus, the difference between the red dashed and the red solid curves represents the N^3 LO portion of the 3NF, which is moderately attractive. Note that the N^3 LO contribution to the 3NF is parameter-free [77, 198] and, therefore, this is a general result. Our conclusion is consistent with the findings of Ref. [79].

Chapter 6

Conclusion

In this work we have examined the nuclear EoS based on state-of-the-art few-nucleon forces. We determined this quantity from an appropriate many-body framework with these forces as input. We reported our EoS predictions, with the focus on neutron-rich matter. We applied the EoS to various neutron-rich systems of interest, including neutron-rich nuclei and neutron stars. Lastly, we discussed the importance of contributions from 3NFs to the SNM EoS and reported recent progress with the inclusion of higher-order contributions.

The NN potentials used in this work are based on χ EFT, which is established as a successful approach to deriving nuclear forces in the low energy domain in a systematic way while maintaining consistency with the symmetries of low-energy QCD. Following the BHF many-body method, we determined the EoS for both symmetric nuclear matter and neutron matter across five orders of the chiral expansion, thus exploring convergence issues.

We studied the properties of isospin-asymmetric matter and the symmetry energy, an important quantity whose density dependence, particularly the slope at saturation density, is closely related to the pressure in neutron matter around that density, which, in turn, plays a crucial role in the formation of the so-called neutron skin. We observed excellent convergence for the symmetry energy predictions, while stressing the importance of including the complete 3NF contributions to the nuclear potential at the third and fourth order of the chiral expansion. Using a semi-empirical mass formula inspired energy-density functional, we obtained predictions for the neutron skins in ^{48}Ca and ^{208}Pb . These quantities are expected to be measured in the near future with unprecedented accuracy, making theoretical predictions important and timely.

The mass-radius relationship in neutron stars is of unique interest to nuclear physics because

of its direct dependence on the pressure in neutron matter and, thus, on the NM EoS. Typical neutron star predictions are constrained [190] by only three assumptions: 1) General Relativity is the appropriate theory; 2) the EoS is constrained by Le Chatelier's principle ($\partial P/\partial\epsilon \geq 0$), and finally; 3) the causality condition, which requires the speed of sound in stellar matter to be less than the speed of light.

We constructed the EoS in β -equilibrium matter by including contributions from lepton energies. Since the densities within neutron stars reach values well above the applicability of χ EFT, we extended the chiral EoS predictions using piecewise polytropes. We then employed the TOV stellar structure equations. We found the predicted neutron star radii for the canonical mass neutron star to be insensitive to the EoS above $3\rho_0$. Estimating the overall theoretical uncertainty, we determined that our predictions fall in the range 10.8 - 12.8 km, which is in good agreement with the constraints extracted from a variety of recent sources, including those derived from the LIGO-Virgo observations.

The 3NFs produce important contributions to the EoS. Currently, the leading 3NFs are well studied and have been incorporated with a good degree of success. Of course, for robust conclusions about the convergence of the chiral EoS, the inclusion of subleading 3NFs is critical. In Chapter 5, we evaluate all long-range sub-leading 3NFs cast in the form of effective density dependent NN potentials. We illustrated the effects of the leading and subleading 3NFs on the EoS and found that the N³LO part of the long-range 3NF is attractive. This contribution is parameter-free, and thus this is a general result.

Current and planned experiments such as the CREX [122] and PREX-II [121], along with combined effort from the MESA [123], FAIR [201] and FRIB [202] facilities seek to place empirical constraints on the neutron skin of neutron-rich nuclei and, as a consequence, place constraints on the closely related nuclear symmetry energy. Additional constraints on the nuclear EoS from multi-messenger astronomy are expected in the coming years. The combined ongoing efforts from theory, experiment, and observation provide an optimistic outlook for future progress.

References

- [1] K.A. Brueckner, C.A. Levinson, H.M. Mahmoud, *Phys Rev.* **95**, 217 (1954).
- [2] K.A. Brueckner, *Phys Rev.* **100**, 36 (1955).
- [3] H.A. Bethe, *Phys Rev.* **103**, 1353 (1956).
- [4] J. Goldstone, *Proc. R. Soc. London*, **A239**, 267 (1957).
- [5] B. Brandow, *Rev. Mod. Phys.* **39**, 771 (1967).
- [6] B. Day, *Rev. Mod. Phys.* **39**, 719 (1967).
- [7] H. Thompson, *Phys. Rev., D.* **1** 110, 17 (1970).
- [8] M. Haftel and F. Tabakin. *Nucl. Phys. A.* **158**, 1 (1970).
- [9] H.A. Bethe, *Annu. Rev. Nucl. Sci.* **21**, 93 (1971).
- [10] M.R. Anastasio, L.S. Celenza, W.S. Pong, C.M. Shakin, *Phys. Rep.* **100**, 327 (1983).
- [11] R. Brockmann and R. Machleidt, *Phys. Lett.* **149B**, 283 (1984).
- [12] B.D. Serot and J.D. Walecka, *Adv. Nuc. Phys.* **16**, 1 (1986).
- [13] B. ter Haar and R. Malfliet, *Phys. Rev. Lett.* **56**, 1237 (1986).
- [14] C.J. Horowitz and B.D. Serot, *Nucl. Phys. A* **464**, 613 (1987).
- [15] B. ter Haar and R. Malfliet, *Phys. Rev. Lett. Phys. Rep.* **149**, 207 (1987).
- [16] C.J. Horowitz and B.D. Serot, *Phys. Rev. C* **42**, 1965 (1990).
- [17] H. Meuther, F. Sammarruca, Z. Ma, *Int. J. Mod. Phys. E* **26**, 173001 (2017).
- [18] V.R. Pandharipande and R.B. Wiringa, *Rev. Mod. Phys.* **51**, 821 (1979).

- [19] I.E. Lagaris and V.R. Pandharipande, *Nuc. Phys. A* **359**, 349 (1981).
- [20] T. Frick and H. Muether, *Phys. Rev. C* **68**, 034310 (2003).
- [21] J.G. Hirsch, J.E. Escher, O. Castanos, S. Pittel, G. Stoitcheva, *World Scientific*, 1 (2004).
- [22] T.H.R. Skyrme, *Nucl. Phys.* **9**, 635 (1959).
- [23] J. Decharge and D. Gogny, *Phys. Rev. C* **21**, 1568 (1980).
- [24] M. Bender and PH. Heenen, *Rev. Mod. Phys.* **75**, 121 (2003).
- [25] P.F. Bedaque, U. van Kolck, *Ann. Rev. Nuc. Part. Sci.* **52**, 339 (2002).
- [26] R.B. Wiringa, V.G.J. Stoks, R. Schiavilla, *Phys. Rev. C* **51**, 38 (1995).
- [27] R.V. Reid, *Ann. Phys.* **50**, 411 (1968).
- [28] Q.B. Shen, Y.L. Han, and H.R. Guo, *Phys. Rev. C* **80**, 024604 (2009).
- [29] M.M. Nagels, T.A. Rijken, J.J. de Swart, *Phys. Rev. D* **17**, 768 (1978).
- [30] J.J. de Swart, R.A.M.M. Klomp, M.C.M. Rentmeester, T.A. Rijken, *In: Guardiola R. (eds) Few-Body Problems in Physics '95. Few-Body Systems* vol. **8**. Springer, Vienna (1995).
- [31] M. Lacombe, B. Loiseau, J.M. Richard, R. Vinh Mau, J. Cote, P. Pires, R. de Tournreil, *Phys. Rev. C* **21**, 861 (1980).
- [32] R. Machleidt, K. Holinde, C. Elster, *Phys. Rept.* **149**, 1 (1987).
- [33] K. Holinde, The Bonn Potential. *In: Guardiola R. (eds) Few-Body Problems in Physics '95. Few-Body Systems* vol. **8**. Springer, Vienna (1995).
- [34] R. Machleidt, *In: J.W. Negele, E. Vogt, (eds) Advances in Nuclear Physics. Advances in Nuclear Physics* vol **19**. Springer, Boston, MA (1989).
- [35] R. Machleidt, *Phys. Rev. C* **63**, 024001 (2001).
- [36] F. Gross and A. Stadler, *Phys. Rev. C* **78**, 014005 (2008).
- [37] A.C. Cordon and E.R. Arriola, *Phys. Rev. C* **81**, 044002 (2010).

- [38] S. Weinberg, *Phys. Lett. B* **251**, 288 ; *Nucl. Phys. B* **363**, 3 (1990).
- [39] S. Weinberg, *Phys. Lett. B* **295**, 114 (1992).
- [40] C. Ordonez, L. Ray, U. van Kolck, *Phys. Rev. Lett.* **72**, 1982 (1994).
- [41] R. Machleidt and I. Slaus, *J. Phys. G* **27**, R69 (2001).
- [42] E. Epelbaum, A. Nogga, W. Glockle, H. Kamada, Ulf-G. Meissner, H. Witala, *Phys. Rev. C* **66**, 064001 (2002).
- [43] D.R. Entem and R. Machleidt, *Phys. Rev. C* **66**, 014002 (2002).
- [44] D.R. Entem, R Machleidt, *Phys. Rev. C* **68**, 041001 (2003).
- [45] E. Epelbaum, W. Gloeckle, U. Meissner, *Eur. Phys. J. A* **19**, 401 (2004).
- [46] E. Epelbaum, *Prog. Part. Nuc. Phys* **57**, 654 (2006).
- [47] E. Epelbaum, H.W. Hammer, Ulf-G. Meissner, *Rev. Mod. Phys.* **81**, 1773 (2009).
- [48] D. Gazit, S. Quaglioni, P. Navratil, *Phys. Rev. Lett.* **103**, 102502 (2009).
- [49] R. Machleidt and D.R. Entem, *Phys. Rep.* **503**, 1 (2011).
- [50] E. Marji, A. Canul, Q. MacPherson, R. Winzer, Ch. Zeoli, D. R. Entem, R. Machleidt, *Phys. Rev. C* **88**, 054002 (2013).
- [51] R. Machleidt, *Scholarpedia* **9**(1), 30710 (2014).
- [52] E. Epelbaum, H. Krebs, U.-G. Meissner, *Phys. Rev. Lett.* **115**, 122301 (2015).
- [53] R. Machleidt, D.R. Entem, N. Kaiser, Y. Nosyk, *Proc. Sci. 8th Intl. W.S. Chrl. Dyn.* (2015).
- [54] D.R. Entem, R. Machleidt, Y. Nosyk, *Phys. Rev. C* **96**, 024004 (2017).
- [55] R. Machleidt, *IOP Conf. Series Jour. Phys. : Conf. Series* **966**, 012011 (2018).
- [56] R. Machleidt, *arXiv:1901.01473 [nucl-th]* (2019).
- [57] R. Machleidt and F. Sammarruca, *Euro. Phys. Jour. A* **56**, 95 (2020).

- [58] U. van Kolck, *Front. in Phys.* **8**, 00079 (2020).
- [59] R. Machleidt, “Nuclear Forces - Lecture 7 - Recent Developments” *2016 Nuclear Physics School* APCTP Headquarters, Pohang, Lecture (2016).
- [60] H. Fritzsche, M. Gell-Mann, H. Leutwyler, *Phys. Lett. B* **47**, 365 (1973).
- [61] T. Muta, *Lecture Notes in Physics* **78**: 3rd ed. *World Scientific*. (2009).
- [62] J. Greensite, *Lecture Notes in Physics* **821**: 1st ed. *Springer-Verlag Berlin Heidelberg* (2011).
- [63] S.R. Beane, P.F. Bedaque, K. Orginos, and M.J. Savage, *Phys. Rev. Lett.* **97**, 012001 (2006).
- [64] W. Detmold and K. Orginos, *Phys. Rev. D* **87**, 114512 (2013).
- [65] T. Yamazaki, *LATTICE-2013, Proc. Sci.* **187** (2013).
- [66] M.J. Savage, *arXiv:1309.4752 [nucl-th]* (2013).
- [67] M. Hoferichter, J. Ruiz de Elvira, B. Kubis, U.G. Meissner, *Phys. Rev. Lett.* **115**, 192301 (2015).; *Phys. Rep.* **625**, 1 (2016).; *EPJ Web Conf.* **137**, 01014 (2017).
- [68] A. Gardestig and D.R. Phillips, *Phys. Rev. Lett.* **96**, 232301 (2006).
- [69] L.E. Marcucci, A. Kievsky, S. Rosati, R. Schiavilla, M. Viviani, *Phys. Rev. Lett.* **108**, 052502 ; **121**, 049901(E) (2012).
- [70] J.W. Holt, N. Kaiser, W. Weise, *Phys. Rev. C* **81**, 024002 (2010).
- [71] P.A. Zyla *et al.* (Particle Data Group), *Prog. Theor. Exp. Phys.* 2020, 083C01 (2020).
- [72] N. Kaiser and V. Niessner, *Phys. Rev. C* **98**, 054002 (2018).
- [73] F. Sammarruca and R. Millerson, *arXiv:2005.01958 [nucl-th]* (2020).
- [74] P. Navratil, *Few-Body Syst.* **47**, 117 (2007)
- [75] C. Drischler, A. Carbone, K. Hebeler, A. Schwenk, *Phys. Rev. C* **94**, 054307 (2016).
- [76] C. Drischler, K. Hebeler, A. Schenk, *Phys Rev. Lett.* **122**, 042501 (2019).

- [77] N. Kaiser and B. Singh, *Phys. Rev. C* **100**, 014002 (2019).
- [78] I. Tews, T. Krueger, K. Hebeler, A. Schwenk, *Phys. Rev. Lett.* **110**, 032504 (2013).
- [79] K. Hebeler, H. Krebs, E. Epelbaum, J. Golak, R. Skibinski, *Phys. Rev. C* **95**, 044001 (2015).
- [80] H. Krebs, A. Gasparyan, E. Epelbaum. *Phys. Rev. C* **85**, 054006 (2012).
- [81] R. B. Wiringa, V. Fiks, A. Fabrocini, *Phys. Rev. C* **38**, 2 (1988).
- [82] W.D. Myers, *At. Data Nucl. Data Tables* **17**, 411 (1976); H. V. Groote, E.R. Hilf, and K. Takahashi, *ibid.* **17**, 418 (1976); P. A. Seeger and W. M. Havard, *ibid.* **17**, 428 (1976); M. Bauer, *ibid.* **17**, 442 (1976); J. Janecke and B. P. Eynon, *ibid.* **17**, 467 (1976).
- [83] R. Millerson and F. Sammarruca, *arXiv:1906.02905* (2019).
- [84] F. Sammarruca and R. Millerson, *Front. Phys.* **7**, 213 (2019).
- [85] F. Sammarruca, *Symmetry* **6**, 851 (2014).
- [86] M. Baldo and G.F. Burgio, *Prog. Part. Nucl. Phys.* **91**, 203 (2016).
- [87] S. Burrello¹, M. Colonna, H. Zheng, *Front. Phys.* **7**, 53 (2019).
- [88] K.A. Bruckner, S.A. Coon, J. Dabrowski, *Phys. Rev.* **168**, 1184 (1968).
- [89] B.K. Agrawal, J.N. De, S.K. Samaddar, *Phys. Rev. Lett.* **109**, 262501 (2012).
- [90] P. Moeller, W.D. Myers, H. Sagawa, S. Yoshida, *Phys. Rev. Lett.* **108**, 052501 (2012).
- [91] P. Moeller, A.J. Sierk, T. Ichikawa, H. Sagawa, *Atomic Data and Nuclear Tables* **109**, 1 (2016).
- [92] F.J. Fattoyev, C.J. Horowitz, J. Piekarewicz, G. Shen, *Phys. Rev. C* **82**, 055803 (2010).
- [93] G.A. Lalazisis, J. Konig, P. Ring, *Phys. Rev. C* **55**, 540 (1997).
- [94] B.A. Brown, *Phys. Rev. Lett.* **85**, 5296 (2000).
- [95] B.M. Santos, M. Dutra, O. Lourenco, A. Delfino, *Jour. Phys. Conf. Ser.* **630**, 012033 (2015).
- [96] C. Mondal, B.K. Agrawal, J.N. De, S.K. Samaddar, M. Centelles, X. Vinas, *Proc. DAE Symp. Nucl. Phys.* **62**, 72 (2017).

- [97] C. Mondal, B.K. Agrawa, J.N. De, S.K. Samaddar, *Int. Jour. Mod. Phys. E* **27**, 1850078 (2018).
- [98] Hui Tong, Xiu-Lei Ren, Peter Ring, Shi-Hang Shen, Si-Bo Wang, Jie Meng, *Phys. Rev. C* **98**, 054302 (2018).
- [99] J.W. Holt, Y. Lim, *Phys. Lett. B* **784**, 77 (2018).
- [100] B. K. Agrawal, J.N. De, S.K. Samaddar, G. Colo, A. Sulaksono, *Phys. Rev. C* **87**, 051306 (2013).
- [101] X. Vinas, M. Centelles, X. Roca-Maza, M. Warda, *AIP Conf. Proc.* **1606**, 256 (2014).
- [102] I. Vidana, C. Providencia, A. Polls, A. Rios, *Phys. Rev. C* **80**, 045806 (2009).
- [103] C. Ducoin, J. Margueron, C. Providencia, I. Vidana, *Phys. Rev. C* **83**, 045810 (2010).
- [104] B.M. Santos, M. Dutra, O. Lourenco, A. Delfino, *Phys. Rev. C* **90**, 054317 (2014).
- [105] J. Piekarewicz, F. Fattoyev, *Physics Today*, **72**, 7, 30 (2019).
- [106] X. Roca-Maza, M. Centelles, X. Vinas, M. Warda, *Phys. Rev. Lett.* **106**, 252501 (2011).
- [107] I. Hamamoto and X. Z. Zhang, *Phys. Rev. C* **52**, R2326(R) (1995).
- [108] N. Alam, B.K. Agrawal, J.N. De, S.K. Samaddar, G. Colo, *Phys. Rev. C* **90**, 054317 (2014).
- [109] P. Danielewicz, J. Lee, *Nucl. Phys. A* **922**, 1 (2014).
- [110] M.B. Tsang, Y. Zhang, P. Danielewicz, M. Famiano, Z. Li, W.G. Lynch, et al., *Phys. Rev. Lett.* **102**, 122701 (2009).
- [111] P. Russotto, S. Gannon, S. Kupny, P. Lasko, L. Acosta, M. Adamczyk, et al., *Phys. Rev. C* **94**, 034608 (2016).
- [112] P. Russotto, P.Z. Wu, M. Zoric, M. Chartier, Y. Leifels, R.C. Lemmon, et al., *Phys. Lett. B* **697**, 471 (2011).
- [113] R.J. Furnstahl, *Nucl. Phys. A* **706**, 85 (2002).

- [114] C.M. Tarbert et al., (Crystal Ball at MAMI and A2 Collaboration), *Phys. Rev. Lett.* **112**, 242502 (2014).
- [115] J. Mammei, Proceedings of CIPANP 2012, *arXiv:1209.3179 [nucl-ex]* (2012)
- [116] A. Gardestig, C.J. Horowitz, G.A. Miller, *arXiv:1504.08347 [nucl-th]* (2015)
- [117] K. Oyamatsu, K. Iida, H. Koura, *Phys Rev C* **82**, 027301 (2010).
- [118] F. Sammarruca and Y. Nosyk, *Phys. Rev. C* **94**, 044311 (2016).
- [119] D.S. Ahn et al., *RIKEN Accel. Prog. Rep.* **51**, 82. (2018).
- [120] M. Thiel, C. Sfienti, J. Piekarewicz, C.J. Horowitz, M. Vanderhaegen, *Jour. Phys. G Nucl. Part. Phys.* **46**, 9 (2019).
- [121] P.A. Souder et al., *Proposal for Jefferson Lab PAC 38*, (2011)
- [122] J. Mammei, D. McNulty, R. Michaels, K. Paschke, S. Riordan, P.A. Souder, *CREX: Parity-Violating Measurement of the Weak Charge Distribution of ^{48}Ca to 0.02 fm Accuracy* (2013).
- [123] D. Becker et al., *Eur. Phys. J.* **A54**, 208 (2018).
- [124] X. Vinas, M. Centelles, X. Roca-Maza, M. Warda, *Eur. Phys. J* **A50**, 27 (2014).
- [125] M. Warda, X. Vias, X. Roca-Maza, M. Centelles, *Phys. Rev. C* **80**, 0243316 (2009).
- [126] C. Xu, B. Li, L. Chen, C.M. Ko, *Nucl. Phys. A* **865**, 1 (2011).
- [127] X. Roca-Maza, M. Brenna, B.K. Agrawal, P.F. Bortignon, G. Colo, L.G. Cao, N. Paar, D. Vretenar, *Phys. Rev. C* **87**, 034301 (2013).
- [128] T. Inakura, N. Nakada, *Phys. Rev. C* **92**, 064301 (2015).
- [129] F. Sammarruca, *Phys. Rev. C* **94**, 054317 (2016).
- [130] F. Sammarruca, *Front. in Phys.* **6**, 90 (2018).
- [131] C.J. Horowitz, J. Piekarewicz, *Phys. Rev. Lett.* **86**, 5647 (2001).
- [132] C.J. Horowitz, J. Piekarewicz, *Phys. Rev. C* **64**, 062802 (2001).

- [133] J.M. Lattimer *Phys. Rev. Lett.* **928**, 276 (2014).
- [134] N.K. Glendenning, *Compact Stars* 2nd edn, *Berlin: Springer* (1996).
- [135] A. Burrows, *Rev. Mod. Phys.* **85**, 245 (2013).
- [136] I. Vidana, *arXiv* arXiv:1805.00837 [nucl-th] (2018).
- [137] J. Chadwick, *Nature* **129**, 312 (1932).
- [138] W. Baade and F. Zwicky, *Proc. Nat. Acad. Sci* **20**(5), 254 (1934).
- [139] W. Baade and F. Zwicky, *Phys. Rev. Jour. Arch.* **46**, 76 (1934).
- [140] R.C. Tolman, *Phys. Rev. C* **55**, 364 (1939).
- [141] J.R. Oppenheimer and G.M. Volkoff, *Phys. Rev. C* **55**, 374 (1939).
- [142] A. G. W. Cameron, *Astrophys. J* **130**, 916 (1959).
- [143] V. A. Ambartsumyan and G. S. Saakyan, *Astron. Zh.* **37**, 193 (1960).
- [144] E. E. Salpeter, *Ann. Phys. (N.Y.)* **11**, 393 (1960).
- [145] D. Ivanenko and D. F. Kurdgelaidze, *Astrofizika* **1**, 479 (1965).
- [146] S. Tsuruta and A. G. W. Cameron, *Canadian J. Phys.* **44**, 1895 (1966).
- [147] A. B. Migdal, *Zh. Eksp. Teor. Fiz.* **61**, 2209 (1971).
- [148] R. F. Sawyer, *Phys. Rev. Lett.* **29**, 382 (1972).
- [149] R. F. Sawyer and D. J. Scalapino, *Phys. Rev. D* **7**, 953 (1972).
- [150] D. B. Kaplan and A. E. Nelson, *Phys. Lett. B* **175**, 57 (1986).
- [151] D. Ivanenko and D. F. Kurdgelaidze, *Lett. Nuovo Cimento* **2**, 13 (1969).
- [152] D. Blaschke, J. Schaffner-Bielich and H. J. Schulze, Eds. Topical issue on exotic matter in neutron stars, *Eur. Phys. J. A* **52**, 71 (2016).
- [153] M. Oertel, M. Hempel, T. Kahn and S. Typel, *Rev. Mod. Phys.* **89**, 015007 (2017).

- [154] G. F. Burgio and A. F. Fantina, arXiv:1804.03020. To appear in the White Book of “New-Compstar” European COST Action MP1304 (2018).
- [155] R. Stabler, Ph. D. thesis (Cornell University), (1960) unpublished.
- [156] H.-Y. Chiu, *Ann. Phys.* **26**, 364 (1964).
- [157] S. Tsuruta and A. G. W. Cameron, *Canadian J. Phys.* **44**, 1863 (1966).
- [158] D.G. Yakovlev, K.P. Levenfish and Yu. A. Shibano, *Uspekhi Fiz. Nauk.* **169**, 825 (1999).
- [159] F. Pacini, *Nature* **216**, 567 (1967).
- [160] A. Hewish, S.J. Bell, J.D.H. Pilkington, P.F. Scott, R.A. Collins, *Nature* **217**, 709 (1968).
- [161] T. Gold, *Nature* **218**, 731 (1968).
- [162] M.I. Large, A.E. Vaughan, B.Y. Mills, *Nature* **220**, 340 (1968).
- [163] E.C. Reifenstein, W.D. Brundage, D.H. Staelin, **22**, 7 (1969).
- [164] R.N. Manchester, *IOP Conf. Ser. Jour. Phys.* **932**, 012001 (2017).
- [165] R.A. Hulse and J.H. Taylor, *Astro. Phys. Jour* **195**, L51 (1975).
- [166] S. Johnston, R.N. Manchester, A.G. Lyne, M. Bailes, V.M. Kaspi, G. Qiao, N. DAmico, *Astro. Phys. Jour* **387**, L37 (1992).
- [167] A.G. Lyne, A. Brinklow, J. Middleditch, S.R. Kulkarni, D.C. Backer, T.R. Clifton, *Nature* **328**, 399 (1987).
- [168] A. Wolszczan and D.A. Frail, *Nature* **355**, 145 (1992).
- [169] M.A. McLaughlin et al., *Nature* **439**, 817 (2006).
- [170] J. van Paradijs, R.E. Taam, E.P.J. van den Heuvel, *Astron. Astrophys.* **299**, L41 (1995).
- [171] B.P. Abbott et al., *LIGO Scientific Collaboration and Virgo Collaboration Phys. Rev. Lett.* **119**, 161101 (2017).
- [172] B.P. Abbott et al., *Astro.Phys. Jour. Lett.* **848**, 2 (2017).

- [173] A. Mann, *nature* **579**, 20 (2020).
- [174] K.C. Gendreau et al., *SPIE* **8443**, 13 (2012).
- [175] C.M. Zhang, J. Wang, Y.H. Zhao, H.X. Yin, L.M. Song, D.P. Menezes, D.T. Wickramasinghe, L. Ferrario, P. Chardonnet, *Astro. Astro.phys.* **527**, A83 (2011).
- [176] J.G. Martinez, K. Stovall, P.C.C. Freire, J.S. Deneva, F.A. Jenet, M.A. McLaughlin, M. Bagchi, S.D. Bates, A. Ridolfi, *Astro.phys. Jour.* **812**, 2 (2015).
- [177] H.T. Cromartie et al., *Nature Astro.* **4**, 72 (2020).
- [178] A.W. Steiner, J.M. Lattimer, E.F. Brown, *Ap.J.* **765**, L5 (2013).
- [179] E. Annala, T. Gorda, A. Kurkela, A. Vuorinen, *Phys. Rev. Lett.* **120**, 172703 (2018).
- [180] E.M. Cackett et al., *Ap.J.* **674**,1 (2008).
- [181] T. M. Tauris, D. Sanyal, S.C. Yoon, N. Langer, *Astron. Astrophys.* **558**, A39 (2013).
- [182] J. Schwab, E. Quataert, L. Bildsten, *Mon. Not. Royal Astro. Soc.* **453**, 2 (2015).
- [183] A.J. Ruiter, L. Ferrario, K. Belczynski, I.R. Seitenzahl, R.M. Crocker, A.I. Karakas, *Mon. Not. Royal Astro. Soc.* **484**, 1 (2019).
- [184] J.M. Lattimer and A.W. Steiner, *Astrophys. Jour.*, **784**, 123 (2014).
- [185] W.G. Newton, M. Gearheart, J. Hooker, B.A. Li, *Neutron Star Crust*, C.A. Bertulani, J. Piekarewicz, (Hauppauge, NY: *Nova Science Pub. Inc.*), chapter 12 (2011).
- [186] M.B. Tsang et al., *Phys. Rev. C* **86**, 015803 (2012).
- [187] J.M. Lattimer and Y. Lim, *Ap.J* **771**, 51 (2013).
- [188] A.W. Steiner and S. Gandolfi, *Phys. Rev. Lett.* **108**, 081102 (2012).
- [189] K. Hebeler, J.M. Lattimer, C.J. Pethick, A. Schwenk, *Ap.J.* **773**, 11 (2013).
- [190] C.D. Rhoades, R. Ruffini, *Phys. Rev. Lett.* **32**, 324 (1974).
- [191] J.B. Hartle, *Phys. Rep.* **46**, 201 (1978).

- [192] J.S. Read, B.D. Lackey, B.J. Owen, J.L. Friedman, *Phys. Rev. D* **79**, 124032 (2009).
- [193] F. Sammarruca and Randy Millerson, *Jour. Phys. G: Nucl. Part. Phys.* **46**, 024001 (2019).
- [194] F. Weber, *Pulsars as Astrophysical Laboratories for Nuclear and Particle Physics*, Bristol :
Institute of Physics Publishing (1999).
- [195] J. Antoniadis, P.C.C. Freire, N. Wex, T.M. Tauris, R.S. Lynch, M.H. van Kerkwijk, *Science*,
340, 6131 (2013).
- [196] B.K. Harrison, J.A. Wheeler, *Gravitational Theory and Gravitational Collapse*, Chicago, IL:
University of Chicago (1965).
- [197] J.W. Negele, D. Vautherin, *Nucl. Phys.* **A207**, 298 (1973).
- [198] V. Bernard, E. Epelbaum, H. Krebs, U.G. Meissner, *Phys. Rev. C* **77**, 064004 (2008).
- [199] J.W. Holt, M. Kawaguchi, N. Kaiser, *Front. Phys.* **8**, 100 (2020).
- [200] V. Bernard, E. Epelbaum, H. Krebs, and Ulf-G. Meissner, *Phys. Rev. C* **84**, 054001 (2001).
- [201] M. Durante et al., *Phys. Scr.* **94**, 3 (2019).
- [202] FRIB Users Organization for the NSAC Long Range Plan Implementation Subcommittee,
FRIB: Opening New Frontiers in Nuclear Science (2012).

Appendix A

Deriving the EoS for β -Stable Matter

A.1 Electron Contributions

In this appendix we evaluate the fraction of each particle species in β -stable matter. Throughout this appendix we will use the following unit conventions: momentum is given in inverse fermi (fm^{-1}), density in inverse fermi cubed (fm^{-3}), energy per particle and chemical potential are given in megaelectronvolts (MeV), energy density is given in MeV per fermi cubed (MeV/fm^3). To convert between units, we use the standard conversion factor, $\hbar c \equiv 197.327 \text{ MeV fm}$. Masses are given in units of energy.

We start by writing the relationship between Fermi momentum and density for leptons using Eq. (4.4) and Eq. (4.7):

$$k_{F_i} = (3\pi^2 Y_i \rho)^{\frac{1}{3}}. \quad (\text{A.1})$$

Since the typical momentum of the electrons is much larger than the electron mass-energy, $(\hbar c)k_e \gg m_e$, where $m_e = 0.511 \text{ MeV}$, we apply the ultra-relativistic approximation and evaluate Eq. (4.2) as follows:

$$\epsilon_e = \frac{1}{\pi^2} \int_0^{k_{F_i}} (\hbar c k) k^2 dk = \frac{\hbar c}{4\pi^2} k_{F_i}^4 = \frac{\hbar c}{4\pi^2} (3\pi^2 \rho_e)^{\frac{4}{3}}. \quad (\text{A.2})$$

Converting energy density into energy per baryon (Eq. (4.5)), we write the electron energy

per baryon as a function of the electron fraction, Y_e :

$$e_e = \frac{\hbar c}{4\pi^2} \rho^{\frac{1}{3}} (3\pi^2 Y_e)^{\frac{4}{3}} \quad \Rightarrow \quad Y_e(\rho) = \left(\frac{4\pi^2}{(3\pi^2)^{\frac{4}{3}}} \frac{e_e(\rho)}{\hbar c \rho^{\frac{1}{3}}} \right)^{\frac{3}{4}}. \quad (\text{A.3})$$

Since the chemical potential of the muons must equal the one of the electrons, per Eq. (4.19) the following equivalency holds true:

$$\frac{\partial e_e}{\partial Y_e} = \frac{\hbar c}{3\pi^2} (3\pi^2)^{\frac{4}{3}} (\rho Y_e)^{\frac{1}{3}} = \frac{\partial e_\mu}{\partial Y_\mu}. \quad (\text{A.4})$$

The muon contribution is discussed next.

A.1.1 Muon Contribution

The non-relativistic approximation may be employed for the muon energy because, especially at moderate densities, the comparatively large muon mass – equal to 105.7 MeV – dominates the muon chemical potential, $m_\mu \gg (\hbar c)k_\mu$. Actually, the non-relativistic approximation holds valid also at higher densities because the fraction of muons remains low (see Fig. 4.2), and, as a consequence, so does the muon Fermi momentum, Eq. (A.1). The chemical potential is then approximated by the non-relativistic kinetic energy plus the mass-energy. Evaluation of the energy density integral gives:

$$\epsilon_\mu \approx \frac{1}{\pi^2} \int_0^{k_{f_i}} \left(\frac{(\hbar c k)^2}{2m_\mu} + m_\mu \right) k^2 dk = \frac{(\hbar c)^2}{10\pi^2 m_\mu} (3\pi^2 \rho_\mu)^{\frac{5}{3}} + m_\mu \rho_\mu, \quad (\text{A.5})$$

and thus the total muon energy per baryon (Eq. (4.5)) is:

$$e_\mu \approx \frac{(\hbar c)^2}{10\pi^2 m_\mu} \rho^{\frac{2}{3}} (3\pi^2 Y_\mu)^{\frac{5}{3}} + Y_\mu m_\mu. \quad (\text{A.6})$$

Applying Eq. (A.6) and Eq. (A.4), we can express the electron fraction as a function of the muon fraction using:

$$Y_e(\rho, Y_\mu) = \left(\frac{\hbar c}{2m_\mu} [3\pi^2 \rho Y_\mu^2]^{\frac{1}{3}} + \frac{m_\mu}{\hbar c [3\pi^2 \rho]^{\frac{1}{3}}} \right)^3. \quad (\text{A.7})$$

Alternatively, we can treat the muon energy density exactly and evaluate the integral in Eq. (4.2) directly. This can be done analytically and yields:

$$\epsilon_\mu = \frac{1}{4\pi^2} \left[\mu_\mu k_{F_\mu} \left(\mu_\mu^2 - \frac{1}{2} m_\mu \right) - \frac{1}{2} m_\mu^4 \ln \left(\frac{\mu_\mu + k_{F_\mu}}{m_\mu} \right) \right]. \quad (\text{A.8})$$

It is now a straightforward task to evaluate the muon energy per baryon as a function of density using Eqs. (A.1), (A.8), and (4.5). The electron fraction in terms of the muon fraction is simply obtained from Eqs. (4.6), (4.8), and (A.4):

$$Y_e(\rho, Y_\mu) = \frac{\left((\hbar c [(3\pi^2 Y_\mu \rho)^{\frac{1}{3}}]^2 + m_\mu^2) \right)^{\frac{3}{2}}}{(\hbar c)^3 (3\pi^2 \rho)}. \quad (\text{A.9})$$

A.1.2 Evaluating Particle Fractions

With the expressions relating the lepton energy per baryon and the lepton fractions, we are now in the position to simultaneously solve Eqs. (4.1), (4.19), and (4.20). We begin by combining Eq. (4.20) and Eq. (4.8):

$$\frac{\partial e_p}{\partial Y_p} = \frac{\partial e_n}{\partial Y_n} - \frac{\partial e_e}{\partial Y_e}, \quad (\text{A.10})$$

and then use Eqs. (4.1) and A.10 to obtain:

$$-4 e_{sym}(\rho) (1 - 2 \cdot Y_p) + (m_p - m_n) + e_e = 0. \quad (\text{A.11})$$

With Eqs. (4.10), (A.11) and either Eq. (A.7) or Eq. (A.9), we have three equations in three unknowns from which the muon, electron and proton fractions can be determined at a given density. Of course, if the muon fraction is zero (the electron chemical potential is lower than the muon mass), we simply set Y_e equal to Y_p . Once the proton fraction is known, the neutron fraction can be determined from total baryon density conservation.

It is then a simple matter to calculate the total energy per baryon, e_T , by summing the individual energy per particle for each species, e_i .

Appendix B

Numerical Tables of Results from Chapter 4

This appendix contains predictions derived in Chapter 4 for the β -stable EoS and neutron star properties in tabular form.

Table B.1: β -stable EoS : N²LO, $\Lambda = 450$ MeV.

ϵ (MeV/fm ⁻³)	P (MeV/fm ⁻³)	ρ_c (fm ⁻³)
32.6865	0.09543	0.03458
48.5574	0.18318	0.05131
64.4625	0.29451	0.06803
80.4076	0.47175	0.08476
96.3959	0.72483	0.10148
112.437	1.07194	0.11820
128.543	1.53363	0.13493
144.709	2.10308	0.15165
160.960	2.83009	0.16837
177.287	3.70325	0.18510
193.707	4.76249	0.20182
210.238	6.03590	0.21854
226.853	7.44260	0.23527
243.607	9.08432	0.25199
260.484	11.0280	0.26871
277.462	13.3146	0.28544
294.600	15.9405	0.30216
313.052	19.0452	0.32000

Table B.2: β -stable EoS : N²LO, $\Lambda = 500$ MeV.

ϵ (MeV/fm ⁻³)	P (MeV/fm ⁻³)	ρ_c (fm ⁻³)
32.6848	0.09322	0.03458
48.5523	0.17388	0.05131
64.4514	0.27578	0.06803
80.3875	0.43954	0.08476
96.3641	0.67713	0.10148
112.391	1.01069	0.11820
128.482	1.46295	0.13493
144.632	2.02657	0.15165
160.866	2.75110	0.16837
177.177	3.62480	0.18510
193.581	4.68982	0.20182
210.097	5.97467	0.21854
226.697	7.39487	0.23527
243.440	9.05973	0.25199
260.307	11.0374	0.26871
277.277	13.3702	0.28544
294.412	16.0647	0.30216
312.865	19.2627	0.32000

Table B.3: β -stable EoS : N³LO, $\Lambda = 450$ MeV.

ϵ (MeV/fm ⁻³)	P (MeV/fm ⁻³)	ρ_c (fm ⁻³)
32.6840	0.09153	0.03458
48.5508	0.17378	0.05131
64.4497	0.27776	0.06803
80.3867	0.44584	0.08476
96.3655	0.69081	0.10148
112.397	1.03779	0.11820
128.495	1.51473	0.13493
144.657	2.11479	0.15165
160.909	2.89309	0.16837
177.243	3.83844	0.18510
193.678	4.99160	0.20182
210.233	6.38511	0.21854
226.881	7.93435	0.23527
243.681	9.73802	0.25199
260.615	11.8694	0.26871
277.661	14.3709	0.28544
294.880	17.2116	0.30216
313.431	20.5466	0.32000

Table B.4: β -stable EoS : N³LO, $\Lambda = 500$ MeV.

ϵ (MeV/fm ⁻³)	P (MeV/fm ⁻³)	ρ_c (fm ⁻³)
32.6831	0.09005	0.03458
48.5474	0.16641	0.05131
64.4418	0.26456	0.06803
80.3720	0.42187	0.08476
96.3407	0.64590	0.10148
112.357	0.95894	0.11820
128.436	1.39779	0.13493
144.573	1.95525	0.15165
160.796	2.69323	0.16837
177.098	3.59691	0.18510
193.498	4.71275	0.20182
210.017	6.08066	0.21854
226.625	7.60953	0.23527
243.389	9.41871	0.25199
260.288	11.5877	0.26871
277.299	14.1611	0.28544
294.492	17.1101	0.30216
313.022	20.5920	0.32000

Table B.5: β -stable EoS : N⁴LO, $\Lambda = 450$ MeV.

ϵ (MeV/fm ⁻³)	P (MeV/fm ⁻³)	ρ_c (fm ⁻³)
32.6830	0.09009	0.03458
48.5470	0.16535	0.05131
64.4402	0.25975	0.06803
80.3675	0.40920	0.08476
96.3316	0.62480	0.10148
112.342	0.92890	0.11820
128.411	1.34656	0.13493
144.535	1.87196	0.15165
160.738	2.55251	0.16837
177.014	3.37886	0.18510
193.376	4.38497	0.20182
209.844	5.59975	0.21854
226.393	6.95243	0.23527
243.073	8.52244	0.25199
259.870	10.3732	0.26871
276.764	12.5406	0.28544
293.807	14.9855	0.30216
312.144	17.8429	0.32000

Table B.6: β -stable EoS : N⁴LO, $\Lambda = 500$ MeV.

ϵ (MeV/fm ⁻³)	P (MeV/fm ⁻³)	ρ_c (fm ⁻³)
32.6826	0.08939	0.03458
48.5456	0.16263	0.05131
64.4372	0.25524	0.06803
80.3621	0.40217	0.08476
96.3231	0.61136	0.10148
112.328	0.90163	0.11820
128.390	1.30135	0.13493
144.505	1.80545	0.15165
160.697	2.46896	0.16837
176.960	3.27918	0.18510
193.309	4.27486	0.20182
209.765	5.48758	0.21854
226.300	6.83709	0.23527
242.971	8.42755	0.25199
259.762	10.3254	0.26871
276.650	12.5695	0.28544
293.696	15.1513	0.30216
312.048	18.2083	0.32000

Table B.7: $1.4 M_{\odot}$: N²LO, $\Lambda = 450$ MeV.

Γ_1	Γ_2	R (km)	ρ_c (fm ⁻³)	v_s (c)
1.5	3.5	10.9557	0.6850	0.7308
1.5	4.0	11.0733	0.6391	0.7802
1.5	4.5	11.1539	0.6088	0.8271
2.0	3.0	11.2274	0.6621	0.6554
2.0	3.5	11.3216	0.6148	0.7088
2.0	4.0	11.3904	0.5864	0.7584
2.0	4.5	11.4311	0.5669	0.8023
2.5	3.0	11.5978	0.5773	0.6339
2.5	3.5	11.6387	0.5543	0.6861
2.5	4.0	11.6626	0.5392	0.7361
2.5	4.5	11.6757	0.5291	0.7883
3.0	2.5	11.8644	0.5231	0.5649
3.0	3.0	11.8657	0.5117	0.6232
3.0	3.5	11.8748	0.5052	0.6809
3.0	4.0	11.8792	0.5007	0.7381
3.0	4.5	11.8737	0.4968	0.7923
3.5	2.5	12.0395	0.4652	0.5979
3.5	3.0	12.0325	0.4637	0.6456
3.5	3.5	12.0326	0.4632	0.6725
3.5	4.0	12.0322	0.4621	0.7043
3.5	4.5	12.0318	0.4611	0.7315
4.0	1.5	12.1346	0.4337	0.7625
4.0	2.0	12.1350	0.4338	0.7506
4.0	2.5	12.1342	0.4338	0.7414
4.0	3.0	12.1337	0.4335	0.7390
4.0	3.5	12.1343	0.4339	0.7318
4.0	4.0	12.1356	0.4343	0.7176
4.0	4.5	12.1356	0.4344	0.7132
4.5	1.5	12.2193	0.4143	0.8119
4.5	2.0	12.2192	0.4143	0.7977
4.5	2.5	12.2083	0.4143	0.7880
4.5	3.0	12.2079	0.4141	0.7835
4.5	3.5	12.2075	0.4139	0.7853
4.5	4.0	12.2092	0.4145	0.7752
4.5	4.5	12.2102	0.4148	0.7585

Table B.8: $1.4 M_{\odot}$: N²LO, $\Lambda = 500$ MeV.

Γ_1	Γ_2	R (km)	ρ_c (fm ⁻³)	v_s (c)
1.5	3.5	10.9714	0.6798	0.7288
1.5	4.0	11.0807	0.6353	0.7785
1.5	4.5	11.1521	0.6058	0.8253
2.0	3.5	11.3348	0.6102	0.7070
2.0	4.0	11.3868	0.5829	0.7561
2.0	4.5	11.4334	0.5641	0.8000
2.5	3.0	11.6051	0.5718	0.6319
2.5	3.5	11.6397	0.5503	0.6841
2.5	4.0	11.6592	0.5363	0.7354
2.5	4.5	11.6769	0.5268	0.7885
3.0	3.0	11.8683	0.5075	0.6221
3.0	3.5	11.8701	0.5017	0.6801
3.0	4.0	11.8771	0.4977	0.7373
3.0	4.5	11.8694	0.4942	0.7912
3.5	2.5	12.0310	0.4619	0.6074
3.5	3.0	12.0237	0.4607	0.6496
3.5	3.5	12.0237	0.4603	0.6717
3.5	4.0	12.0228	0.4595	0.6994
3.5	4.5	12.0301	0.4586	0.7231
4.0	2.0	12.1226	0.4316	0.7535
4.0	2.5	12.1227	0.4316	0.7436
4.0	3.0	12.1222	0.4313	0.7401
4.0	3.5	12.1229	0.4318	0.7324
4.0	4.0	12.1234	0.4321	0.7167
4.0	4.5	12.1243	0.4323	0.7105
4.5	1.5	12.1985	0.4127	0.8102
4.5	2.0	12.1985	0.4127	0.7963
4.5	2.5	12.1984	0.4127	0.7854
4.5	3.0	12.1980	0.4125	0.7813
4.5	3.5	12.1974	0.4123	0.7828
4.5	4.0	12.1994	0.4128	0.7738
4.5	4.5	12.2005	0.4131	0.7576

Table B.9: $1.4 M_{\odot}$: N³LO, $\Lambda = 450$ MeV.

Γ_1	Γ_2	R (km)	ρ_c (fm ⁻³)	v_s (c)
1.5	3.5	11.1945	0.6525	0.7179
1.5	4.0	11.2849	0.6145	0.7673
1.5	4.5	11.3428	0.5891	0.8127
2.0	3.0	11.4904	0.6200	0.6415
2.0	3.5	11.5575	0.5854	0.6945
2.0	4.0	11.6001	0.5635	0.7412
2.0	4.5	11.6229	0.5483	0.7857
2.5	3.0	11.8309	0.5430	0.6210
2.5	3.5	11.8436	0.5291	0.6770
2.5	4.0	11.8521	0.5208	0.7343
2.5	4.5	11.8647	0.5139	0.7891
3.0	2.5	12.0536	0.4877	0.5551
3.0	3.0	12.0573	0.4846	0.6154
3.0	3.5	12.0603	0.4819	0.6711
3.0	4.0	12.0541	0.4794	0.7209
3.0	4.5	12.0560	0.4776	0.7662
3.5	2.5	12.1836	0.4443	0.6596
3.5	3.0	12.1838	0.4440	0.6727
3.5	3.5	12.1840	0.4444	0.6647
3.5	4.0	12.1844	0.4443	0.6709
3.5	4.5	12.1840	0.4440	0.6764
4.0	1.5	12.2719	0.4195	0.7590
4.0	2.0	12.2719	0.4196	0.7441
4.0	2.5	12.2726	0.4196	0.7341
4.0	3.0	12.2721	0.4193	0.7308
4.0	3.5	12.2729	0.4197	0.7264
4.0	4.0	12.2737	0.4201	0.7101
4.0	4.5	12.2739	0.4203	0.6985
4.5	1.5	12.3235	0.4035	0.7922
4.5	2.0	12.3234	0.4035	0.7808
4.5	2.5	12.3239	0.4034	0.7746
4.5	3.0	12.3234	0.4033	0.7717
4.5	3.5	12.3225	0.4031	0.7724
4.5	4.0	12.3239	0.4034	0.7661
4.5	4.5	12.3236	0.4036	0.7504

Table B.10: $1.4 M_{\odot}$: N³LO, $\Lambda = 500$ MeV.

Γ_1	Γ_2	R (km)	ρ_c (fm ⁻³)	v_s (c)
1.5	3.5	11.1565	0.6516	0.7179
1.5	4.0	11.2457	0.6138	0.7674
1.5	4.5	11.3074	0.5887	0.8128
2.0	3.0	11.4438	0.6191	0.6416
2.0	3.5	11.5122	0.5847	0.6947
2.0	4.0	11.5488	0.5630	0.7414
2.0	4.5	11.5691	0.5479	0.7860
2.5	3.0	11.7759	0.5425	0.6214
2.5	3.5	11.7930	0.5287	0.6776
2.5	4.0	11.8015	0.5206	0.7352
2.5	4.5	11.8104	0.5138	0.7900
3.0	2.5	12.0059	0.4874	0.5557
3.0	3.0	11.9974	0.4842	0.6160
3.0	3.5	12.0005	0.4817	0.6716
3.0	4.0	12.0037	0.4791	0.7211
3.0	4.5	12.0049	0.4773	0.7660
3.5	2.5	12.1299	0.4441	0.6591
3.5	3.0	12.1298	0.4438	0.6719
3.5	3.5	12.1302	0.4441	0.6656
3.5	4.0	12.1298	0.4441	0.6703
3.5	4.5	12.1294	0.4438	0.6755
4.0	1.5	12.2150	0.4194	0.7609
4.0	2.0	12.2150	0.4195	0.7462
4.0	2.5	12.2160	0.4195	0.7345
4.0	3.0	12.2152	0.4192	0.7301
4.0	3.5	12.2037	0.4196	0.7260
4.0	4.0	12.2045	0.4200	0.7108
4.0	4.5	12.2051	0.4202	0.6996
4.5	1.5	12.2676	0.4035	0.7943
4.5	2.0	12.2687	0.4035	0.7831
4.5	2.5	12.2683	0.4034	0.7733
4.5	3.0	12.2673	0.4032	0.7705
4.5	3.5	12.2666	0.4030	0.7710
4.5	4.0	12.2597	0.4034	0.7658
4.5	4.5	12.2595	0.4036	0.7514

Table B.11: $1.4 M_{\odot}$: N⁴LO, $\Lambda = 450$ MeV.

Γ_1	Γ_2	R (km)	ρ_c (fm ⁻³)	v_s (c)
1.5	3.5	10.7114	0.7129	0.7417
1.5	4.0	10.8511	0.6590	0.7893
1.5	4.5	10.9395	0.6251	0.8367
2.0	3.5	11.0825	0.6399	0.7191
2.0	4.0	11.1566	0.6052	0.7695
2.0	4.5	11.2082	0.5821	0.8151
2.5	3.0	11.3453	0.6075	0.6449
2.5	3.5	11.3997	0.5767	0.6982
2.5	4.0	11.4296	0.5568	0.7462
2.5	4.5	11.4514	0.5428	0.7923
3.0	3.0	11.6442	0.5361	0.6303
3.0	3.5	11.6504	0.5239	0.6857
3.0	4.0	11.6550	0.5159	0.7414
3.0	4.5	11.6623	0.5100	0.7960
3.5	2.5	11.8395	0.4844	0.5597
3.5	3.0	11.8382	0.4811	0.6270
3.5	3.5	11.8370	0.4791	0.6783
3.5	4.0	11.8358	0.4771	0.7280
3.5	4.5	11.8340	0.4754	0.7726
4.0	2.0	11.9534	0.4473	0.6976
4.0	2.5	11.9519	0.4470	0.7050
4.0	3.0	11.9502	0.4463	0.7187
4.0	3.5	11.9501	0.4465	0.7237
4.0	4.0	11.9493	0.4466	0.7240
4.0	4.5	11.9480	0.4462	0.7334
4.5	1.5	12.0343	0.4238	0.8262
4.5	2.0	12.0347	0.4239	0.8116
4.5	2.5	12.0349	0.4240	0.8003
4.5	3.0	12.0345	0.4238	0.7938
4.5	3.5	12.0340	0.4236	0.7973
4.5	4.0	12.0359	0.4243	0.7809
4.5	4.5	12.0372	0.4246	0.7653

Table B.12: $1.4 M_{\odot}$: N⁴LO, $\Lambda = 500$ MeV.

Γ_1	Γ_2	R (km)	ρ_c (fm ⁻³)	v_s (c)
1.5	3.5	10.7458	0.7040	0.7385
1.5	4.0	10.8795	0.6527	0.7868
1.5	4.5	10.9644	0.6200	0.8340
2.0	3.5	11.1163	0.6319	0.7162
2.0	4.0	11.1846	0.5993	0.7668
2.0	4.5	11.2317	0.5774	0.8116
2.5	3.0	11.3801	0.5981	0.6422
2.5	3.5	11.4238	0.5697	0.6948
2.5	4.0	11.4573	0.5513	0.7429
2.5	4.5	11.4766	0.5384	0.7907
3.0	3.0	11.6605	0.5285	0.6286
3.0	3.5	11.6724	0.5182	0.6848
3.0	4.0	11.6745	0.5114	0.7413
3.0	4.5	11.6833	0.5062	0.7961
3.5	2.5	11.8443	0.4784	0.5667
3.5	3.0	11.8428	0.4758	0.6310
3.5	3.5	11.8415	0.4743	0.6771
3.5	4.0	11.8392	0.4726	0.7221
3.5	4.5	11.8380	0.4710	0.7619
4.0	2.0	11.9594	0.4431	0.7184
4.0	2.5	11.9593	0.4429	0.7209
4.0	3.0	11.9577	0.4423	0.7297
4.0	3.5	11.9573	0.4427	0.7293
4.0	4.0	11.9575	0.4428	0.7227
4.0	4.5	11.9565	0.4426	0.7269
4.5	1.5	12.0322	0.4209	0.8238
4.5	2.0	12.0333	0.4210	0.8091
4.5	2.5	12.0336	0.4210	0.7964
4.5	3.0	12.0331	0.4208	0.7904
4.5	3.5	12.0318	0.4206	0.7930
4.5	4.0	12.0344	0.4213	0.7795
4.5	4.5	12.0359	0.4216	0.7639